



INSA

N°d'ordre NNT : 2018LYSEI043

THESE de DOCTORAT DE L'UNIVERSITE DE LYON
opérée au sein de
I'Institut National des Sciences Appliquées de Lyon

Ecole Doctorale N°ED162
MECANIQUE, ENERGETIQUE, GENIE CIVIL, ACOUSTIQUE

Spécialité de doctorat :
Discipline : Mécanique – Génie Mécanique – Génie Civil

Soutenue publiquement le 16/05/2018, par :
Wenqi ZHU

Effective elastic properties of foams: morphological study and micromechanical modeling

Devant le jury composé de :

			Président
MONERIE Yann	Professeur des Universités	Univ Montpellier	Rapporteur
DUMONTET Héléne	Professeur des Universités	UPMC	Rapporteuse
BARANGER Thouraya	Professeur des Universités	Univ-lyon1	Examinatrice
MACHADO Guilherme	Maître de Conférences	AMU	Examineur
BAILLIS Dominique	Professeur des Universités	INSA Lyon	Directrice de thèse
BLAL Nawfal	Maître de Conférences	INSA Lyon	Co-directeur

Département FEDORA – INSA Lyon - Ecoles Doctorales – Quinquennal 2016-2020

SIGLE	ECOLE DOCTORALE	NOM ET COORDONNEES DU RESPONSABLE
CHIMIE	CHIMIE DE LYON http://www.edchimie-lyon.fr Sec. : Renée EL MELHEM Bât. Blaise PASCAL, 3e étage secretariat@edchimie-lyon.fr INSA : R. GOURDON	M. Stéphane DANIELE Institut de recherches sur la catalyse et l'environnement de Lyon IRCELYON-UMR 5256 Équipe CDFA 2 Avenue Albert EINSTEIN 69 626 Villeurbanne CEDEX directeur@edchimie-lyon.fr
E.E.A.	ÉLECTRONIQUE, ÉLECTROTECHNIQUE, AUTOMATIQUE http://edeea.ec-lyon.fr Sec. : M.C. HAVGOUDOUKIAN ecole-doctorale.eea@ec-lyon.fr	M. Gérard SCORLETTI École Centrale de Lyon 36 Avenue Guy DE COLLONGUE 69 134 Écully Tél : 04.72.18.60.97 Fax 04.78.43.37.17 gerard.scorletti@ec-lyon.fr
E2M2	ÉVOLUTION, ÉCOSYSTÈME, MICROBIOLOGIE, MODÉLISATION http://e2m2.universite-lyon.fr Sec. : Sylvie ROBERJOT Bât. Atrium, UCB Lyon 1 Tél : 04.72.44.83.62 INSA : H. CHARLES secretariat.e2m2@univ-lyon1.fr	M. Philippe NORMAND UMR 5557 Lab. d'Ecologie Microbienne Université Claude Bernard Lyon 1 Bâtiment Mendel 43, boulevard du 11 Novembre 1918 69 622 Villeurbanne CEDEX philippe.normand@univ-lyon1.fr
EDISS	INTERDISCIPLINAIRE SCIENCES-SANTÉ http://www.ediss-lyon.fr Sec. : Sylvie ROBERJOT Bât. Atrium, UCB Lyon 1 Tél : 04.72.44.83.62 INSA : M. LAGARDE secretariat.ediss@univ-lyon1.fr	Mme Emmanuelle CANET-SOULAS INSERM U1060, CarMeN lab, Univ. Lyon 1 Bâtiment IMBL 11 Avenue Jean CAPELLE INSA de Lyon 69 621 Villeurbanne Tél : 04.72.68.49.09 Fax : 04.72.68.49.16 emmanuelle.canet@univ-lyon1.fr
INFOMATHS	INFORMATIQUE ET MATHÉMATIQUES http://edinfomaths.universite-lyon.fr Sec. : Renée EL MELHEM Bât. Blaise PASCAL, 3e étage Tél : 04.72.43.80.46 Fax : 04.72.43.16.87 infomaths@univ-lyon1.fr	M. Luca ZAMBONI Bât. Braconnier 43 Boulevard du 11 novembre 1918 69 622 Villeurbanne CEDEX Tél : 04.26.23.45.52 zamboni@maths.univ-lyon1.fr
Matériaux	MATÉRIAUX DE LYON http://ed34.universite-lyon.fr Sec. : Marion COMBE Tél : 04.72.43.71.70 Fax : 04.72.43.87.12 Bât. Direction ed.materiaux@insa-lyon.fr	M. Jean-Yves BUFFIÈRE INSA de Lyon MATEIS - Bât. Saint-Exupéry 7 Avenue Jean CAPELLE 69 621 Villeurbanne CEDEX Tél : 04.72.43.71.70 Fax : 04.72.43.85.28 jean-yves.buffiere@insa-lyon.fr
MEGA	MÉCANIQUE, ÉNERGÉTIQUE, GÉNIE CIVIL, ACOUSTIQUE http://edmega.universite-lyon.fr Sec. : Marion COMBE Tél : 04.72.43.71.70 Fax : 04.72.43.87.12 Bât. Direction mega@insa-lyon.fr	M. Jocelyn BONJOUR INSA de Lyon Laboratoire CETHIL Bâtiment Sadi-Carnot 9, rue de la Physique 69 621 Villeurbanne CEDEX jocelyn.bonjour@insa-lyon.fr
ScSo	ScSo* http://ed483.univ-lyon2.fr Sec. : Viviane POLSINELLI Brigitte DUBOIS INSA : J.Y. TOUSSAINT Tél : 04.78.69.72.76 viviane.polsinelli@univ-lyon2.fr	M. Christian MONTES Université Lyon 2 86 Rue Pasteur 69 365 Lyon CEDEX 07 christian.montes@univ-lyon2.fr

ScSo : Histoire, Géographie, Aménagement, Urbanisme, Archéologie, Science politique, Sociologie,

Cette thèse est accessible à l'adresse : <http://theses.insa-lyon.fr/publication/2018LYSEI043/these.pdf>

© [W. Zhu], [2018], INSA Lyon, tous droits réservés

Remerciements

This thesis is financed by China Scholarship Council (CSC).

I remember clearly when I first set foot on this land, my heart was filled with excitement and longing. And through the miracle of time, I will soon complete my doctoral studies. Looking back on these three and a half years, there are so many people I need to thank.

First of all, I would like to express my sincere gratitude to my two supervisors, Prof. Dominique BAILLIS and Associate Professor Nawfal BLAL. It is not only their academic guidance but also their support and encouragement that runs throughout my doctoral career. Without their guidance, this work could not have been completed. They have also set a good example for me of their meticulous attitude towards academic work. It is really a privilege to have them as my supervisors.

I truly appreciate the members of the jury, Prof. Yann MONERIE and Prof. H el ene DUMONTET as the reviewers, and Prof. Thouraya BARANGER and Associate Professor Guilherme MACHADO as the examiners. Thank them for their presence in the jury and reviewing my work.

In these three and a half years, especially in the first year, Paul-Marie MICHAUD shares his precious experience in modeling and mechanical properties of foam materials with me, which makes me benefit a lot. I really appreciate it.

Meanwhile, I would also like to thank my colleagues in LaMCoS for the good time : K. AMUZUGA, F. FEKAK, A. GLACET, T. HIRSCHLER, N.LION, Y. LU, T.MAQUART, P. PANICO, S. CHEN, M. WANG, G. COUDOUEL, D. LIU, W. GAO, T. JAILIN, A. SONDE, C. ZHANG, M. DIA, I. COMBY, H. LUO, Z. LOW. I am particularly grateful to S. CUNSOLO for his help in modeling and the collaboration in simulating, and L. ZHAO and W. YE for their useful discussions and suggestions when I encountered problems.

Last but not least, I would like to thank the closest people who love me and support me along the way.

Abstract

Thanks to the excellent combination of physical, mechanical and thermal properties, foam materials bring new possibilities to extend the range of the properties for engineering, which is limited by fully dense solids. In this study, a micromechanical modeling based on Hill's lemma (Hill's lemma periodic computational homogenization approach) is proposed for predicting the effective elastic properties of foam materials. An approach based on Voronoi diagram is used to generate realistic periodic foam structures, including regular and irregular open-cell structures, and irregular closed-cell structures.

First, the influences of morphological parameters of open-cell foams on the effective elastic properties are studied. The generated structures allow representing the details of the microstructure and cover a large range of foam materials for engineering purposes. With the assessments, new generic analytical laws are proposed for Kelvin open-cell foams by considering their morphological parameters. Second, the tomography images are analysed to obtain the morphological description of the real irregular open-cell structure. With these morphological parameters, numerous numerical realistic structures are generated. Specific statistic methods are proposed to determine the Representative Volume Element (RVE) for foam models. Third, the anisotropic irregular closed-cell foam is studied. The numerical structures are generated with the morphological description of the reconstructed tomography structure and the effective elastic properties of the closed-cell foam models are estimated. The numerical results show the satisfying agreement with the experimental results.

KEY WORDS: Foam, Morphology, Tomography, Periodic computational homogenization, Effective elastic properties, Representative volume element

Résumé

Les matériaux cellulaires poreux de type mousse présentent un grand intérêt pour de nombreuses applications. Leurs propriétés thermiques, mécaniques, acoustiques dépendent fortement de leur microstructure complexe. Afin de mieux comprendre la relation microstructure/propriétés mécaniques de ces matériaux, une modélisation micromécanique basée sur une méthode d'homogénéisation périodique et le lemme de Hill est proposée pour prédire les propriétés élastiques effectives de ces matériaux. Une approche basée sur le diagramme de Voronoï est utilisée pour générer des structures de mousse périodiques réalistes plus ou moins irrégulières, couvrant une large gamme de matériaux. Différents types de mousses à forte porosité sont générés, non seulement des matériaux cellulaires à pores ouverts mais aussi des matériaux cellulaires à pores fermés. Des comparaisons avec des résultats issus de tomographie X d'architectures réelles 3D de mousses valident ces approches de Voronoï.

Les simulations numériques permettent d'étudier l'influence des paramètres morphologiques des mousses sur les propriétés élastiques effectives. De nouvelles lois analytiques génériques de propriétés effectives sont déduites pour des mousses à cellules ouvertes de type Kelvin. Une attention particulière est portée sur la détermination de l'élément de volume représentatif (VER). Des méthodes statistiques spécifiques sont proposées pour déterminer le VER approprié aux modèles de mousse. Dans le cas des mousses polymères isolantes à cellules fermées irrégulières anisotropes, la confrontation avec des résultats d'essais mécaniques confirme la validité des modèles développés.

MOTS CLÉS: Mousse, Morphologie, Tomographie, Homogénéisation périodique, Propriétés élastiques effectives, Élément de volume représentatif.

Contents

Contents	i
List of Figures	v
List of Tables	ix
Notations	xi
Introduction	1
1 Introduction to foams	2
1.1 Productions of foams	2
1.2 Structures of foams	3
1.3 Properties and applications of foams	4
2 Review of previous work to foams	5
2.1 Experimental studies	6
2.2 Modeling studies	9
3 Scope of the thesis	11
1 Homogenization for linear elasticity	13
1 Basic concepts	15
1.1 Constitutive equations	15
1.2 Material symmetries and anisotropy	16
2 Homogenization	19
2.1 The concept of Homogenization	19
2.2 Representative volume element	20
2.3 Boundary conditions	21
3 Analytical techniques for elastic properties	22
3.1 Bounding methods	23
3.2 Analytical models	25
4 Usual computational homogenization approach based on the finite element method	27

2	Effective elastic properties of regular Kelvin open-cell foams	29
1	Introduction	31
2	Modeling of open-cell structure	32
3	Computational periodic homogenization	35
	3.1 Hill's lemma for periodic media [SUQ 87]	35
	3.2 Finite element implementation of Hill's lemma approach (HL-FEM)	36
4	Numerical study	39
	4.1 Mesh sensitivity	39
	4.2 Validation by usual FEM	40
	4.3 RVE sensitivity	42
5	Parametric study	43
	5.1 Effect of Young's modulus of bulk	43
	5.2 Effect of relative density	43
	5.3 Effect of normalized curvature	44
	5.4 Effect of diameter ratio	46
	5.5 Effect of irregularity and dispersion of cell size distribution	49
6	Conclusion	53
3	Effective elastic properties of periodic irregular open-cell foams	55
1	Introduction	57
2	Modeling of irregular open-cell structure from tomography slices	57
	2.1 Morphological analysis of open-cell foam	57
	2.2 Generations of numerical structures	61
3	RVE determination approach	62
	3.1 Kanit's relation for linear properties [KAN 03]	62
	3.2 Moussaddy's algorithm [MOU 13]	64
4	Numerical simulation	66
5	Results and discussion	67
	5.1 Influence of RVE parameters	67
	5.2 Results of Kanit's method	67
	5.3 Results of Moussaddy's algorithm	72
	5.4 New suggestions of the determination of the RVE	76
6	Conclusion	78
4	Effective elastic properties of periodic irregular closed-cell foams	81
1	Introduction	83
2	Modeling of irregular closed-cell structure	83
	2.1 Material and its properties	83
	2.2 Morphological description	85
	2.3 Generations of numerical models	86
3	Results and discussion	90
	3.1 Influence of kinematic modeling	90
	3.2 Influence of RVE parameters	91

3.3	Influence of relative density	92
3.4	Comparison with tomography model	94
3.5	Comparison with experimental results	100
4	Conclusion	102
General conclusions and prospects		103
A The variational asymptotic method for unit cell homogenization (VAMUCH)		107
B Enforced periodic boundary condition		109
1	Polynomial interpolation	109
2	Fixed point method	111
2.1	Influence of relative density	112
2.2	Influence of layer thickness	113
2.3	Influence of number of elements	113
3	Conclusion	115
Bibliography		117

List of Figures

1	Natural cellular materials : (a) cork ; (b) balsa ; (c) sponge ; (d) cancellous bone ; (e) coral ; (f) cuttlefish bone ; (g) iris leaf ; (h) stalk of a plant [GIB 97].	1
2	Examples of different structures of solid foams : (a) closed-cell carbon foam [RUI 15] ; (b) open-cell nickel foam [FAN 17] ; (c) polyether foam with both open and closed cells [GIB 97].	3
3	Ashby's material map for the modulus-density space [ASH 13].	5
4	Stress-strain curves with different densities and orientations for Al foam in compression [NIE 00].	6
5	Typical compressive response of an aluminum open-cell foam [JAN 09].	7
6	Sequence of full cross-section deformed configurations corresponding to each stage in FIG. 5 [JAN 09].	7
7	Sequence of deformed configurations of site A corresponding to each stage in FIG. 5 [JAN 09].	8
8	Sequence of deformed configurations of site B corresponding to each stage in FIG. 5 [JAN 09].	8
9	Stress-strain curves of aluminum foams at different strain rates [WAN 06].	9
1.1	Illustration : A macro composite, a heterogeneous medium from the composite and the corresponding homogeneous medium.	20
1.2	Illustration of the convergence property with the RVE size shown in [NGU 12] : (a) RVE with different sizes ; (b) The convergence of average properties with the increase of RVE size under different boundary condition types.	22
2.1	(a) Unwrapped periodic structure ; (b) Structure with the duplicated parts on the sides ; (c) Domain cut to periodic bounding box.	33
2.2	The dispersions of cell size distributions with different C_V s.	33
2.3	The variation of cross section of strut.	34
2.4	The variation of longitudinal profile of strut.	35
2.5	Illustration of the corresponding nodes on the boundary surfaces.	38
2.6	The reference model ($\rho^{\text{hom}}/\rho^{\text{b}} = 6\%, q = 1, t = 1, \text{Kelvin}$).	40
2.7	The relation between C_{ij}^{hom} and the number of elements for the reference model ($\rho^{\text{hom}}/\rho^{\text{b}} = 6\%, q = 1, t = 1, \text{Kelvin}$).	41
2.8	Illustration of Model 1 [#] and Model 2 [#] .	42

2.9	Evolution of (a) effective Young's modulus, (b) effective shear modulus and (c) effective Poisson's ratio with respect to the relative density.	45
2.10	Effect of the relative density for the models ($q = 1, t = 1, Kelvin$) on the normalized properties.	46
2.11	Effect of the normalized curvature for the models ($\rho^{hom}/\rho^b = 6\%, t = 1, Kelvin$) on the deviation indicators.	47
2.12	Evolutions of (a) C_{11}^{hom}/C_{11}^b , (b) C_{12}^{hom}/C_{12}^b and (c) C_{44}^{hom}/C_{44}^b with respect to the relative density by the analytical laws (al) and the computational results (cr) with ($q = \{-0.3; 0.5; 1\}$).	48
2.13	Effect of the diameter ratio for the models ($\rho^{hom}/\rho^b = 6\%, q = 1, Kelvin$) on the deviation indicators.	49
2.14	Evolutions of (a) C_{11}^{hom}/C_{11}^b , (b) C_{12}^{hom}/C_{12}^b and (c) C_{44}^{hom}/C_{44}^b with respect to the relative density by the analytical laws (al) and the computational results (cr) with ($t = \{0.33; 0.38; 0.43; 1\}$).	50
3.1	Tomographic data of the irregular open-cell structure : (a) slice of the sample ($571 \times 571 \text{ px}^2$); (b) 3D rendering after reconstruction ($571 \times 571 \times 484 \text{ px}^3$).	58
3.2	Covariance functions in three directions of solid phase of open-cell sample microstructure.	59
3.3	(a) Illustration of S_{sur} , d_o and d_i in the case $q = 0$ (flat triangle cross section); (b) Illustration of $d_{j,max}$	60
3.4	Illustration of numerical irregular open-cell structure ($\rho^{hom}/\rho^b = 6.4\%$) for (a) Set A*; (b) Set B*; (c) Set C*; (d) Set D* and (e) Set E*.	61
3.5	Evolution of the mean elastic property as a function of the number of realizations : (a) k^{hom} and μ^{hom} for Set D*; (b) k^{hom} for each set.	68
3.6	Evolution of the normalized mean property as a function of the RVE volume.	69
3.7	Evolution of the variance ratio $D_z^2(V)/D_z^2$ as a function of the RVE volume.	70
3.8	Evolution of ζ_{iso} as a function of the number of realizations for five sets.	73
3.9	Evolution of ζ_{con} as a function of the number of realizations for (a) Set A*; (b) Set B*; (c) Set C*; (d) Set D* and (e) Set E*.	74
3.10	Evolution of (a) δ_{dev} , (b) δ_{ave} and (c) δ_{err} as a function of the RVE volume.	75
4.1	Tomographic data of the irregular closed-cell structure : (a) a tomography slice ($400 \times 400 \text{ px}^2$); (b) 3D rendering after reconstruction.	84
4.2	Covariance functions in three directions of solid phase of closed-cell sample microstructure.	86
4.3	Illustration of the blurs in the tomography slice which leads to the error.	86
4.4	Original (a) and exploded (b) cell structure. Colors identify cells. Walls are pattern filled.	87
4.5	Full cell structure showing the space between cells (wall thickness) in 3D.	88
4.6	Normalized cell diameter distributions of the tomography structure and the numerical structure, as calculated by iMorph.	88

4.7	Illustration of numerical irregular closed-cell model for (a) Set A; (b) Set B; (c) Set C; (d) Set D and (e) Set E.	89
4.8	An original overall isotropic model is mesh with (a) 304,341 shell elements and (b) 891,823 solid elements, respectively.	91
4.9	Illustration of (a) tensile simulation and (b) shear simulation in a 2D perspective.	92
4.10	Deformations of (a) shell model and (b) solid model for the tensile test along direction 11 with <i>von Mises</i> equivalent stress map.	93
4.11	Deformations of (a) shell model and (b) solid model for the shear test along direction 12 with <i>von Mises</i> equivalent stress map.	94
4.12	Comparison of the tensile response and the shear response between shell model and solid model.	95
4.13	Evolutions of \bar{k}^{hom} and $\bar{\mu}^{\text{hom}}$ as a function of the number of realizations for Set A.	95
4.14	Evolution of \bar{k}^{hom} and $\bar{\mu}^{\text{hom}}$ as a function of the RVE volume.	96
4.15	Effect of the relative density on the effective elastic moduli.	96
4.16	Deformations of the tomography model for (a) the tensile test and (a) the shear test with <i>von Mises</i> equivalent stress map.	97
4.17	The evolution of the energy density as a function of (a) $\bar{\sigma}_{11}$ and (b) $\bar{\sigma}_{12}$ for each model.	99
4.18	Illustration of (a) the cubic specimen for compression test and (b) the “Batman”-shaped specimen for shear test.	100
4.19	Illustration of the shear deformation of the “Batman”-shaped specimen.	101
4.20	Stress-strain curves of the macroscopic compression and shear tests (the effective elastic moduli obtained by numerical simulations are drawn with the black lines).	101
B.1	Illustration of the positions and the relations of four nodes.	110
B.2	The elements on two opposite surfaces.	111
B.3	Illustration of the fixed point method.	112
B.4	Illustration of the Kelvin open-cell structure surrounded by a layer.	112
B.5	Effect of the relative density on δ	114
B.6	Effect of the normalized layer thickness on δ	114
B.7	Effect of the number of elements of foam model on δ	115

List of Tables

1.1	The calculation procedures for the usual computational homogenization approach based on the FEM to obtain $[\mathbb{C}^{\text{hom}}]$	28
2.1	The comparison of the effective properties obtained by HL-FEM and Abaqus.	42
2.2	The comparison of the effective properties between Model 1 [#] and Model 2 [#]	43
2.3	Illustration of Kelvin structure and irregular structures with different C_V s.	51
2.4	The comparison of mean effective properties among Kelvin model and irregular models ($C_V = \{0; 0.05; 0.1\}$).	53
3.1	Characterizations of each set of open-cell structures ($\rho^{\text{hom}}/\rho^{\text{b}} = 6.4\%$).	62
3.2	The integral range \mathcal{A}^3 and the coefficient α for the effective elastic moduli k^{hom} and μ^{hom} , which are estimated by fitting with EQ. 3.9 ($\rho^{\text{hom}}/\rho^{\text{b}} = 6.4\%$).	69
3.3	Minimal number of realizations estimated to obtain the effective elastic modulus for each set ($\rho^{\text{hom}}/\rho^{\text{b}} = 6.4\%$).	71
3.4	The integral range \mathcal{A}^3 and the coefficient α for the contrastive models ($\rho^{\text{hom}}/\rho^{\text{b}} = 4\%$).	71
3.5	Minimal number of realizations for the contrastive models ($\rho^{\text{hom}}/\rho^{\text{b}} = 4\%$).	72
3.6	Number of realization n_r and RVE set determined by each method (M) with $tol = 5\%$ for all criteria except $\zeta_{iso} \leq 1\%$	76
3.7	The comparison of the required numbers of realizations and the obtained properties for Set B*.	77
3.8	The comparison of the errors for k^{hom} combined with the set (volume) and the number of realizations determined by ζ_{con} (23, 16, 10, 11 and 10 for each set, respectively).	78
3.9	The RVE parameters determined by the proposed methods for the foam models.	78
4.1	Characterizations of each set of closed-cell structures.	89

Notations

In this manuscript, the scalars are denoted by italic Roman letters, e.g. a , or italic Greek letters, e.g. α . The vectors are denoted by bold italic Roman letters, e.g. \mathbf{u} (u_i in index notation). The second-order tensors are denoted by bold italic Roman letters, e.g. \mathbf{M} (M_{ij} in index notation), or bold italic Greek letters, e.g. ϵ (ϵ_{ij} in index notation). The fourth-order tensors are denoted by double-barred Roman letters, e.g. \mathbb{P} (P_{ijkl} in index notation).

The dot product is denoted by a single point, e.g. $\mathbf{u} \cdot \mathbf{v}$. According to Einstein summation convention, one has $\mathbf{u} \cdot \mathbf{v} = u_i v_i$. The dyadic product is denoted by \otimes , e.g. $\mathbf{u} \otimes \mathbf{v} = u_i v_j$ and $\epsilon \otimes \epsilon = \epsilon_{ij} \epsilon_{kl}$. The other tensor products are denoted with the points and the number of points indicates the number of order of the contract product, e.g. $\mathbf{A} \cdot \mathbf{u} = A_{ij} u_j$, $\epsilon : \sigma = \epsilon_{ij} \sigma_{ij}$, $\mathbb{P} : \mathbf{A} = P_{ijkl} A_{kl}$.

The matrix representation of the components of a given tensor \mathbb{T} in a chosen orthonormal basis are denoted with brackets $[\mathbb{T}]$. All the matrices and vectors used for the finite element computation are also written with brackets.

Introduction

Solid cellular-structured materials exist universally in nature, such as wood, cancellous bone, coral, honeycomb, cork, etc. FIG. 1 shows various natural cellular materials. With the study of such materials, people are becoming more and more interested in the cellular structure due to its excellent properties. Over the years, numerous kinds of man-made foam materials have been produced and used in various fields. Solid foams are a medium composed of the two phases : solid and gas. Large amounts of solid materials can be foamed : metals, plastics, ceramics, glasses and even composites.

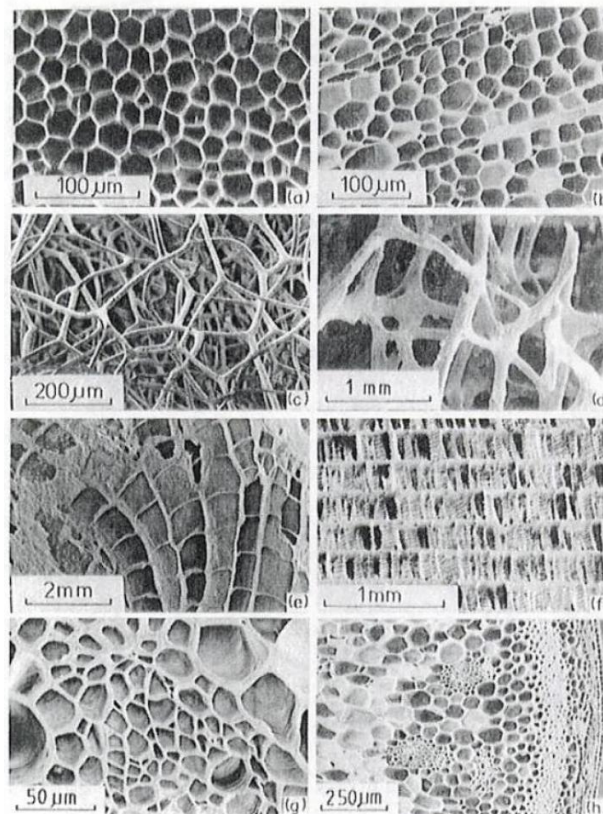


FIGURE 1: Natural cellular materials : (a) cork; (b) balsa; (c) sponge; (d) cancellous bone; (e) coral; (f) cuttlefish bone; (g) iris leaf; (h) stalk of a plant [GIB 97].

The general introduction to foam materials are presented from different aspects in

Section 1. In section 2, a review of the previous work in experimental and modeling studies of mechanical properties of foam materials is introduced. The scope of the thesis is reported in Section 3.

1 Introduction to foams

1.1 Productions of foams

The basic way to produce man-made solid foams is to generate air voids in a melt and solidify at a specific rate to satisfy the structure and the properties. There are a variety of processing routes to prepare foams, such as pouring the melt into a removable mould, gas injection into a melt, and immersion of gas releasing blowing agents into a melt [BAN 03, ASH 00, GIB 00].

In general, polymers are foamed by injecting gas bubbles into the liquid monomer or hot polymer, which allows the bubbles to grow and stabilize, and then solidifying the whole materials using cross-linking or cooling [GIB 97]. Either by mixing a blowing agent or by mechanical stirring, the gas is injected into the polymer. In order to form vapour bubbles, physical blowing agents work via adding inert gases such as carbon dioxide or nitrogen in the hot polymer at high pressure or by adding low melting point liquids such as chlorofluorocarbon or methylene chloride into the polymer and volatilize on heating. While for chemical blowing agents, additives are added either to decompose on heating or to combine together when mixed to release gas [GIB 97].

Metallic foams are made using liquid or solid state processing [SHA 94, DAV 83]. Aluminium foams are produced using mechanical agitation of a mixture of liquid aluminium and silicon carbide particles. Liquid metals can be permeated around granules which are removed after. Metals can be coated onto open-cell polymer foams using the techniques, such as electroless deposition, electrochemical deposition and chemical vapor deposition. Metal foams can also be manufactured by eutectic transformation. The powder metal is mixed with a spacing agent which decomposes or evaporates in the powder sintering method. For example, powdered metal can be mixed with powdered hydride, and then evolve hydrogen as a gas and form the foam by compacting and heating to the melting point of the metal. It is an important way to produce the single crystal silicon foam material with the anodizing process [GIB 97].

The preparations of glass foams and polymer foams are parallel. Ceramic foams can be made by infiltrating polymer foams with a slip while Carbon foams are made by graphitizing polymer foams. Ceramic foams can also be made using chemical vapour deposition onto a matrix of reticulated carbon foam. Cement foams are manufactured by mixing slurries of cement with preformed aqueous foams, which are produced by mixing compressed air [GIB 97].

1.2 Structures of foams

Thanks to different manufacturing processes, solid foams can be divided into two types of structures in general : open-cell structure and closed-cell structure. Sometimes these two structures exist in a solid foam simultaneously. FIG. 2 shows a couple of foams with different structures. For closed-cell foams, because of the presence of cell walls, the fluid, such as air, trapped in cells is restricted to each cell, which leads that there is no fluid flow throughout the foam structure. On the other hand, open-cell foams allow fluid flow across the foam structure.

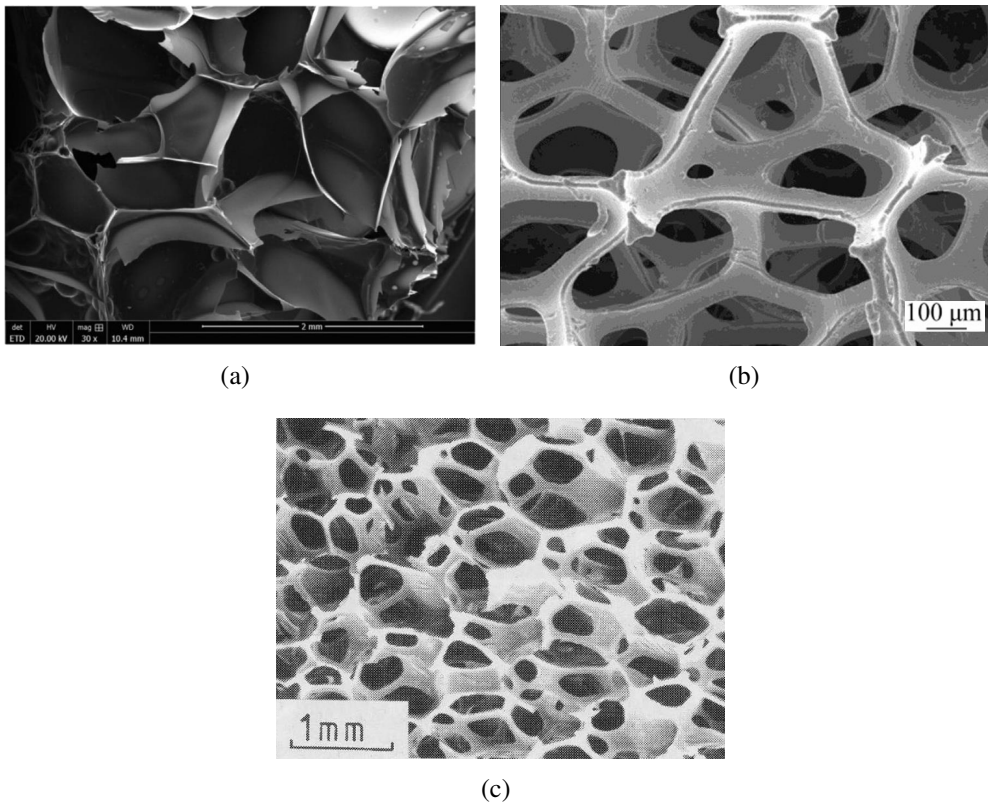


FIGURE 2: Examples of different structures of solid foams : (a) closed-cell carbon foam [RUI 15]; (b) open-cell nickel foam [FAN 17]; (c) polyether foam with both open and closed cells [GIB 97].

The structure of the foam has a significant influence on its behaviors. The general structural parameters summarized in [SHU 98] are listed below :

- relative number of open cells
- relative foam density
- cell size

- cell shape, or geometrical anisotropy
- cell walls thickness and distribution of solid between struts and faces
- cell constituents

In this thesis, both open-cell foams and closed-cell foams are concerned. The influences of morphological parameters on the effective elastic properties of foams are studied.

1.3 Properties and applications of foams

Solid foams have a series of properties, such as physical, mechanical and thermal properties, which can be measured by the same methods as those used for fully dense solids [GIB 97]. Foam materials bring new possibilities in terms of functional properties, which greatly extend the range of the properties for engineering. For example, foams fill the gaps and push the limits of *Ashby's* material performance map (shown in FIG. 3 [ASH 13]) for mechanical properties.

This enormous extension of properties makes it possible to produce applications which can not easily be made by fully dense solids. Due to the low thermal conductivity, the largest single application for polymeric and glass foams is as thermal insulation [PLA 05, COQ 06, BAI 08, KAE 10], which is cheap and reliable and can be better than the expensive vacuum-based methods. Foams applied no matter in disposable coffee cups, or in transport systems, in modern buildings and in the booster rockets for the space shuttle all avail of the low thermal conductivity. The low strengths and large compressive strains make foams excellent for energy absorbing applications. Foams used as packages can absorb the energy of impacts generated by deceleration without subjecting the contents to damaging stresses. Meanwhile the low density makes the package light, which reduce handing and shipping costs. The low stiffness makes foams ideal for a wide range of cushioning applications. Metallic foams are widely used in the automotive industry due to their remarkable energy absorption [MIY 02, RAJ 08, ILU 13, JUN 15, FIS 16] and vibration damping [YIN 14]. Many natural foam materials, such as wood, cancellous bone and coral, support large static and cyclic loads for long periods of time [GIB 97]. People have been using the natural foams or the man-made structural foams inspired by the natural ones. Moreover foams are also used as buoyancy materials [GIB 97], sandwich panels [JIN 16], high-temperature applications [LU 99, FEN 04, GAU 07, MEY 16], catalyst carrier [CIA 10], porous electrode for fuel cell [SIN 00, CIA 10] and so on.

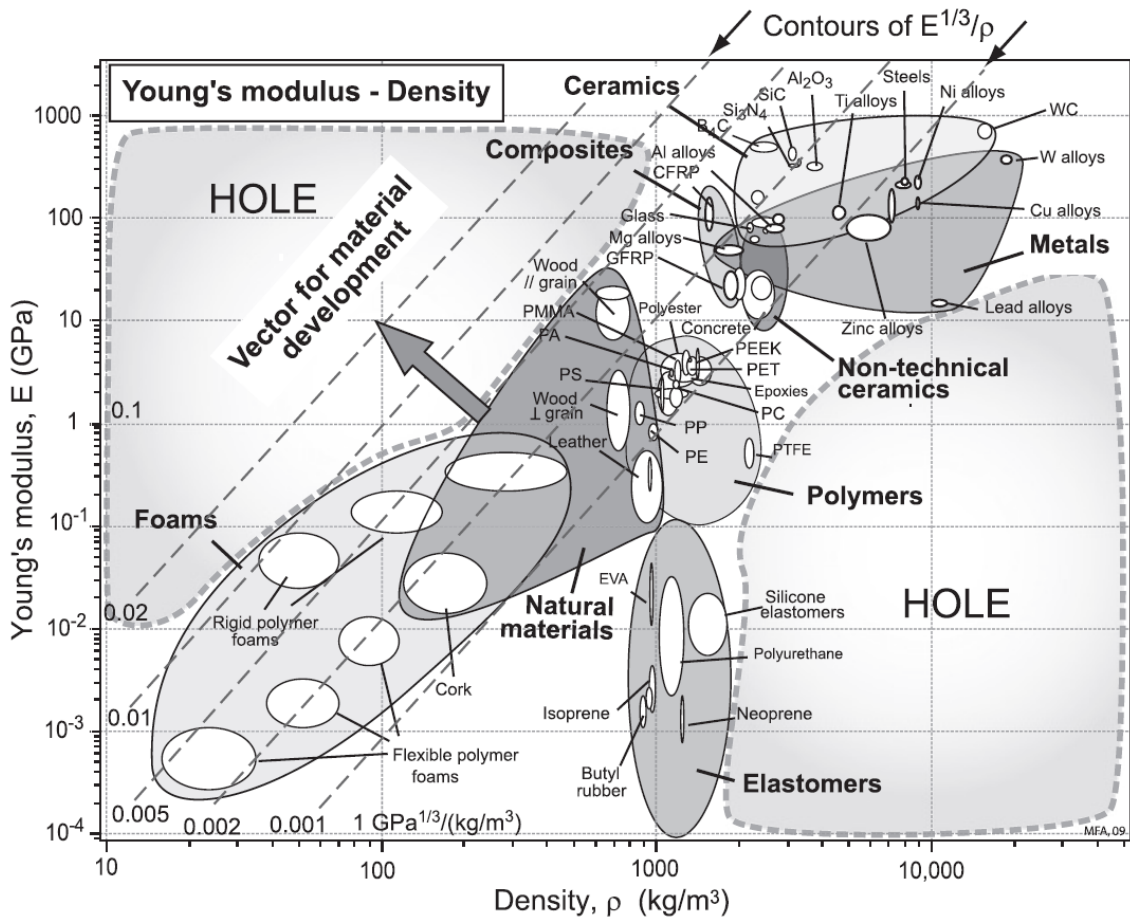


FIGURE 3: Ashby's material map for the modulus-density space [ASH 13].

2 Review of previous work to foams

The name “cell” was proposed first by Robert Hooke to describe the repetitive shape of foam materials when observing the structure of cork wood by microscope [ROM 08]. [THO 42] considered the polyhedral tetrakaidecahedron as the cells in order to obtain the most efficient foam structure by minimizing the cell wall area. [PLA 73] made the contribution to creating the rules for the connectivity of the cells in foam systems. Since then, studies on foam materials and their cells have never stopped, including the study of mechanical properties of foams.

Experimental, theoretical and modeling studies on mechanics of foams have been published in numerous pioneering work, such as [GIB 97, KRA 94, ZHU 97b, ZHU 97a, SHA 94, MUK 99a, LU 99, HAR 99, GRE 98, WAR 97, MIL 00, HAN 98], etc. They have contributed to a good understanding of a series of mechanics problems. They laid the theoretical foundation for the study of the mechanical properties of foam materials and provided guidance for the current investigation.

With the increasing demands for foam materials and the expanding fields of their

applications, foam materials are attracting more and more attention. The studies on their diverse behaviors are also expanding and deepening. [BAD 00, GAI 14, GAI 15, BAR 14b, GON 05, JIN 16] focused on the deformation mechanisms, including the different stages of deformation, and the failure mechanism. [GON 05, CHE 15, SON 10, LI 14b, GRE 00, MIR 16] analyzed the influence of the morphology on the mechanical properties. [FIS 16, GAI 15, ILU 13, MIY 02, FAN 17, JUN 15, RAJ 08] concentrated on the energy absorption applications of foams. Some interesting previous work in both experimental studies and modeling studies will be introduced as follows.

2.1 Experimental studies

Usually the quasi-static response and dynamic loading are considered for experimental studies. And the complete deformation is taken into account in general, instead of focusing on a stage. [NIE 00] studied the mechanical properties of open-cell aluminum foams with different morphologies in compression. Density has been proven to be the primary variable which controls the mechanical properties, which is shown in FIG. 4. Furthermore, the differences in properties caused by different cell shape and size have been explained with theoretical models. [CAO 06] experimentally investigated the influence of cell

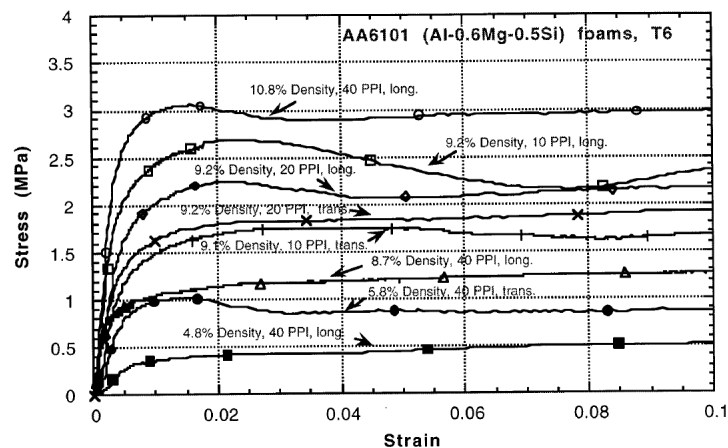


FIGURE 4: Stress-strain curves with different densities and orientations for Al foam in compression [NIE 00].

size on the quasi-static and dynamic compressive responses of open-cell aluminum foams by MTS 810 system and split Hopkinson pressure bar, respectively. Besides the relative density, the cell size also has a significant effect of the elastic moduli and compressive strengths not only under quasi-static loading but also under dynamic loading. Moreover, the cell size is also an important factor that affects the strain rate sensitivity of the foams. The conclusion has been drawn that the foam with middle cell size has the highest elastic modulus, the highest flow strength and the most significant strain rate sensitivity. Using X-ray tomography, [JAN 09] observed the evolution of crushing in compression at slow displacement rates along the rise and traverse directions. In both directions, a nearly linear

response has been found initially, which is followed by an extensive load plateau. It starts to enter the densification stage when the average strain is about 55%. The limit load, the buckling and collapse of cells and collapsing bands have been analyzed to show the whole crushing process. The typical compressive response is presented in FIG. 5. FIG. 6 corresponds to the full cross-section deformed configurations corresponding to each stage in FIG. 5. FIG. 7 and FIG. 8 show the different deformed configurations of site A and site B at different stages (site A and site B are marked in FIG. 6). [BAR 14b] studied the

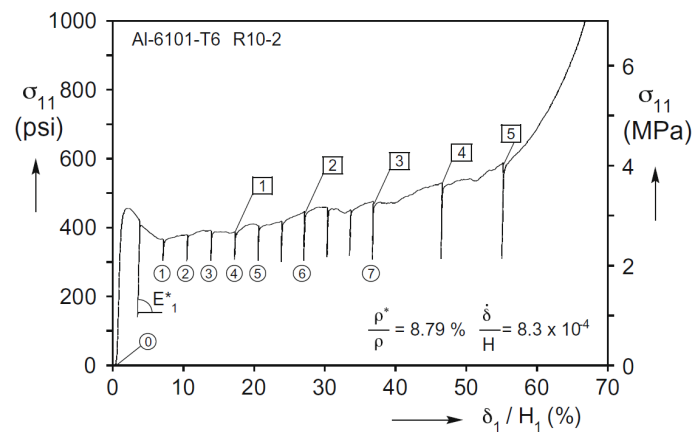


FIGURE 5: Typical compressive response of an aluminum open-cell foam [JAN 09].

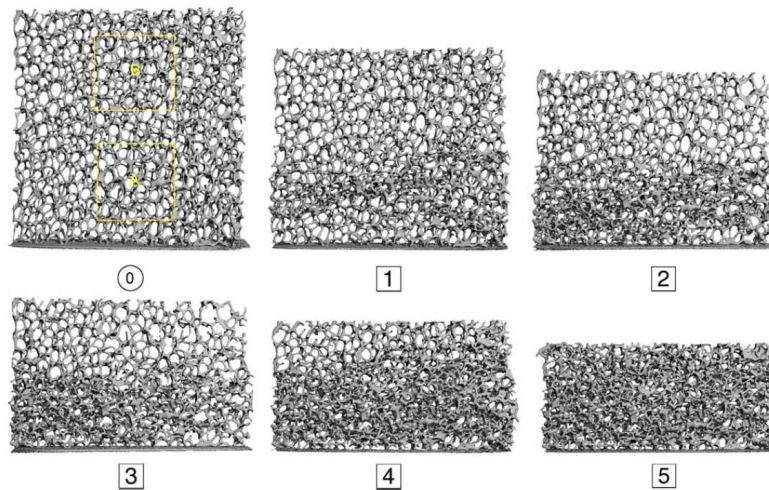


FIGURE 6: Sequence of full cross-section deformed configurations corresponding to each stage in FIG. 5 [JAN 09].

direct and stationary impact of aluminum open-cell foams at impact speed in the range of 20-160 m/s. At different impact speeds, foam specimens present different deformation mechanism. Planar shocks are observed at high velocities (60 m/s or higher) which

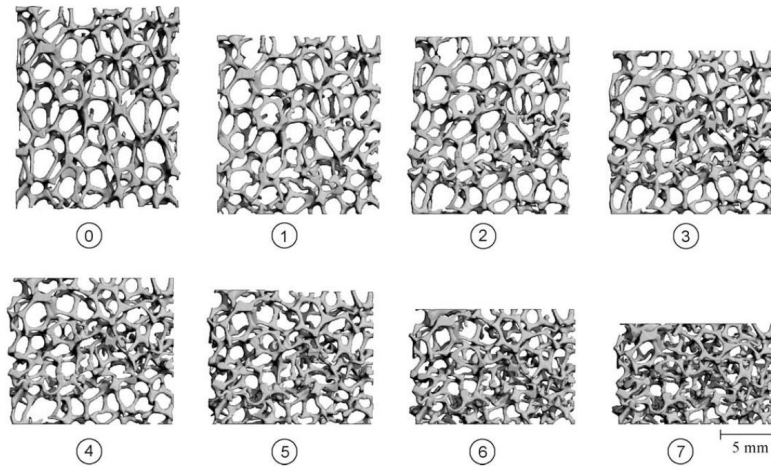


FIGURE 7: Sequence of deformed configurations of site A corresponding to each stage in FIG. 5 [JAN 09].

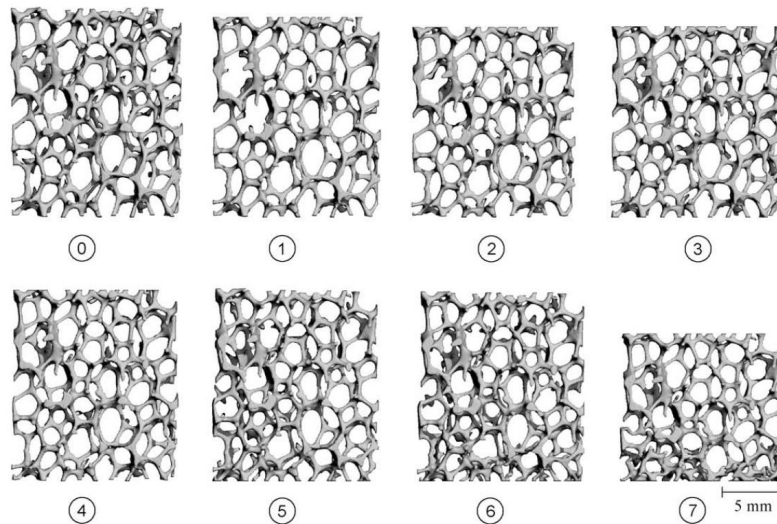


FIGURE 8: Sequence of deformed configurations of site B corresponding to each stage in FIG. 5 [JAN 09].

propagates at well-defined velocities until the specimen is crushing. There is a linear relationship between the shock speed and impact speed. With the increase of impact velocity, the compaction energy dissipation across the shock increases as well. When the impact velocity is lower than 40 m/s, the deformation response is similar to that under quasi-static crushing, and the compaction energy dissipation is significantly smaller than that at high impact velocity. [GAI 15] investigated the energy absorption of open-cell foams with different relative densities under both quasi-static crushing and dynamical impact. Linear increases of the limit of plateau stresses and the energy absorbed have been found under quasi-static crushing while the densification strains presents a linear decrease. The

influence of the strain rates on the quasi-static and dynamic compression stress-strain curves of foams has been exhibited in FIG. 9 in [WAN 06]. Similar investigations of the effect of the strain rates can be also found in [YI 01, DAN 00, MUK 99b], etc.

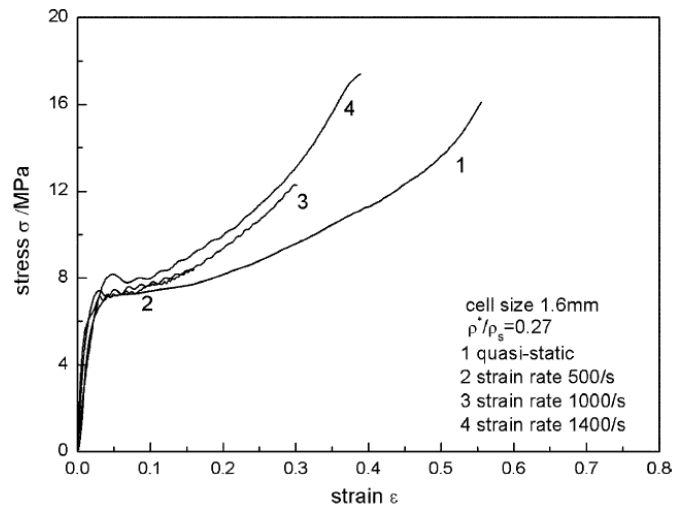


FIGURE 9: Stress-strain curves of aluminum foams at different strain rates [WAN 06].

2.2 Modeling studies

Thanks to the complicated microstructure and unknown microstructural properties, modeling and simulating the foams are quite difficult [ROM 08]. A representative unit cell was usually considered to stand for the cellular structure. 2D foams have been modeled as honey comb structures [GIB 82b, WAR 87, OVE 98], while 3D foams have been considered as cubic cells [GIB 82a], tetrahedral cells [WAR 88], pentagonal dodecahedrons [MEN 75], tetrakaidecahedrons [WAR 97, LI 14a], etc.

A BBC lattice model of tetrakaidecahedral cells has been generated to represent foams in [ZHU 97a, MIL 99]. The contributions of cell face tensions and edge bending have been discussed. The elastic and plastic properties have been analyzed. The influence of non-uniform cell wall thickness on stiffness of Kelvin closed-cell foams has been discussed in [GRE 00]. The stiffness of closed-cell cellular solids has been proven that is not sensitive to the variations of the wall thickness. [CHE 15] also reported the similar investigation of cell wall thickness variation. The influence of the cell irregularity on the elastic properties of open-cell foams has been investigated in [ZHU 00]. The more irregular the foams are, their effective Young's modulus and shear modulus are larger at constant overall relative density. While the bulk modulus decrease with the increase of degree of cell irregularity. Poisson's ratio shows independence. Different isotropic random closed-cell foam models based on Voronoi tessellations and level-cut Gaussian random fields have been generated in [ROB 01] and the dependence of the Young's modulus and Poisson's ratio on density and microstructure has been computed. A power law $E \propto \rho^n$ ($1 < n < 2$)

is used to describe the results for the closed-cell cellular materials. [GAN 05] estimated the effect of the relative density on the Young's modulus, Poisson's ratio and bulk modulus of foams using the finite element analysis. The failure mechanism has also been studied. In [LI 06], the influence of cell shape and strut cross-sectional area variations on the elastic properties of three-dimensional open-cell foams has been analyzed. The dynamic crushing responses of 3D closed-cell foams based on Voronoi random model are reported in [SON 10, LI 14b]. In the literatures, the influences of numerous variables, such as relative density, inertia of cell walls, the cell shape irregularity, strain hardening and impact loading on the plateau stress and the deformation model have been investigated. A new tetrakaidecahedra structure has been constructed in [NAM 10]. The evaluation of the stiffness and mechanical response under large strain have been conducted. Comparing to the cruciform-pyramidal and cubic-spherical foam models, tetrakaidecahedral foam has higher crushing resistance and energy absorption. In [GAI 12], foam structures have been generated using realistic random soap froth with N^3 cells. The ligaments are modeled straight but with non-uniform cross sectional area distributions. The compressive responses, including the complete response from the initial elastic regime to the extended stress plateau to densification, have been simulated in both the rise and transverse directions. Random soap froth has been generated using the Surface Evolver software in [GAI 14]. Appropriate distributions of solid are added to the linear edges of the cellular structure to match those in the real foams. Beam elements are dressed for the ligaments. The crush behavior including the formation and evolution, the force, the shock, the strain and the energy absorbed have been studied. Hexagonal honeycombs have been generated in [MOU 14] and the effects of cell wall material strain hardening and density functional gradation on in-plane constant-velocity dynamic crushing response and impact behavior have been investigated. Material point method has been used to study numerically the influences of porous density and strain-rate effect on dynamical responses of aluminum foam in [LIU 14]. The plateau stress level increases with the increase of the relative density, while the plateau width decreases. The influence of loading rate on the compressive properties of open-cell foams has been numerically studied in [LI 14a]. The influence of the impact velocity and the relative density on the deformation modes, energy absorption, plateau stress and densification strain has been analyzed qualitatively. The failure modes and patterns are found and proven to be caused by different impact velocities. The influence of the relative density and irregularity of Voronoi closed-cell foam models on the elastic and plastic properties are reported in [BAR 14a]. A multiaxial "plasticity" criterion of the simulation of the macroscopic behavior of light closed-cell foams is developed in [YE 15]. Numerical calculations of relative Young's modulus on computer-generated Kelvin and random microstructures of closed-cell foams and inverse foams have been performed in [PAB 18], where the numerical results have been compared to analytical models. The differences of effective elastic properties between accurate volumetric models and corresponding beam models of a Kelvin has been performed in [STO 13b]. They also defined several morphological parameters and discussed the effect of these geometry details on the elastic properties. By implicit functions, [STO 13a] proposed an approach to generate models of ceramic open-cell foams with simple variable thickness objects. Ca-

vities within struts and nodes have also been taken into account. The numerical structures are verified with CT data of real foams quantitatively. [STO 15] focused on the modeling of the structure of foams. The geometric details, such as strut thickness variations, strut curvature, node thickness, node and strut cavities, and anisotropy have been considered. The influences of them have been studied using the finite element method together with a computational homogenisation technique. Besides, [STO 16] also studied the the yielding or failure of different ductile or brittle open-cell Kelvin foams with several local strength and yield criteria.

Finally, the reader is warned that some literary work mentioned in this chapter will be mentioned again in the introduction to the following chapters in order to make each chapter self-contained.

3 Scope of the thesis

On the basis of previous work, the present work aims to study the effective elastic properties of foams systematically, including the study on the influence of the morphology with a Voronoi-based method and the micromechanical modeling based on the proposed Hill's lemma periodic computational homogenization approach. The manuscript develops in the following way :

- The first chapter deals with the relevant knowledge on homogenization, which includes the basic concepts of the constitutive equations and several symmetry classes of materials, the concepts of homogenization and Representative Volume Element (RVE), three classical types of boundary conditions, the bounding methods and analytical models, and the usual computational homogenization approach.
- Considering that microstructures of foam models are generally simplified in previous literatures, the second chapter aims at investigating the influences of the morphological parameters on the effective elastic properties of Kelvin open-cell foams. The Hill's lemma periodic computational homogenization approach is developed, which has the significant advantages comparing to the usual methods. The innovative approach based on Voronoi diagram for the generation of foam materials is introduced. New generic analytical laws are deduced for Kelvin open-cell foams by considering the morphological parameters.
- Due to the lack of specific methods for foam models in previous literatures, the third chapter focuses on the determination of the RVE of irregular open-cell foam models and the importance of choosing the RVE parameters, i.e. the number of realizations and the volume of RVE, on estimating the effective elastic properties. The efficiencies of a number of approaches are compared and some recommendations and improvements are proposed.
- The fourth chapter performs the investigations about the influences of the RVE parameters, the different kinematic modelings and the relative density on the effective

elastic properties of irregular closed-cell foam models. The simulation results of our generated models are compared with those of the tomography reconstruction model and the experimental results.

- Finally, the general conclusions are carried out with some prospects.

Chapter 1

Homogenization for linear elasticity

In this chapter, the relevant knowledge on homogenization is addressed. The first part introduces the basic concepts of the constitutive equations and several important symmetry classes of materials. The second part deals with the concepts of homogenization and Representative Volume Element (RVE), and three classical types of boundary conditions. The third part focuses on the bounding methods and analytical models for elastic properties. The last part presents the usual computational homogenization approach, which will be compared with our proposed approach in the next chapter.

Contents

1	Basic concepts	15
1.1	Constitutive equations	15
1.2	Material symmetries and anisotropy	16
2	Homogenization	19
2.1	The concept of Homogenization	19
2.2	Representative volume element	20
2.3	Boundary conditions	21
3	Analytical techniques for elastic properties	22
3.1	Bounding methods	23
3.2	Analytical models	25
4	Usual computational homogenization approach based on the finite element method	27

1 Basic concepts

1.1 Constitutive equations

Focussing on the case of small perturbation, for elastic materials, Hooke's law stands for the material behavior and relates the unknown stresses and strains. The general equation for Hooke's law is

$$\boldsymbol{\sigma} = \mathbb{C} : \boldsymbol{\epsilon}, \quad (1.1)$$

where $\boldsymbol{\sigma}$ is the second-order *Cauchy* stress tensor, $\boldsymbol{\epsilon}$ is the second-order infinitesimal strain tensor and \mathbb{C} is the fourth-order elastic stiffness tensor, which consists of 81 components for three-dimensional problems. One may also write it as

$$\boldsymbol{\epsilon} = \mathbb{S} : \boldsymbol{\sigma}, \quad (1.2)$$

where the tensor \mathbb{S} represents the inverse of tensor \mathbb{C} , called the compliance tensor. One can obtain

$$\mathbb{C} :: \mathbb{S} = \mathbb{I} \quad (1.3)$$

with \mathbb{I} , fourth-order identity tensor operating on symmetric second-order tensors such that :

$$\mathbb{I} = \frac{1}{2} (\delta_{ik}\delta_{jl} + \delta_{il}\delta_{jk}) \mathbf{e}_i \otimes \mathbf{e}_j \otimes \mathbf{e}_k \otimes \mathbf{e}_l \quad \text{with } i, j, k, l = 1, 2, 3. \quad (1.4)$$

δ is the Kronecker delta function, defined as

$$\delta_{ij} = \begin{cases} 0 & \text{for } i \neq j \\ 1 & \text{for } i = j \end{cases}. \quad (1.5)$$

Each component of stress σ_{ij} is linearly dependent upon every component of strain ϵ_{kl} and vice versa. Since all directional indices may assume values 1, 2, and 3, one obtains 9 relations. Each of this relations involves on component of stress and nine components of strain. Since the stress tensor is symmetrical, i.e. $\sigma_{ij} = \sigma_{ji}$, only six of these equations are independent. This is also valid for the strain. The stiffness tensor has the following minor symmetries which result from the symmetry of the stress and strain tensor :

$$C_{ijkl} = C_{jikl} = C_{ijlk} = C_{jilk}, \quad (1.6)$$

where C_{ijkl} are the components of the stiffness tensor. This reduces the number of independent components from 81 to 36. Moreover, the existence of a unique strain energy potential requires that $C_{ijkl} = C_{klij}$. Hence the number of independent components in the stiffness tensor reduces to 21.

For simplicity, it is useful to apply the modified Voigt notation to express the $3 \times 3 \times 3 \times 3$ stiffness tensor \mathbb{C} as a 6×6 stiffness matrix $[\mathbb{C}]$ in a given frame.

Hence a symmetric second order tensor \mathbf{a} can be represented in a vector form as $\{\mathbf{a}\} =^T \{a_{11}, a_{22}, a_{33}, \sqrt{2}a_{23}, \sqrt{2}a_{13}, \sqrt{2}a_{12}\}$ with a_{ij} are its components in the basis $(\mathbf{e}_i)_{i=1,2,3}$. EQ. 1.1 can also be expressed as follows in the given frame :

$$\begin{Bmatrix} \sigma_{11} \\ \sigma_{22} \\ \sigma_{33} \\ \sqrt{2}\sigma_{23} \\ \sqrt{2}\sigma_{13} \\ \sqrt{2}\sigma_{12} \end{Bmatrix} = \begin{bmatrix} C_{11} & C_{12} & C_{13} & \sqrt{2}C_{14} & \sqrt{2}C_{15} & \sqrt{2}C_{16} \\ & C_{22} & C_{23} & \sqrt{2}C_{24} & \sqrt{2}C_{25} & \sqrt{2}C_{26} \\ & & C_{33} & \sqrt{2}C_{34} & \sqrt{2}C_{35} & \sqrt{2}C_{36} \\ Sym & & & 2C_{44} & 2C_{45} & 2C_{46} \\ & & & & 2C_{55} & 2C_{56} \\ & & & & & 2C_{66} \end{bmatrix} \begin{Bmatrix} \varepsilon_{11} \\ \varepsilon_{22} \\ \varepsilon_{33} \\ \sqrt{2}\varepsilon_{23} \\ \sqrt{2}\varepsilon_{13} \\ \sqrt{2}\varepsilon_{12} \end{Bmatrix}. \quad (1.7)$$

1.2 Material symmetries and anisotropy

Anisotropy stands for the directional dependence of material properties. The different types of material anisotropy are determined by the existence of symmetries in the internal structure of the material. The more the internal symmetries, the simpler the structure of the stiffness tensor. Several important symmetry classes are introduced, corresponding the anisotropy and the structure of the stiffness tensor.

1.2.1 Isotropic media

In the simplest symmetry case of an isotropic elastic solid, the stiffness tensor \mathbb{C} can be rewritten as follows :

$$\mathbb{C} = 3k\mathbb{J} + 2\mu\mathbb{K}, \quad (1.8)$$

with k bulk modulus and μ shear modulus. \mathbb{J} and \mathbb{K} are spherical and deviatoric fourth order tensorial projectors, such that :

$$\mathbb{J} = \frac{1}{3}\delta_{ij}\delta_{kl}\mathbf{e}_i \otimes \mathbf{e}_j \otimes \mathbf{e}_k \otimes \mathbf{e}_l \quad (1.9)$$

and

$$\mathbb{K} = \mathbb{I} - \mathbb{J}. \quad (1.10)$$

In modified Voigt notation, $[\mathbb{J}]$ and $[\mathbb{K}]$ are the matrix representations of the classical isotropy basis components of fourth order symmetric tensor, which can written as :

$$[\mathbb{J}] = \begin{bmatrix} 1/3 & 1/3 & 1/3 & 0 & 0 & 0 \\ 1/3 & 1/3 & 1/3 & 0 & 0 & 0 \\ 1/3 & 1/3 & 1/3 & 0 & 0 & 0 \\ 0 & 0 & 0 & 0 & 0 & 0 \\ 0 & 0 & 0 & 0 & 0 & 0 \\ 0 & 0 & 0 & 0 & 0 & 0 \end{bmatrix}, \quad (1.11)$$

and

$$[\mathbb{K}] = \begin{bmatrix} 2/3 & -1/3 & -1/3 & 0 & 0 & 0 \\ -1/3 & 2/3 & -1/3 & 0 & 0 & 0 \\ -1/3 & -1/3 & 2/3 & 0 & 0 & 0 \\ 0 & 0 & 0 & 1 & 0 & 0 \\ 0 & 0 & 0 & 0 & 1 & 0 \\ 0 & 0 & 0 & 0 & 0 & 1 \end{bmatrix}. \quad (1.12)$$

The stiffness tensor in modified Voigt notation has the form :

$$[\mathbb{C}] = \begin{bmatrix} C_{11} & C_{12} & C_{12} & 0 & 0 & 0 \\ & C_{11} & C_{12} & 0 & 0 & 0 \\ & & C_{11} & 0 & 0 & 0 \\ & Sym & & C_{11} - C_{12} & 0 & 0 \\ & & & & C_{11} - C_{12} & 0 \\ & & & & & C_{11} - C_{12} \end{bmatrix}. \quad (1.13)$$

1.2.2 Cubic symmetric media

As the simplest anisotropic case, cubic symmetric media have 3 independent components, and the stiffness tensor \mathbb{C} can be written in the form :

$$\mathbb{C} = 3k\mathbb{J} + 2\mu^a\mathbb{K}_a + 2\mu^b\mathbb{K}_b, \quad (1.14)$$

where μ^a and μ^b are two shear moduli. Introduce the tensor $\mathbb{W} = \mathbf{e}_1 \otimes \mathbf{e}_1 \otimes \mathbf{e}_1 \otimes \mathbf{e}_1 + \mathbf{e}_2 \otimes \mathbf{e}_2 \otimes \mathbf{e}_2 + \mathbf{e}_3 \otimes \mathbf{e}_3 \otimes \mathbf{e}_3$ by considering $\mathbf{e}_1, \mathbf{e}_2, \mathbf{e}_3$ are the unit vectors in the three orthogonal directions of cubic symmetry. \mathbb{K}_a and \mathbb{K}_b are defined as :

$$\mathbb{K}_a = \mathbb{W} - \mathbb{J} \quad (1.15)$$

and

$$\mathbb{K}_b = \mathbb{K} - \mathbb{K}_a = \mathbb{I} - \mathbb{W}. \quad (1.16)$$

The stiffness tensor in modified Voigt notation can be written as :

$$[\mathbb{C}] = \begin{bmatrix} C_{11} & C_{12} & C_{12} & 0 & 0 & 0 \\ & C_{11} & C_{12} & 0 & 0 & 0 \\ & & C_{11} & 0 & 0 & 0 \\ & Sym & & 2C_{44} & 0 & 0 \\ & & & & 2C_{44} & 0 \\ & & & & & 2C_{44} \end{bmatrix}. \quad (1.17)$$

1.2.3 Transversely isotropic media

Transversely isotropic media can be characterized by the existence of a single plane of isotropy and one single axis of rotational symmetry, which is vertical to the plane. Any plane containing the axis of symmetry stands for a plane of mirror symmetry. Assuming that \mathbf{n} is a unit vector parallel to the axis of transverse isotropy and $\mathbf{i}_T = \mathbf{i} - \mathbf{n} \otimes \mathbf{n}$ is the identity tensor in the transverse plane. The stiffness tensor of the transversely isotropic media can be written in the form :

$$\mathbb{C} = \left[E^l + 4(\nu^l)^2 K \right] \mathbb{E}_L + 2K \mathbb{J}_T + 2\sqrt{2}\nu^l K (\mathbb{F} + {}^T \mathbb{F}) + 2\mu^t \mathbb{K}_T + 2\mu^l \mathbb{K}_L, \quad (1.18)$$

where E^l is the longitudinal Young's modulus, ν^l is the longitudinal Poisson's ratio, K is the bulk modulus in the plane, μ^t and μ^l are the transverse shear modulus and longitudinal shear modulus, respectively. The fourth-order tensors are defined as :

$$\mathbb{E}_L = \mathbf{n} \otimes \mathbf{n} \otimes \mathbf{n} \otimes \mathbf{n}, \quad (1.19)$$

$$\mathbb{J}_T = \frac{1}{2} \mathbf{i}_T \otimes \mathbf{i}_T, \quad (1.20)$$

$$\mathbb{F} = \frac{1}{\sqrt{2}} \mathbf{i}_T \otimes \mathbf{n} \otimes \mathbf{n}, \quad (1.21)$$

$$\mathbb{K}_T = \mathbb{I}_T - \mathbb{J}_T \quad (1.22)$$

and

$$\mathbb{K}_L = \mathbb{K} - \mathbb{K}_T - \mathbb{K}_E, \quad (1.23)$$

where \mathbb{I}_T is the fourth-order identity tensor in the transverse plane and $\mathbb{K}_E = \frac{1}{6} (2\mathbf{n} \otimes \mathbf{n} - \mathbf{i}_T) \otimes (2\mathbf{n} \otimes \mathbf{n} - \mathbf{i}_T)$.

Supposing e_3 is the axis of symmetry, the stiffness tensor in modified Voigt notation for transversely isotropic media has the form :

$$[\mathbb{C}] = \begin{bmatrix} C_{11} & C_{12} & C_{13} & 0 & 0 & 0 \\ & C_{11} & C_{13} & 0 & 0 & 0 \\ & & C_{33} & 0 & 0 & 0 \\ & Sym & & 2C_{44} & 0 & 0 \\ & & & & 2C_{44} & 0 \\ & & & & & 2C_{66} \end{bmatrix} \quad (1.24)$$

with $C_{12} = C_{11} - 2C_{66}$.

1.2.4 Orthotropic media

Orthotropic media are characterized by three mutually orthogonal planes of symmetry. If the axes of a Cartesian reference coordinate system (e_1, e_2, e_3) are aligned within the symmetry planes, the stiffness matrix of the orthotropic system has nine independent components and reads :

$$[C] = \begin{bmatrix} C_{11} & C_{12} & C_{13} & 0 & 0 & 0 \\ & C_{22} & C_{23} & 0 & 0 & 0 \\ & & C_{33} & 0 & 0 & 0 \\ & Sym & & 2C_{44} & 0 & 0 \\ & & & & 2C_{55} & 0 \\ & & & & & 2C_{66} \end{bmatrix}. \quad (1.25)$$

The compliance matrix can be written as :

$$[S] = \begin{bmatrix} \frac{1}{E_{11}} & -\frac{\nu_{21}}{E_{22}} & -\frac{\nu_{31}}{E_{33}} & 0 & 0 & 0 \\ -\frac{\nu_{12}}{E_{11}} & \frac{1}{E_{22}} & -\frac{\nu_{32}}{E_{33}} & 0 & 0 & 0 \\ -\frac{\nu_{13}}{E_{11}} & -\frac{\nu_{23}}{E_{22}} & \frac{1}{E_{33}} & 0 & 0 & 0 \\ 0 & 0 & 0 & \frac{1}{2G_{23}} & 0 & 0 \\ 0 & 0 & 0 & 0 & \frac{1}{2G_{31}} & 0 \\ 0 & 0 & 0 & 0 & 0 & \frac{1}{2G_{12}} \end{bmatrix}, \quad (1.26)$$

where E_{ii} is the Young's modulus along axis i , G_{ij} is the shear modulus in direction j on the plane whose normal is in direction i , and ν_{ij} is the Poisson's ratio that corresponds to a contraction in direction j when an extension is applied in direction i .

2 Homogenization

2.1 The concept of Homogenization

Most "natural" materials as well as many engineering materials are heterogeneous. A hypothesis of continuity of a material was introduced. In this hypothesis, the actual constitution of the material is idealized to be continuous by a notion of statistical average [KUR 04]. A homogeneous medium is then represented by considering every point over the medium has identical properties (see FIG. 1.1). The concept of leading a "heterogeneous" medium to be "homogeneous" is called homogenization.

For a heterogeneous medium, the heterogeneity manifests as the variations of the physical properties with different positions, which can be either continuous or discontinuous.

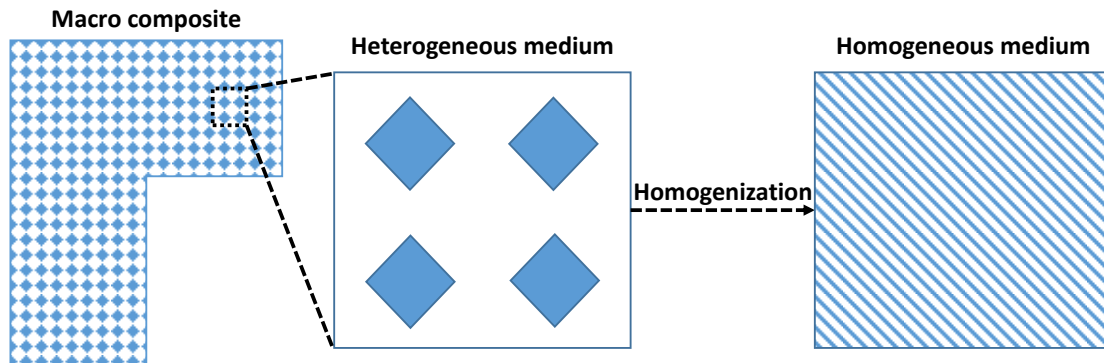


FIGURE 1.1: Illustration : A macro composite, a heterogeneous medium from the composite and the corresponding homogeneous medium.

For the foams, the variations of the properties are considered in a discontinuous way, i.e. the properties vary at the interfaces between the solid phase and the air phase, and the solid phase is homogeneous and isotropic.

2.2 Representative volume element

The various definitions of the representative volume element (RVE) have been proposed for decades. [HIL 63] revealed that for a given material the “theoretical RVE” is a sample should be large enough to include a sufficient number of microstructural heterogeneities of the composite and to reflect the effective properties which are independent of boundary conditions. [BER 68] emphasized the role of statistical homogeneity in a volume-averaged sense. A review on analysis of composite materials can be found in [HAS 83], where a scale separation principle was proposed as : $L_{MICRO} \ll L_{MINI} \ll L_{MACRO}$. L_{MICRO} is the size of microstructural heterogeneities. L_{MINI} is referring to the size of the RVE, also called the mesoscale. L_{MACRO} represents the size of the whole composite. [SAB 92] pointed out that only if the homogenized moduli tend towards those of a similar periodic medium can the classical RVE definition hold for a heterogeneous, i.e. the response over a RVE should be independent of boundary conditions. [DRU 96] proposed the idea of minimizing the RVE size, that the RVE is the smallest material volume to make the apparent and effective properties consistent. From the practical standpoint, [GUS 97] and [KAN 03] considered that the “numerical RVE” would be defined as the smallest volume element which has the macroscopic properties. [GUS 97] proposed the first determination criterion to estimate the stability of the apparent properties with the increase of the heterogeneities. [KAN 03] presented that the number of random realizations of the volume element (with satisfactory confidence in the results) is also necessary to the RVE definition by algorithm. The effective properties would possibly be equal for small RVEs after a sufficient number of realizations and large RVEs after fewer realization. Furthermore, a method which can determine the minimal RVE size was proposed using the ergodicity hypothesis [OST 98, OST 02]. Other RVE determination criteria have also

been reported in [GIT 07, TRI 06, PEL 09, SAL 12, GHO 12, MOU 13].

In this dissertation, the statistical methods proposed in [KAN 03] and [MOU 13] are implemented to determine the RVEs for random foams.

2.3 Boundary conditions

Consider a RVE Ω , made of an elastic bulk medium and a porous phase. Conditions are prescribed at its boundary $\partial\Omega$ to estimate its overall properties. There are three classical types of boundary conditions [KAN 03, KAN 06, DIR 12] :

- *Kinematic uniform boundary condition (KUBC)* : The displacement \mathbf{u} is imposed at a point \mathbf{x} belong to the boundary $\partial\Omega$:

$$\mathbf{u} = \bar{\boldsymbol{\epsilon}} \cdot \mathbf{x} \quad \forall \mathbf{x} \in \partial\Omega. \quad (1.27)$$

$\bar{\boldsymbol{\epsilon}}$ is a second-order macroscopic strain tensor which is symmetric and independent of \mathbf{x} . It implies that :

$$\langle \boldsymbol{\epsilon} \rangle \hat{=} \frac{1}{\Omega} \int_{\Omega} \boldsymbol{\epsilon} \, d\Omega = \bar{\boldsymbol{\epsilon}}. \quad (1.28)$$

The sign $\hat{=}$ denotes the definition of the left quantity. The macroscopic stress tensor is then defined as the spatial average of the local stress field and obtained solving a boundary value problem (BVP) with finite element method (FEM), for example :

$$\bar{\boldsymbol{\sigma}} \hat{=} \langle \boldsymbol{\sigma} \rangle = \frac{1}{\Omega} \int_{\Omega} \boldsymbol{\sigma} \, d\Omega. \quad (1.29)$$

- *Static uniform boundary condition (SUBC)* : The traction vector is prescribed for any point \mathbf{x} on $\partial\Omega$:

$$\boldsymbol{\sigma} \cdot \mathbf{n} = \bar{\boldsymbol{\sigma}} \cdot \mathbf{n} \quad \forall \mathbf{x} \in \partial\Omega. \quad (1.30)$$

with $\bar{\boldsymbol{\sigma}}$ a symmetric second-order macroscopic stress tensor which does not depend on \mathbf{x} . \mathbf{n} denotes the vector normal to $\partial\Omega$ at \mathbf{x} . It follows :

$$\langle \boldsymbol{\sigma} \rangle \hat{=} \frac{1}{\Omega} \int_{\Omega} \boldsymbol{\sigma} \, d\Omega = \bar{\boldsymbol{\sigma}}. \quad (1.31)$$

The macroscopic strain tensor is then defined as the spatial average of the local strain field and obtained solving the BVP with finite element computation :

$$\bar{\boldsymbol{\epsilon}} \hat{=} \langle \boldsymbol{\epsilon} \rangle = \frac{1}{\Omega} \int_{\Omega} \boldsymbol{\epsilon} \, d\Omega. \quad (1.32)$$

- *Periodic boundary condition (PBC)* : The local strain field $\boldsymbol{\epsilon}$, at a point \mathbf{x} within the RVE can be divided into a macroscopic strain tensor $\bar{\boldsymbol{\epsilon}}$, and a correction

field ϵ' , which stands for the presence of heterogeneities, i.e. $\epsilon(\mathbf{x}) = \bar{\epsilon} + \epsilon'(\mathbf{x})$. The fluctuations strain ϵ' is derived from a fluctuations displacement field \mathbf{u}' , i.e. $\epsilon' = 1/2(\nabla\mathbf{u}' + {}^T\nabla\mathbf{u}')$. The perturbation field \mathbf{u}' is a periodic field (its components are equal over two opposite sides of the RVE). ϵ' has a vanishing average $\langle\epsilon'\rangle = \mathbf{0}$. It follows that the local displacement \mathbf{u} can be decomposed for any point \mathbf{x} as :

$$\mathbf{u} = \bar{\epsilon} \cdot \mathbf{x} + \mathbf{u}' \quad \forall \mathbf{x} \in \Omega, \quad \mathbf{u}' \text{ periodic.} \quad (1.33)$$

The traction vector $\boldsymbol{\sigma} \cdot \mathbf{n}$ has opposite values at two homologous points on opposite sides of RVE.

The periodic boundary condition is usually used for periodic heterogeneous media and has been verified to be the most efficient in terms of convergence rate when the RVE size increase in many studies [TER 00, KAN 03, LAR 11, NGU 12]. FIG. 1.2 presents that the increase of the RVE size makes a better evolution of the average properties for all three kinds of boundary conditions, and the periodic boundary condition shows a better estimation than the other two boundary conditions. Because of the efficiency, the periodic boundary condition is imposed in this thesis.

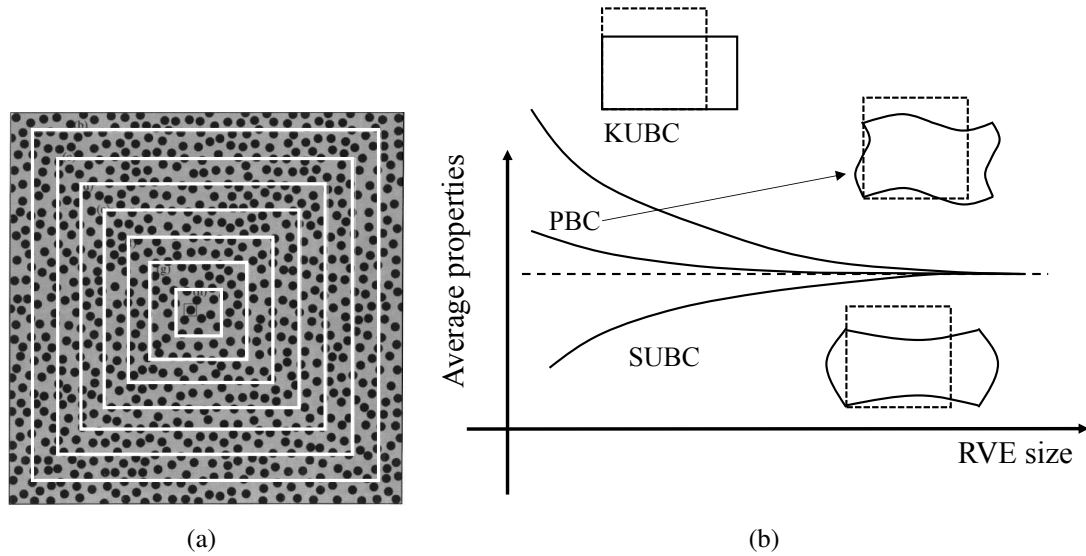


FIGURE 1.2: Illustration of the convergence property with the RVE size shown in [NGU 12] : (a) RVE with different sizes; (b) The convergence of average properties with the increase of RVE size under different boundary condition types.

3 Analytical techniques for elastic properties

In this section, some bounding methods and analytical models for elastic predictions are reviewed.

3.1 Bounding methods

In order to model and estimate the effective elastic properties of composites precisely, one must know :

- the individual elastic moduli of the constituents,
- the volume fraction of each constituent,
- the details of the geometry which show the distributions of the constituents.

Sometimes, the details of the geometry is difficult to obtain. The estimation of the upper and lower bounds on the moduli is then used and considered if omit the details of the geometry. The bounds are powerful and robust to present rigorous upper and lower limits of the properties.

3.1.1 Voigt and Reuss bounds [VOI 89, REU 29]

A power law average of the constituents is defined based on a strictly empirical method :

$$M^{\text{hom}\varpi} = f_1 M_1^{\varpi} + f_2 M_2^{\varpi} + f_3 M_3^{\varpi} + \dots \quad (1.34)$$

where M^{hom} is the effective property of the composite, M_i is the property of the i th constituent, f_i is the volume fraction of the i th constituent, and ϖ is a constant (equals to -1 or +1 generally). The Voigt average is the upper bound :

$$M_V^{\text{hom}} = \sum_{i=1}^n f_i M_i. \quad (1.35)$$

While the Reuss average is the lower bound :

$$M_R^{\text{hom}^{-1}} = \sum_{i=1}^n f_i M_i^{-1}. \quad (1.36)$$

With the upper and lower bounds, an estimate of the actual property is considered as the average of two, called the Voigt-Reuss-Hill average :

$$M_{VRH}^{\text{hom}} = \frac{M_V^{\text{hom}} + M_R^{\text{hom}}}{2}.$$

The Voigt and Reuss averages are taken as the ratio of average stress and strain within the composite. The upper bound and lower bound respectively assume that the strain and the stress are homogeneous in the composite, which are generally unknown and expected to be nonuniform. It brings

$$\mathbb{C}_V^{\text{hom}} = \sum_{i=1}^n f_i \mathbb{C}_i = \mathbb{S}_V^{\text{hom}^{-1}}. \quad (1.37)$$

and

$$\mathbb{C}_R^{\text{hom}^{-1}} = \sum_{i=1}^n f_i \mathbb{C}_i^{-1} = \mathbb{S}_R^{\text{hom}}. \quad (1.38)$$

3.1.2 Hashin-Shtrikman bounds [HAS 63]

The Hashin-Shtrikman bounds allow to estimate the properties for an isotropic media with only the volume fractions of the constituents. Meanwhile it is narrower than the Voigt-Reuss bounds. For a composite with 2 materials, the bulk modulus k and the shear modulus μ are given by :

$$k^{HS\pm} = k_1 + \frac{f_2}{(k_2 - k_1)^{-1} + f_1 \left(k_1 + \frac{4}{3}\mu_1 \right)^{-1}} \quad (1.39)$$

and

$$\mu^{HS\pm} = \mu_1 + \frac{f_2}{(\mu_2 - \mu_1)^{-1} + \frac{2f_1(k_1 + 2\mu_1)}{5\mu_1 \left(k_1 + \frac{4}{3}\mu_1 \right)}}. \quad (1.40)$$

The upper bound is computed when $k_1 > k_2$ while the lower bound is computed when $k_2 > k_1$.

A more general form for composites with more than two phases are [BER 93]

$$k^{HS+} = \Upsilon(\mu_{max}), \quad k^{HS-} = \Upsilon(\mu_{min}) \quad (1.41)$$

and

$$\mu^{HS+} = \Gamma(\xi(k_{max}, \mu_{max})), \quad \mu^{HS-} = \Gamma(\xi(k_{min}, \mu_{min})), \quad (1.42)$$

where

$$\Upsilon(z) = \left\langle \frac{1}{k(r) + \frac{4}{3}z} \right\rangle^{-1} - \frac{4}{3}z,$$

$$\Gamma(z) = \left\langle \frac{1}{\mu(r) + z} \right\rangle^{-1} - z,$$

$$\xi(k, \mu) = \frac{\mu}{6} \left(\frac{9k + 8\mu}{k + 2\mu} \right),$$

and $\langle \rangle$ indicates volume average over the spatially varying $k(r)$ and $\mu(r)$ of the constituents.

3.2 Analytical models

3.2.1 Self consistent method

Usually bounding methods consider only the volume fraction of each constituent and do not depend on any geometry. A more direct approach, namely the self consistent method, is available for the composites in which one phase is dispersion of ellipsoidal inclusions. This method is proposed originally by [HER 54] and [KRÖ 58] for aggregates of crystals and reviewed and elaborated by [HIL 65] and [BUD 65]. This approach takes into account the interaction of phases by considering each phase to be an inclusion in a homogeneous medium which has the overall properties. The basic postulate of the self consistent method shows that

$$\bar{\sigma}^{(1)} - \bar{\sigma} = \mathbb{C}^{\text{hom}} \left(\bar{\epsilon} - \bar{\epsilon}^{(1)} \right), \quad (1.43)$$

and the elementary relation between the phases and the overall average of stress is

$$f_1 \left(\bar{\sigma}^{(1)} - \bar{\sigma} \right) + f_2 \left(\bar{\sigma}^{(2)} - \bar{\sigma} \right) = 0. \quad (1.44)$$

Where the superscripts (1) and (2) as well as the subscripts 1 and 2 denote the inclusion and matrix (the superscripts are used to avoid mixing with the directional indices). According to the above two equations, there is

$$\bar{\sigma}^{(2)} - \bar{\sigma} = \mathbb{C}^{\text{hom}} \left(\bar{\epsilon} - \bar{\epsilon}^{(2)} \right). \quad (1.45)$$

Obviously, both the inclusion and the matrix are considered on the same footing. Taking EQ. 1.43 and EQ. 1.45 together comes

$$\left(\mathbb{C}^{\text{hom}} + \mathbb{C}^{(1)} \right) \bar{\epsilon}^{(1)} = \left(\mathbb{C}^{\text{hom}} + \mathbb{C}^{(2)} \right) \bar{\epsilon}^{(2)} = \left(\mathbb{C}^{\text{hom}} + \mathbb{C} \right) \bar{\epsilon}, \quad (1.46)$$

which can be solved for the effective stiffness of the composite with various particle shapes. This “self consistent scheme” performs well for the dispersed component at low concentrations while the performance is poor at high concentrations when the difference in modulus between the components is large. For the composite with a dispersion of elastic spherical particulates, the effective bulk modulus k^{hom} and the effective shear modulus μ^{hom} of the composite can be solved iteratively by the self consistent scheme :

$$k^{\text{hom}} = k_2 + \frac{f_1 k^{\text{hom}} (k_1 - k_2)}{k^{\text{hom}} + \left(\frac{3k^{\text{hom}}}{3k^{\text{hom}} + 4\mu^{\text{hom}}} \right) (k_1 - k^{\text{hom}})} \quad (1.47)$$

and

$$\mu^{\text{hom}} = \mu_2 + \frac{f_1 \mu^{\text{hom}} (\mu_1 - \mu_2)}{k^{\text{hom}} + \left(\frac{6k^{\text{hom}} + 12\mu^{\text{hom}}}{15k^{\text{hom}} + 10\mu^{\text{hom}}} \right) (\mu_1 - \mu^{\text{hom}})}, \quad (1.48)$$

where k_1 and μ_1 are the bulk modulus and the shear modulus of the inclusion respectively, k_2 and μ_2 are the bulk modulus and the shear modulus of the matrix respectively and f_1 is the volume fraction of the inclusion.

3.2.2 Mori-Tanaka method

The original method was proposed by [MOR 73] and [BEN 87] reformulated it in a simpler version to apply it to composites. The key assumption of this model gives a fourth order tensor to relate the average strain in the inclusion and the average strain in the matrix. The homogeneous boundary conditions on the displacement \mathbf{u} and the traction $\boldsymbol{\sigma}$ can be written as :

$$\mathbf{u} = \boldsymbol{\epsilon}^0 \mathbf{x} \quad \text{and} \quad \boldsymbol{\sigma} = \boldsymbol{\sigma}^0 \cdot \mathbf{n}, \quad (1.49)$$

where $\boldsymbol{\epsilon}^0$ and $\boldsymbol{\sigma}^0$ are constant strain and stress tensors and \mathbf{n} is the vector normal to the external surface of the composite. With these dual set of boundary conditions, one can have :

$$\bar{\boldsymbol{\epsilon}} = f_1 \langle \bar{\boldsymbol{\epsilon}}^{(1)} \rangle + f_2 \bar{\boldsymbol{\epsilon}}^{(2)} = \boldsymbol{\epsilon}^0 \quad (1.50)$$

and

$$\bar{\boldsymbol{\sigma}} = f_1 \langle \bar{\boldsymbol{\sigma}}^{(1)} \rangle + f_2 \bar{\boldsymbol{\sigma}}^{(2)} = \boldsymbol{\sigma}^0 \quad (1.51)$$

where $\langle \bar{\boldsymbol{\epsilon}}^{(1)} \rangle$ and $\langle \bar{\boldsymbol{\sigma}}^{(1)} \rangle$ are the overall average strain and stress tensors in an individual inclusion which are orientation dependent, while $\bar{\boldsymbol{\epsilon}}^{(2)}$ and $\bar{\boldsymbol{\sigma}}^{(2)}$ are those in the matrix and $\bar{\boldsymbol{\epsilon}}$, $\bar{\boldsymbol{\sigma}}$ are the overall average strain and stress tensors of the composite. With the idea of a concentration matrix, the effective stiffness tensor is defined as

$$\mathbb{C}^{\text{hom}} = \mathbb{C}^{(2)} + f_1 (\mathbb{C}^{(1)} - \mathbb{C}^{(2)}) \mathbb{B}_1, \quad (1.52)$$

where $\mathbb{C}^{(1)}$ and $\mathbb{C}^{(2)}$ are the stiffness tensors of different phases, ‘‘concentration factor’’ \mathbb{B}_1 is the orientation dependent tensor which is defined as

$$\bar{\boldsymbol{\epsilon}}^{(1)} = \mathbb{B}_1 \boldsymbol{\epsilon}^0. \quad (1.53)$$

From the dilute approximation, one can obtain $\mathbb{B}_1 \equiv \mathbb{Q}$, here \mathbb{Q} can be writtern in terms of Eshelby’s tensor \mathbb{P} as

$$\mathbb{Q} = \left[\mathbb{I} + \mathbb{P} \left[\mathbb{C}^{(2)} \right]^{-1} \left(\mathbb{C}^{(1)} - \mathbb{C}^{(2)} \right) \right]^{-1} \quad (1.54)$$

and \mathbb{I} is the identity tensor. This approximation is most valid at dilute concentrations thanks to the neglect of particle interactions for the dilute model. Assuming in this method

$$\bar{\boldsymbol{\epsilon}}^{(1)} \approx \mathbb{Q} \bar{\boldsymbol{\epsilon}}^{(2)}, \quad (1.55)$$

and combining EQ. 1.52, EQ. 1.53 and EQ. 1.55, here comes

$$\mathbb{C}^{\text{hom}} = \mathbb{C}^{(2)} + f_1 (\mathbb{C}^{(1)} - \mathbb{C}^{(2)}) \mathbb{Q} (f_2 \mathbb{I} + f_1 \mathbb{Q})^{-1}. \quad (1.56)$$

Finally, one can have

$$\frac{\bar{\epsilon}_{kk}^{(1)}}{\epsilon_{kk}^0} = (3k_2 + 4\mu_2)/(3k_1 + 4\mu_2) \quad (1.57)$$

and the effective bulk modulus

$$k^{\text{hom}} = k_2 + f_1(k_1 - k_2) \frac{k_2}{f_2(k_1 - k_2)\alpha_2 + k_2} \quad (1.58)$$

with

$$\alpha_2 = \frac{3k_2}{3k_2 + 4\mu_2}. \quad (1.59)$$

4 Usual computational homogenization approach based on the finite element method

Over the years, computational homogenization approaches have been presented in many works [MOU 98, FRI 12, KAN 03, HAI 08, ZOH 04, KAR 07, ODE 97, GEE 16, DIR 12]. A model based on a multilevel finite element (FE²) technique has been developed for heterogeneous material [FEY 00]. [CAI 03] has proved that the finite element method (FEM) is a very efficient technique to solve the microstructural mechanics problems. In this section, the usually used FEM-based computational homogenization approach with the periodic boundary condition (presented in Section 2.3) is introduced. The numerical results calculated by this approach will be compared with those by the proposed approach in Section 4.2 of Chapter 2.

In elastic domain, the constitutive equation could be established as EQ. 1.7 :

$$\begin{pmatrix} \bar{\sigma}_{11} \\ \bar{\sigma}_{22} \\ \bar{\sigma}_{33} \\ \sqrt{2}\bar{\sigma}_{23} \\ \sqrt{2}\bar{\sigma}_{13} \\ \sqrt{2}\bar{\sigma}_{12} \end{pmatrix} = \begin{bmatrix} C_{11}^{\text{hom}} & C_{12}^{\text{hom}} & C_{13}^{\text{hom}} & \sqrt{2}C_{14}^{\text{hom}} & \sqrt{2}C_{15}^{\text{hom}} & \sqrt{2}C_{16}^{\text{hom}} \\ & C_{22}^{\text{hom}} & C_{23}^{\text{hom}} & \sqrt{2}C_{24}^{\text{hom}} & \sqrt{2}C_{25}^{\text{hom}} & \sqrt{2}C_{26}^{\text{hom}} \\ & & C_{33}^{\text{hom}} & \sqrt{2}C_{34}^{\text{hom}} & \sqrt{2}C_{35}^{\text{hom}} & \sqrt{2}C_{36}^{\text{hom}} \\ & \text{Sym} & & 2C_{44}^{\text{hom}} & 2C_{45}^{\text{hom}} & 2C_{46}^{\text{hom}} \\ & & & & 2C_{55}^{\text{hom}} & 2C_{56}^{\text{hom}} \\ & & & & & 2C_{66}^{\text{hom}} \end{bmatrix} \begin{pmatrix} \bar{\epsilon}_{11} \\ \bar{\epsilon}_{22} \\ \bar{\epsilon}_{33} \\ \sqrt{2}\bar{\epsilon}_{23} \\ \sqrt{2}\bar{\epsilon}_{13} \\ \sqrt{2}\bar{\epsilon}_{12} \end{pmatrix}. \quad (1.60)$$

The approach consists in :

- impose 6 different macro-strains $\{\bar{\epsilon}_{ij}\}$;
- compute the average stress $\{\bar{\sigma}_{ij}\}$ and derive the components of the effective stiffness matrix $[C^{\text{hom}}]$.

From each calculation, one can obtain 6 components of the matrix. Given that there are 36 components in the matrix, 6 calculations are necessary. The detailed calculation procedures are listed in TAB. 1.1.

TABLE 1.1: The calculation procedures for the usual computational homogenization approach based on the FEM to obtain $[C^{hom}]$.

Calculation procedures	1	2	3	4	5	6
The imposed macro-strain $\{\bar{\epsilon}\}$	$\begin{Bmatrix} 1 \\ 0 \\ 0 \\ 0 \end{Bmatrix}$	$\begin{Bmatrix} 0 \\ 1 \\ 0 \\ 0 \end{Bmatrix}$	$\begin{Bmatrix} 0 \\ 0 \\ 1 \\ 0 \end{Bmatrix}$	$\begin{Bmatrix} 0 \\ 0 \\ 0 \\ \sqrt{2} \end{Bmatrix}$	$\begin{Bmatrix} 0 \\ 0 \\ 0 \\ \sqrt{2} \end{Bmatrix}$	$\begin{Bmatrix} 0 \\ 0 \\ 0 \\ \sqrt{2} \end{Bmatrix}$
The obtained average stress $\{\bar{\sigma}\}$				$\begin{Bmatrix} \bar{\sigma}_{11} \\ \bar{\sigma}_{22} \\ \bar{\sigma}_{33} \\ \sqrt{2}\bar{\sigma}_{12} \\ \sqrt{2}\bar{\sigma}_{23} \\ \sqrt{2}\bar{\sigma}_{13} \end{Bmatrix}$		
The corresponding obtained components of $[C^{hom}]$	$\begin{Bmatrix} C_{11}^{hom} \\ C_{21}^{hom} \\ C_{31}^{hom} \\ \sqrt{2}C_{41}^{hom} \\ \sqrt{2}C_{51}^{hom} \\ \sqrt{2}C_{61}^{hom} \end{Bmatrix}$	$\begin{Bmatrix} C_{12}^{hom} \\ C_{22}^{hom} \\ C_{32}^{hom} \\ \sqrt{2}C_{42}^{hom} \\ \sqrt{2}C_{52}^{hom} \\ \sqrt{2}C_{62}^{hom} \end{Bmatrix}$	$\begin{Bmatrix} C_{13}^{hom} \\ C_{23}^{hom} \\ C_{33}^{hom} \\ \sqrt{2}C_{43}^{hom} \\ \sqrt{2}C_{53}^{hom} \\ \sqrt{2}C_{63}^{hom} \end{Bmatrix}$	$\begin{Bmatrix} \sqrt{2}C_{14}^{hom} \\ \sqrt{2}C_{24}^{hom} \\ \sqrt{2}C_{34}^{hom} \\ 2C_{44}^{hom} \\ 2C_{54}^{hom} \\ 2C_{64}^{hom} \end{Bmatrix}$	$\begin{Bmatrix} \sqrt{2}C_{15}^{hom} \\ \sqrt{2}C_{25}^{hom} \\ \sqrt{2}C_{35}^{hom} \\ 2C_{45}^{hom} \\ 2C_{55}^{hom} \\ 2C_{65}^{hom} \end{Bmatrix}$	$\begin{Bmatrix} \sqrt{2}C_{16}^{hom} \\ \sqrt{2}C_{26}^{hom} \\ \sqrt{2}C_{36}^{hom} \\ 2C_{46}^{hom} \\ 2C_{56}^{hom} \\ 2C_{66}^{hom} \end{Bmatrix}$

Chapter 2

Effective elastic properties of regular Kelvin open-cell foams

*This chapter focuses on the influences of morphological parameters on the effective elastic properties of regular Kelvin open-cell foams. An innovative approach combined with Voronoi diagram is developed to generate foam structures. The morphological description allows to represent the details of the microstructure and to cover a wide range of open-cell foams which are usually used in engineering applications. In order to estimate the effective elastic properties, a micromechanical modeling based on Hill's lemma approach is proposed in this chapter. The effects of a number of morphological parameters on the elastic effective properties are studied. Considering the morphological parameters, generic analytical laws are deduced for Kelvin open-cell foams. The main results are published in the paper :
Zhu, W., Blal, N., Cunsolo, S., & Baillis, D. (2017).
Micromechanical modeling of effective elastic properties of open-cell foam. *International Journal of Solids and Structures*, 115, 61-72.*

Contents

1	Introduction	31
2	Modeling of open-cell structure	32
3	Computational periodic homogenization	35
3.1	Hill's lemma for periodic media [SUQ 87]	35
3.2	Finite element implementation of Hill's lemma approach (HL-FEM)	36
4	Numerical study	39
4.1	Mesh sensitivity	39
4.2	Validation by usual FEM	40
4.3	RVE sensitivity	42
5	Parametric study	43
5.1	Effect of Young's modulus of bulk	43
5.2	Effect of relative density	43
5.3	Effect of normalized curvature	44
5.4	Effect of diameter ratio	46
5.5	Effect of irregularity and dispersion of cell size distribution	49
6	Conclusion	53

1 Introduction

It is difficult to model and compute the mechanical properties of foams, since those of pores and matrix are different [DÜS 12]. Other heterogeneous materials also have the same problem. Because the dimensions of macroscopic structure and constituent vary greatly, it is difficult to evaluate such structures with considering all the details of constituent. The earliest homogenization theoretical principle has been raised in [HIL 63] and [HAS 62]. As discussed in the previous chapter, numerous numerical homogenization approaches have been published over the years, including the finite element method (FEM). [DÜS 12] pointed out that although FEM is versatile and widely used, it requires vast computational work. A suitable microstructure and corresponding boundary value problem have to be considered for each integration point of the finite elements in the macro-scale. As introduced in Section 4 in Chapter 1, in order to obtain the full effective stiffness tensor, usually 6 independent numerical calculations are necessary [YUA 08, STO 16]. By formulating a variational statement with an asymptotic expansion, a model, named the variational asymptotic method for unit cell homogenization (VAMUCH), has been raised by [YU 07a] for heterogeneous media which have periodic structures (see Appendix A). The finite element implementation of VAMUCH [YU 07a, YU 07b, TAN 08a, TAN 08b, ZHA 14] has the advantage that with only one calculation, the full effective stiffness tensor can be obtained without elementary loadings, comparing with the usual FEMs.

A number of approaches have been raised to generate foam structures. Tomographic technique is a very important method and has been widely used in many works [WAN 10, GAI 12, GAI 14, GAI 15]. By micrographies, [GON 05] studied the morphology of polyester urethane foams and proposed a symmetric function to describe the geometric characteristics. Using microtomography, [JAN 08] improved this approach and proved that different shapes of strut cross section, such as Plateau border, triangular and circular cross section, does affect the elastic properties of open-cell foam. The local morphological characteristics of struts, such as the cavity structure, the closed cell windows and the coatings, have been studied by generated models with a versatile dilation method based on implicit functions in [STO 13a]. Based on the 'voro++' code [RYC 09], 3D Voronoi structures have been generated to investigate the mechanical properties of both regular and irregular closed-cell polymer foams under uniaxial and multiaxial loadings in [BAR 14a] and [YE 15].

In previous works, microstructures of foam models are generally simplified. For example, for closed-cell models, the thickness of the walls are assumed as a constant value; Another example, for open-cell models, struts of foam models are considered as cylinders. In this chapter, a methodology is introduced which allows to generate realistic foam structures by considering the details of microstructure. It permits to generate representations of open-cell foam models by controlling a number of morphological parameters. Inspired by VAMUCH, Hill's lemma scheme is studied computationally to develop a micromechanical modeling to estimate the elastic effective properties. Unlike the usual FEMs which need 6 independent computations corresponding to 6 independent boun-

dary loadings, the main advantage of our proposed method is the ability to evaluate the effective properties with only one finite element computation and without any specific elementary loadings, such as macro-stains. It can make the calculation efficient and cheap. For regular Kelvin open-cell foams, the influences of the morphological parameters on the effective elastic properties are investigated. New generic analytical laws are deduced based on these estimations. The analytic laws have a satisfactory agreement with the numerical results, which makes them have a guiding role in designing and producing Kelvin open-cell foams. In addition, the influences of irregularity and cell size distribution of irregular cellular foams are also studied.

2 Modeling of open-cell structure

A new methodology is introduced in this section to generate realistic foam structures with a high control of the morphological parameters. This generation methodology, including the use of Voronoi diagram [RYC 09] and Surface Evolver post-processing [BRA 92], is inspired by [KRA 03, KRA 04] for pure morphology and [JAN 08] in study of mechanical properties. The methodology is realized by developing a Matlab code [MAT 16].

A certain amount of seeding points, corresponding to the cells of the final periodic structure, are created first. The regular Kelvin structure are generated with regular cubic centred distribution of seeding points. While for irregular structure, Random Sequential Absorption algorithm [KRA 03] is applied to make sure that equal-sized spheres are distributed in the given space without overlapping. The centers of these spheres are actually the seeding points. This algorithm ensure the minimum distance between any two seeding points, followed the polyhedral regions partitions of the space with respect to seeding points by Voronoi diagram [RYC 09]. In order to obtain more realistic structure, Surface Evolver [BRA 92] is used to make the structure energetically stable. The entire chain of the softwares (VORO++ \Rightarrow Surface Evolver) natively supports handling with periodic structures. The data imported into MATLAB is the “unwrapped” periodic structure. Every strut appears only once and their extreme points are not necessary to be aligned with the bounding box. To assure the cut is perfectly periodic, the structure is partially replicated, i.e. the parts of the structure that cross the bounding box are duplicated on all sides and then a cut is made (see FIG. 2.1).

This methodology can be summarized as the following steps :

- Generate a pseudo-random lattice of seeding points ;
- Generate a Voronoi diagram of these points ;
- Stabilize the resulting cell structure in the Surface Evolver [BRA 92] ;
- Add polygonal struts along the resulting skeleton.

In order to represent the microstructure of foams, four morphological parameters are

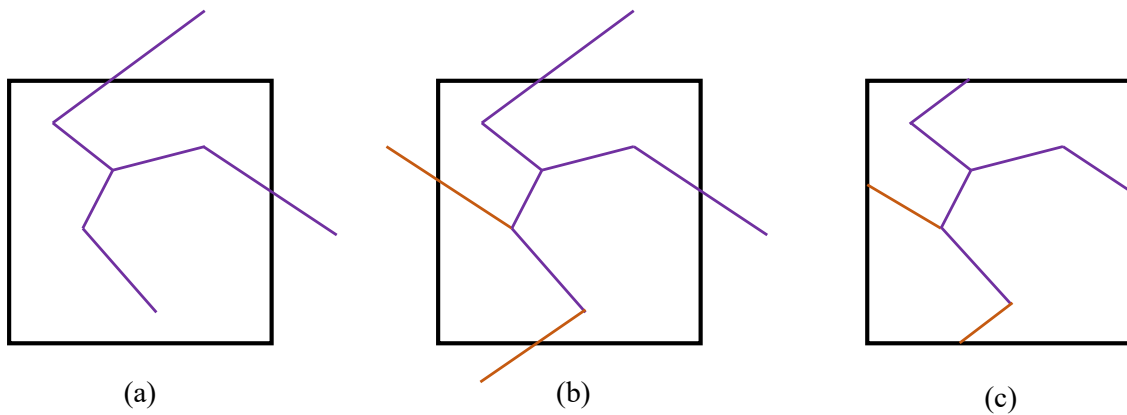


FIGURE 2.1: (a) Unwrapped periodic structure; (b) Structure with the duplicated parts on the sides; (c) Domain cut to periodic bounding box.

introduced. The first parameter C_V , named coefficient of variation, is defined to describe the dispersion of cell size distribution for irregular structures with $C_V = \sigma_{d_c} / \bar{d}_c$, where σ_{d_c} is the standard deviation of cell diameter and \bar{d}_c denotes average cell diameter (equivalent sphere). The dispersions of cell size distributions with different C_V s are shown in FIG. 2.2. For $C_V = 0$, the volume of each cell is same even if the structure is irregular.

Remark : In this thesis, the size distribution of cells is a Gaussian unimodal distribution by varying standard deviation.

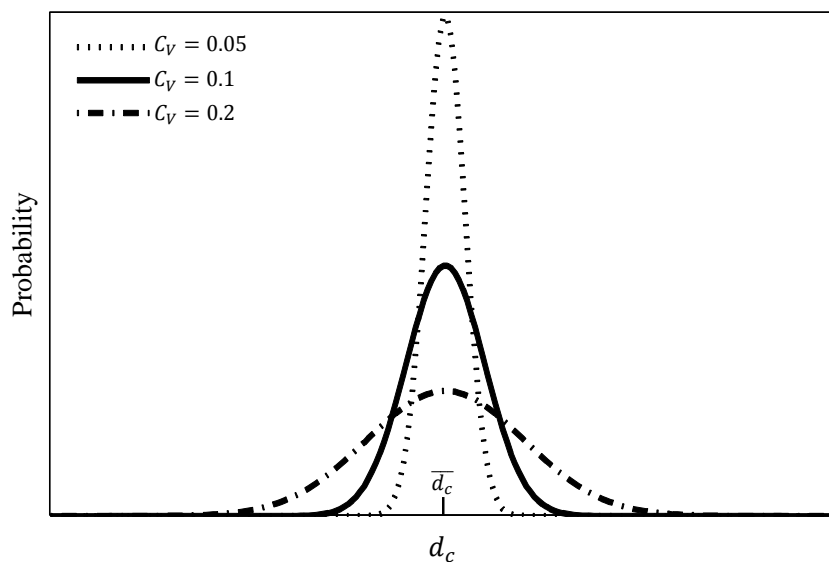


FIGURE 2.2: The dispersions of cell size distributions with different C_V s.

Polygonal struts are added along the generated skeleton taking into account the other morphological characters. The second morphological parameter is the relative density of foam, $\rho^{\text{hom}} / \rho^b$, which has been proved to have the largest effect on properties of foams. In

this thesis, the superscript notations ^{hom} and ^b represent the homogenization and the bulk, respectively. In this chapter, the relative densities of open-cell foam models are concentrated in the range [4% – 14%], corresponding to practical applications in engineering.

The cross section of the strut can be considered as an equilateral triangle whose sides are curved with certain curvature. The shape of the triangle is controlled by the third morphological parameter q , named normalized curvature, which equals to the curvature radius of the circumcircle of the triangle divided by the curvature radius of the sides. The shape of the cross section can change from concave triangle to flat triangle and to circle by varying q . The variation of the cross section shape is shown in FIG. 2.3.

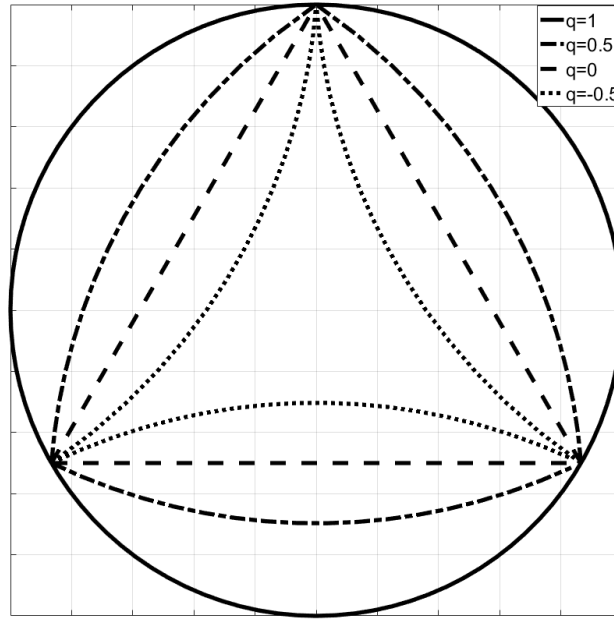


FIGURE 2.3: The variation of cross section of strut.

The fourth parameter shows the variation of the cross-sectional area along the strut axis of a random strut. At an axial position $\eta = \|\boldsymbol{x}\|/l$, the diameter of the circumcircle of the cross section $d(\eta)$, can be normalized by that at mid-span d_{min} , as the function :

$$d(\eta) = d_{min} \left[1 + \frac{(1-t)(2\eta-1)^2}{t} \right], \quad (2.1)$$

where \boldsymbol{x} is the local abscissa and l denotes the total length of the strut. The ratio of minimum to maximum diameter can be represented as $t = d_{min}/d_{max}$. Different longitudinal profiles of struts can be obtained by varying t , named diameter ratio (see FIG. 2.4).

Notes that the relative density and the cell sizes of the foam model can keep constant by changing the diameter of circumcircle of the cross section to accommodate the variations of q and t .

In this thesis, unless otherwise specified, the final structure is meshed with linear tetrahedron solid elements using the commercial package ICEM CFD 16.2 [ANS 13].

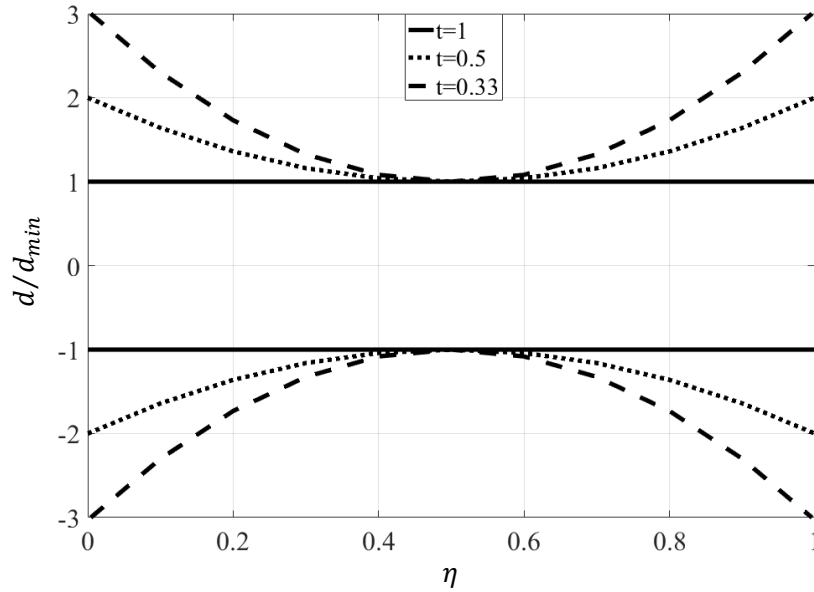


FIGURE 2.4: The variation of longitudinal profile of strut.

3 Computational periodic homogenization

3.1 Hill's lemma for periodic media [SUQ 87]

A RVE of an open-cell foam Ω , which is made of an elastic bulk medium and a porous phase, is considered. The effective elastic properties of the RVE are evaluated with a computational periodic homogenization approach. Assume quasi-static evolutions, neglected body forces and the linear elasticity framework for this approach. The local fields fluctuate at the local scale \boldsymbol{x} ($\boldsymbol{x} = x_i \boldsymbol{e}_i$, where \boldsymbol{e}_i is the component of the euclidean space) because of the heterogeneities. As said in Section 2.3, the local strain field $\boldsymbol{\epsilon}$, at \boldsymbol{x} within the RVE can be separated into two fields : a macroscopic field $\bar{\boldsymbol{\epsilon}}$ and a correction field $\boldsymbol{\epsilon}'$, such that

$$\boldsymbol{\epsilon}(\boldsymbol{x}) = \bar{\boldsymbol{\epsilon}} + \boldsymbol{\epsilon}'(\boldsymbol{x}). \quad (2.2)$$

The macroscopic strain corresponds to the average of the local strain field over the RVE, i.e. $\bar{\boldsymbol{\epsilon}} = \langle \boldsymbol{\epsilon} \rangle$, while the fluctuation strain $\boldsymbol{\epsilon}'$ represents the presence of heterogeneities and is derived from a local fluctuation displacement field \boldsymbol{u}' , i.e.

$$\boldsymbol{\epsilon}' = 1/2 (\nabla \boldsymbol{u}' + {}^T \nabla \boldsymbol{u}'). \quad (2.3)$$

The perturbation field \boldsymbol{u}' is a periodic field, which means its components are equal over two opposite sides of the RVE. It leads a vanishing average $\langle \boldsymbol{\epsilon}' \rangle = \mathbf{0}$. The local displacement \boldsymbol{u} can be written as

$$\boldsymbol{u}(\boldsymbol{x}) = \bar{\boldsymbol{\epsilon}} \cdot \boldsymbol{x} + \boldsymbol{u}'(\boldsymbol{x}) \quad \text{in } \Omega, \quad \boldsymbol{u}' \text{ periodic.} \quad (2.4)$$

Only considering the linear elasticity case, the local constitutive law is

$$\boldsymbol{\sigma}(\mathbf{x}) = \mathbb{C}(\mathbf{x}) : \boldsymbol{\epsilon}(\mathbf{x}), \quad (2.5)$$

where $\boldsymbol{\sigma}(\mathbf{x})$ means the local stress tensor, $\mathbb{C}(\mathbf{x})$ denotes the local stiffness fourth order tensor and the double dot " : " is double tensorial contraction product. Over the RVE, the equilibrium conditions is such that :

$$\text{div}(\boldsymbol{\sigma}) = \mathbf{0} \text{ in } \Omega, \quad \boldsymbol{\sigma} \cdot \mathbf{n} \text{ anti-periodic.} \quad (2.6)$$

The anti-periodicity denotes that the tensor vector $\boldsymbol{\sigma} \cdot \mathbf{n}$ has opposite values at opposite sides of the RVE. Then the macroscopic stress tensor is defined as the average of the local strain field over the RVE, i.e. $\bar{\boldsymbol{\sigma}} = \langle \boldsymbol{\sigma} \rangle$. Introduce two admissibility sets

$$\mathcal{K}_{\#} = \{ \mathbf{v}, \mathbf{v} = \bar{\boldsymbol{\epsilon}} \cdot \mathbf{x} + \mathbf{v}', \quad \mathbf{v}' \text{ periodic} \} \quad (2.7)$$

and

$$\mathcal{S}_{\#} = \{ \boldsymbol{\tau}, \text{div}(\boldsymbol{\tau}) = \mathbf{0} \text{ in } \Omega, \quad \bar{\boldsymbol{\tau}} = \langle \boldsymbol{\tau} \rangle \text{ and } \boldsymbol{\tau} \cdot \mathbf{n} \text{ anti-periodic} \}. \quad (2.8)$$

According to the Hill's lemma for periodic media [SUQ 87], for any local strain and stress fields included in the periodic admissibility sets $\mathcal{K}_{\#}$ and $\mathcal{S}_{\#}$ respectively, the average of the local internal work equals to the global work, i.e.

$$\langle \boldsymbol{\tau} : \boldsymbol{\epsilon} \rangle = \bar{\boldsymbol{\tau}} : \bar{\boldsymbol{\epsilon}}, \quad \text{for } (\mathbf{v}, \boldsymbol{\tau}) \in \mathcal{K}_{\#} \times \mathcal{S}_{\#} \quad \text{with} \quad \boldsymbol{\epsilon} = \frac{1}{2} (\nabla \mathbf{v} + {}^T \nabla \mathbf{v}). \quad (2.9)$$

3.2 Finite element implementation of Hill's lemma approach (HL-FEM)

Suppose that $\mathbf{v} \in \mathcal{K}_{\#}$ is a virtual displacement field and $\boldsymbol{\sigma}$ is a local stress field associated to the displacement \mathbf{u} solution of the equilibrium state over the RVE, i.e. $\boldsymbol{\sigma} = \mathbb{C} : \boldsymbol{\epsilon}$ with $\boldsymbol{\epsilon} = \bar{\boldsymbol{\epsilon}} + \boldsymbol{\epsilon}'$. Since the fields \mathbf{v} and $\boldsymbol{\sigma}$ belong to the admissibility sets $\mathcal{K}_{\#}$ and $\mathcal{S}_{\#}$ respectively, the Hill's lemma works. Furthermore, it can be applied in two virtual fields. On the one hand, if one considers a virtual fluctuation periodic fields \mathbf{v}^* , it comes $\mathbf{v} = \bar{\boldsymbol{\epsilon}} \cdot \mathbf{x} + \mathbf{v}^*$ and the Hill's lemma yields to

$$\langle \boldsymbol{\epsilon}' : \mathbb{C} : \boldsymbol{\epsilon}(\mathbf{v}^*) \rangle + \langle \bar{\boldsymbol{\epsilon}} : \mathbb{C} : \boldsymbol{\epsilon}(\mathbf{v}^*) \rangle = 0 \quad \forall \mathbf{v}^* \text{ periodic.} \quad (2.10)$$

On the other hand, if one considers a virtual macroscopic strain field $\bar{\boldsymbol{\epsilon}}^*$ which makes $\mathbf{v} = \bar{\boldsymbol{\epsilon}}^* \cdot \mathbf{x} + \mathbf{u}'$, then the Hill's lemma gives

$$\langle \boldsymbol{\epsilon}' : \mathbb{C} : \bar{\boldsymbol{\epsilon}}^* \rangle + \bar{\boldsymbol{\epsilon}} : \langle \mathbb{C} \rangle : \bar{\boldsymbol{\epsilon}}^* = \bar{\boldsymbol{\sigma}} : \bar{\boldsymbol{\epsilon}}^* \quad \forall \bar{\boldsymbol{\epsilon}}^*. \quad (2.11)$$

Using the modified Voigt notation, \mathbb{C} , $\boldsymbol{\epsilon}$ and $\boldsymbol{\sigma}$ could be simplified to matrix $[\mathbb{C}]$, vector $\{\boldsymbol{\epsilon}\}$ and $\{\boldsymbol{\sigma}\}$, respectively. The elementary fluctuation strain vector can be related to the periodic displacement for a finite element discretization of the RVE as :

$$\{\boldsymbol{\epsilon}'\} = [\mathbf{B}]\{\mathbf{u}'\}, \quad (2.12)$$

where $[\mathbf{B}]$ is the matrix which relates strains and displacements and $\{\mathbf{u}'\}$ is the periodic elementary displacement vector. In the discretized formulation, EQ. 2.10 and EQ. 2.11 can be written as

$$\begin{cases} [\mathbf{K}]\{\mathbf{u}'\} + [\mathbf{F}]\{\bar{\boldsymbol{\epsilon}}\} = \{\mathbf{0}\} \\ {}^T[\mathbf{F}]\{\mathbf{u}'\} + [\bar{\mathbf{C}}]\{\bar{\boldsymbol{\epsilon}}\} = \{\bar{\boldsymbol{\sigma}}\} \end{cases}, \quad (2.13)$$

with

$$\begin{cases} [\bar{\mathbf{C}}] = \frac{1}{V} \int_{\Omega} [\mathbf{C}^b] d\mathbf{x} & (6 \times 6 \text{ matrix}) \\ [\mathbf{F}] = \frac{1}{V} \int_{\Omega} [\mathbf{B}]^T [\mathbf{C}^b] d\mathbf{x} & (N \times 6 \text{ matrix}) \\ [\mathbf{K}] = \frac{1}{V} \int_{\Omega} [\mathbf{B}]^T [\mathbf{C}^b] [\mathbf{B}] d\mathbf{x} & (N \times N \text{ matrix}) \end{cases}, \quad (2.14)$$

where N denotes the degrees of freedom of the RVE and $[\mathbf{C}^b]$ is the elastic stiffness matrix of the bulk. In our case, the periodic boundary condition can be written as follows if the RVE is imagined as a cube whose side length equals to 1 :

$$\mathbf{u}' \left(x_1 = -\frac{1}{2}, x_2, x_3 \right) = \mathbf{u}' \left(x_1 = +\frac{1}{2}, x_2, x_3 \right), \quad (2.15)$$

$$\mathbf{u}' \left(x_1, x_2 = -\frac{1}{2}, x_3 \right) = \mathbf{u}' \left(x_1, x_2 = +\frac{1}{2}, x_3 \right), \quad (2.16)$$

$$\mathbf{u}' \left(x_1, x_2, x_3 = -\frac{1}{2} \right) = \mathbf{u}' \left(x_1, x_2, x_3 = +\frac{1}{2} \right), \quad (2.17)$$

where the origin of the local coordinate is the center of RVE. FIG. 2.5 illustrates two sets of corresponding nodes ($A^+ - A^-$ and $B^+ - B^-$) on the boundary surfaces in a 2D perspective for clarity. Slave the nodes on the positive boundary surfaces (i.e., $x_i = +\frac{1}{2}, i = 1, 2, 3$) to the corresponding nodes on the opposite negative boundary surfaces (i.e., $x_i = -\frac{1}{2}$) and generate two selection matrices, $[\mathbf{S}_c]$ and $[\mathbf{S}_s]$, to assemble all the independent active degrees of freedom of these two node categories, respectively. The periodic displacement fields of arbitrary two corresponding nodes are the same according to EQ. 2.15-EQ. 2.17, which makes the periodic boundary condition for the discrete formulation have the form :

$$[\mathbf{S}]\{\mathbf{u}'\} = \{\mathbf{0}\}, \quad \text{with} \quad [\mathbf{S}] = [\mathbf{S}_c] - [\mathbf{S}_s]. \quad (2.18)$$

In [YU 07a, TAN 08a], the computational homogenization method is proposed with no need to impose boundary loadings. The idea of the approach is computing an explicit

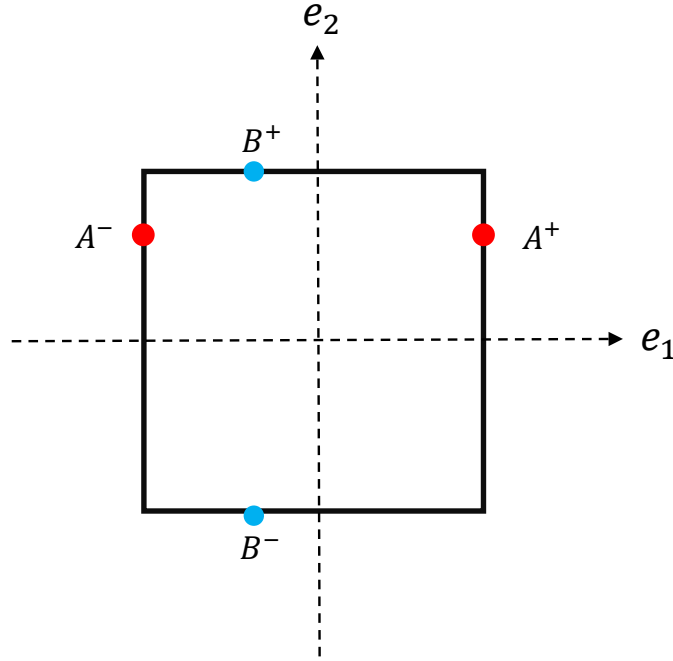


FIGURE 2.5: Illustration of the corresponding nodes on the boundary surfaces.

expression of the effective stiffness without the post-processing of the averaged fields, which is always necessary with elementary loadings for the usual method (e.g. [STO 16]). Indeed, the first equation of the discretized Hill's lemma, i.e. EQ. 2.13₍₁₎ results in the constrained linear problem :

$$[\mathbf{K}]\{\mathbf{u}'\} = -[\mathbf{F}]\{\bar{\boldsymbol{\epsilon}}\} \quad \text{under the constraint} \quad [\mathbf{S}]\{\mathbf{u}'\} = \{\mathbf{0}\}. \quad (2.19)$$

By Lagrange Multiplier method, one can obtain :

$$\begin{bmatrix} \mathbf{K} & {}^T\mathbf{S} \\ \mathbf{S} & \mathbf{0} \end{bmatrix} \begin{Bmatrix} \mathbf{u}' \\ \boldsymbol{\lambda} \end{Bmatrix} = - \begin{bmatrix} \mathbf{F} \\ \mathbf{0} \end{bmatrix} \{\bar{\boldsymbol{\epsilon}}\}, \quad (2.20)$$

where $\{\boldsymbol{\lambda}\}$ is the Lagrange multiplier. Obviously, the fluctuation displacement field $\{\mathbf{u}'\}$ linearly depends on $\{\bar{\boldsymbol{\epsilon}}\}$:

$$\{\mathbf{u}'\} = [\mathbf{A}]\{\bar{\boldsymbol{\epsilon}}\}, \quad (2.21)$$

where $[\mathbf{A}]$ ($N \times 6$ matrix) is a macroscopic strain-to-fluctuation displacement operator. Similarly to the VAMUCH method [TAN 08a], $\{\bar{\boldsymbol{\epsilon}}\}$ can be considered as a variable symbol and one only needs to compute the localization-like operator $[\mathbf{A}]$ rather than imposing 6 independent elementary loadings $\{\bar{\boldsymbol{\epsilon}}\}$ and solving the associated finite element boundary volume problems (run 6 FE computations). It should be noticed that the operator $[\mathbf{A}]$ is not the localization tensor \mathbb{A} , which usually links the local and global strains in homogenization, i.e. $\boldsymbol{\epsilon} = \mathbb{A} : \bar{\boldsymbol{\epsilon}}$ [MIC 99].

Substituting EQ. 2.21 into EQ. 2.13₍₂₎, one can obtain

$$\{\bar{\sigma}\} = ([\bar{C}] + {}^T [F][A]) \{\bar{\epsilon}\} = [C^{\text{hom}}] \{\bar{\epsilon}\}. \quad (2.22)$$

Obviously $[C^{\text{hom}}]$ is the required effective stiffness matrix instead of specific $\{u'\}$. The same result can be obtained using the framework of the VAMUCH method (shown in Appendix A). EQ. 2.22 also exhibits that the effective stiffness tensor is a correction of the Voigt bound $\langle [C] \rangle = [\bar{C}]$ with the induced fluctuation contribution ${}^T [F][A]$. The effective stiffness $[C^{\text{hom}}]$ can be explicitly obtained with only one finite element computation.

Remark :

- As mentioned, this approach is based on the discrete formula of the Hill's lemma raised in [MOU 98], where a stress prescribed approach is considered that the fluctuation field can be obtained by solving EQ. 2.13 and the effective properties can be derived then if one imposes the overall stress. While for our proposed approach, the system (EQ. 2.13) is proposed to solve directly and $[C^{\text{hom}}]$ can be computed directly without calculating the local fields.
- If necessary, the local fields can be obtained with the macroscopic fields and the localization operator $[A]$, e.g. $\epsilon(x) = \bar{\epsilon} + \epsilon'(x) \Rightarrow \{\epsilon\} = \{\bar{\epsilon}\} + [A]\{\bar{\epsilon}\}$.
- HL-FEM can be considered as the VAMUCH method with different formulations of homogenization equations.
- The approach is only applied to small deformation theory now.

4 Numerical study

A reference model (see FIG. 2.6) is generated with morphological parameters ($\rho^{\text{hom}}/\rho^{\text{b}} = 6\%$, $q = 1$, $t = 1$, *Kelvin*) and bulk properties (Young's modulus of bulk $E^{\text{b}} = 70$ GPa and Poisson's ratio of bulk $\nu^{\text{b}} = 0.3$) corresponding to the metallic bulk. The influences of a number of parameters are investigated by comparing with the reference model in the following sections.

4.1 Mesh sensitivity

Meshing is always a key point for finite element analyse. The result is more accurate when the mesh size is smaller (the number of elements is more). If the number of elements is infinitely many, the result is supposed to be infinitely close to the real value. With this conception, a linear relation between the number of elements and the effective property is raised to estimate the convergence using the empirical criterion [ROB 00, GAT 05] :

$$C_{ij}^{\text{hom}} = C_{ij}^0 + \frac{aa}{N_e}, \quad (2.23)$$

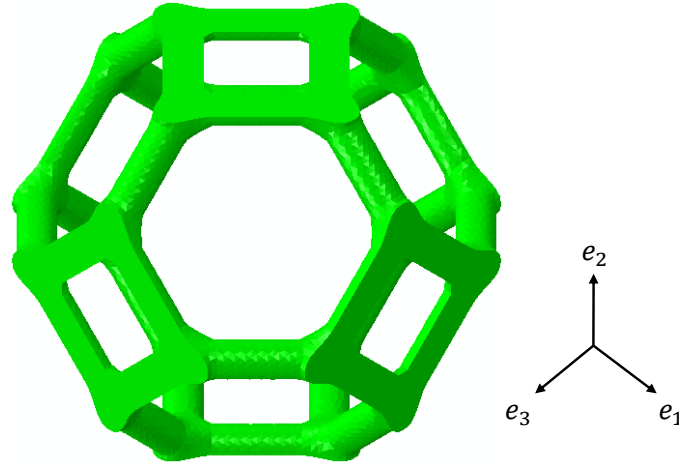


FIGURE 2.6: The reference model ($\rho^{\text{hom}}/\rho^{\text{b}} = 6\%$, $q = 1$, $t = 1$, *Kelvin*).

where C_{ij}^{hom} is a component of the effective elastic stiffness matrix, C_{ij}^0 stands for its convergence value, aa means a constant and N_e denotes the number of elements.

When the reference model is meshed with 245,006 linear solid elements, the obtained effective elastic stiffness matrix in the cubic frame (e_1, e_2, e_3) is :

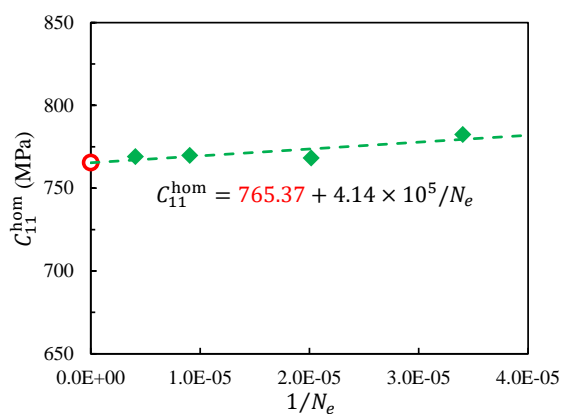
$$[C^{\text{hom}}] = \begin{bmatrix} 769.07 & 554.98 & 555.08 & \sim 0 & \sim 0 & \sim 0 \\ & 768.74 & 554.94 & \sim 0 & \sim 0 & \sim 0 \\ & & 768.69 & \sim 0 & \sim 0 & \sim 0 \\ & \text{Sym} & & 161.99 & \sim 0 & \sim 0 \\ & & & & 161.93 & \sim 0 \\ & & & & & 161.91 \end{bmatrix} \text{ (MPa)}.$$

One can see that there are only three independent components in the matrix, which proves Kelvin foam models are cubic symmetrical. C_{11}^{hom} , C_{12}^{hom} and C_{44}^{hom} are necessary to obtain the effective elastic properties of Kelvin foam models. For clarity, the relations between C_{ij}^{hom} and the number of elements are plotted in FIG. 2.7 as example. The green points are the computational results with different numbers of elements and the dashed fitting line is plotted based on EQ. 2.23 with the computational results. The intersection point of the fitting line and Y axis, i.e. the red point in the figure, denotes the convergence result. This method is used throughout the entire thesis to reduce the mesh discretization error.

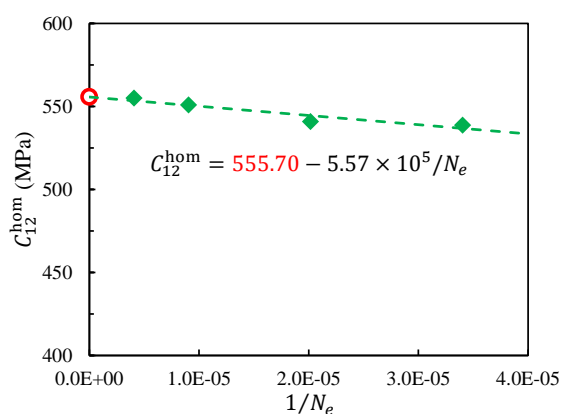
4.2 Validation by usual FEM

With the commercial FE package Abaqus 6.11-2 [Aba 11], the usual FEM is performed to validate the proposed HL-FEM. The periodic boundary condition [YAN 99] is also imposed on the reference model in Abaqus to make sure the continuity.

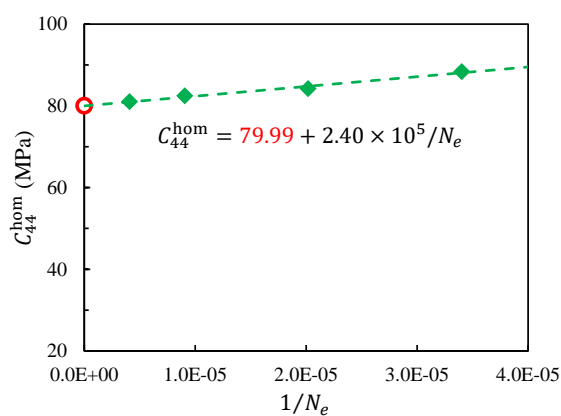
Bulk properties are set as same as in Section 4.1. One can see in TAB. 2.1 that the



(a)



(b)



(c)

FIGURE 2.7: The relation between C_{ij}^{hom} and the number of elements for the reference model ($\rho^{hom}/\rho^b = 6\%$, $q = 1$, $t = 1$, *Kelvin*).

numerical results obtained by two approaches are exactly the same, which makes HL-FEM validated.

TABLE 2.1: The comparison of the effective properties obtained by HL-FEM and Abaqus.

Approach	C_{11}^{hom} (MPa)	C_{12}^{hom} (MPa)	C_{44}^{hom} (MPa)
HL-FEM	765.37	555.70	79.99
Abaqus	765.37	555.70	79.99

4.3 RVE sensitivity

In order to study RVE sensitivity, two models with the same morphological parameters as the reference model are generated, which contains different numbers of cells. The first model actually is the reference model, named Model 1[#] with two cells. The second model contains sixteen cells, named Model 2[#]. FIG. 2.8 shows the structures of these two models. It should be explained clearly that, there are eight neighbour cells at the eight corners of the cubic unit cell in Model 1[#], which share struts with the center cell. Hence there are two Kelvin cells in Model 1[#]. Similarly, Model 2[#] contains sixteen cells in total. Bulk properties are set as same as mentioned in Section 4.1. TAB. 2.2 demonstrates the effective elastic properties of two models. One can see that the differences between the properties of two models are negligible, which proves that the number of cells has no obvious influence on the effective elastic properties for Kelvin open-cell models under the periodic boundary condition. For our study, small RVE like the reference model is enough. Hence the following investigations will be mainly performed on the small RVE.

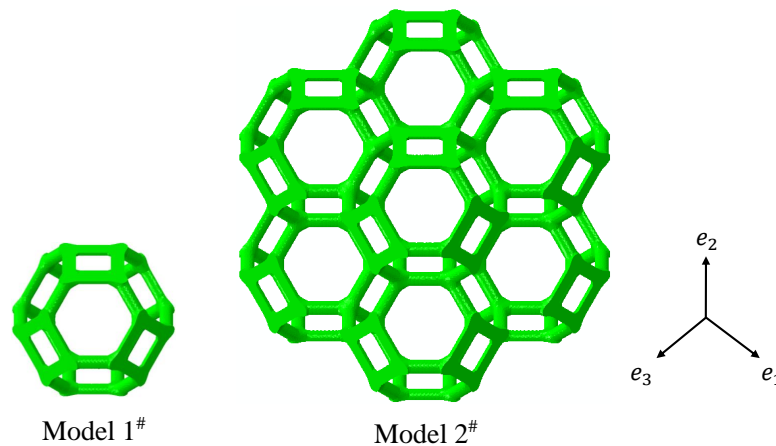


FIGURE 2.8: Illustration of Model 1[#] and Model 2[#].

TABLE 2.2: The comparison of the effective properties between Model 1[#] and Model 2[#].

Model	C_{11}^{hom} (MPa)	C_{12}^{hom} (MPa)	C_{44}^{hom} (MPa)
Model 1 [#]	765.37	555.70	79.99
Model 2 [#]	764.85	552.16	80.32

5 Parametric study

By varying E^b , ρ^{hom}/ρ^b , t , q and C_V , the influences of these five parameters are investigated in this section. The numerical computations are performed with the assumption that $\nu^b = 0.3$.

5.1 Effect of Young's modulus of bulk

For the reference model, the normalized properties $C_{11}^{\text{hom}}/C_{11}^b$, $C_{12}^{\text{hom}}/C_{12}^b$ and $C_{44}^{\text{hom}}/C_{44}^b$ are verified to be constant and independent of the variation of E^b from 40 GPa to 100 GPa. Therefore, E^b defaults to 70 GPa in the following investigations, which corresponds to aluminum bulk.

5.2 Effect of relative density

In [GIB 97, ZHU 00, STO 15, ROB 01, BAR 14a, KÖL 16] etc, numerous analytical formulas among varieties of mechanical properties and relative density have been raised. FIG. 2.9 shows the comparison between our numerical results and the data of [STO 15] for Kelvin open-cell models. The models used have the morphological parameters ($q = 1, t = 1, \text{Kelvin}$) and six different relative densities ($\rho^{\text{hom}}/\rho^b = \{4\%; 6\%; 8\%; 10\%; 12\%; 14\%\}$). Effective Young's modulus (E^{hom}), effective shear modulus (μ^{hom}) and effective Poisson's ratio (ν^{hom}) are compared and they are calculated from the effective elastic stiffness matrix with the following equations for Kelvin foam models :

$$E^{\text{hom}} = \frac{(C_{11}^{\text{hom}} - C_{12}^{\text{hom}})(C_{11}^{\text{hom}} + 2C_{12}^{\text{hom}})}{C_{11}^{\text{hom}} + C_{12}^{\text{hom}}}, \quad (2.24)$$

$$\mu^{\text{hom}} = C_{44}^{\text{hom}}, \quad (2.25)$$

$$\nu^{\text{hom}} = \frac{C_{12}^{\text{hom}}}{C_{11}^{\text{hom}} + C_{12}^{\text{hom}}}. \quad (2.26)$$

In the figure, the deviation between our results and Storm's is less than 3% for effective Poisson's ratio, while the deviations are between 8% and 25% for effective Young's modulus and effective shear modulus. It may be caused by the difference in the microstructure of Kelvin open-cell models.

The evolutions of the normalized effective elastic properties $C_{11}^{\text{hom}}/C_{11}^{\text{b}}$, $C_{12}^{\text{hom}}/C_{12}^{\text{b}}$ and $C_{44}^{\text{hom}}/C_{44}^{\text{b}}$ with the relative density are shown in FIG. 2.10. One can see that the variations of these three normalized properties caused by relative density are obvious but different for the low density foams. Clearly, $C_{12}^{\text{hom}}/C_{12}^{\text{b}}$ increase linearly while $C_{11}^{\text{hom}}/C_{11}^{\text{b}}$ and $C_{44}^{\text{hom}}/C_{44}^{\text{b}}$ have quadratic increase with the increase of relative density.

We propose the following equations with four coefficients ($\phi_1; \phi_2; \phi_3; \phi_4$) to point out the relations between each effective elastic property and the relative density :

$$\frac{C_{11}^{\text{hom}}}{C_{11}^{\text{b}}} = \phi_1 \left(\frac{\rho^{\text{hom}}}{\rho^{\text{b}}} \right)^2 + \phi_2 \left(\frac{\rho^{\text{hom}}}{\rho^{\text{b}}} \right), \quad (2.27)$$

$$\frac{C_{12}^{\text{hom}}}{C_{12}^{\text{b}}} = \phi_3 \left(\frac{\rho^{\text{hom}}}{\rho^{\text{b}}} \right), \quad (2.28)$$

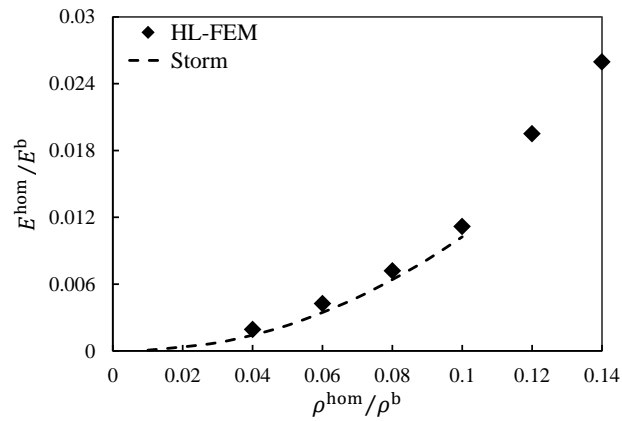
$$\frac{C_{44}^{\text{hom}}}{C_{44}^{\text{b}}} = \phi_4 \left(\frac{\rho^{\text{hom}}}{\rho^{\text{b}}} \right)^2. \quad (2.29)$$

5.3 Effect of normalized curvature

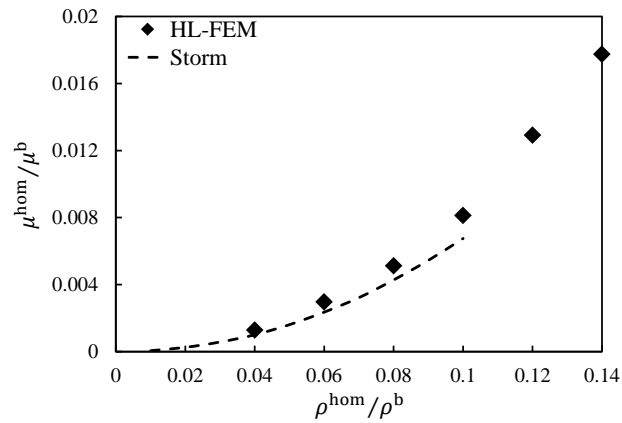
The effect of normalized curvature is investigated with the variation of q in the range $[-0.3, 1]$. The study is performed on the models ($\rho^{\text{hom}}/\rho^{\text{b}} = 6\%, t = 1, \text{Kelvin}$). Introduce the deviation indicator, $e_{ij} = \frac{C_{ij}^{\text{hom}} - C_{ij}^{*0}}{C_{ij}^{*0}}$, in order to present clearly the effect of normalized curvature on three effective properties. Here C_{ij}^{*0} denotes the corresponding property of the reference model ($\rho^{\text{hom}}/\rho^{\text{b}} = 6\%, q = 1, t = 1, \text{Kelvin}$). It is clear in FIG. 2.11 that the variation of e_{12} is very small, which means the normalized curvature has the negligible effect on C_{12}^{hom} in the whole range. The effect of the normalized curvature on e_{11} and e_{44} , especially on e_{44} , is significant in the range $[-0.3, 0.25]$, while it is much smaller in the range $(0.25, 1]$.

By fitting with the computational results, four linear functions $\phi_1(q)$, $\phi_2(q)$, $\phi_3(q)$ and $\phi_4(q)$ are obtained for Kelvin open-cell foams with constant diameter struts :

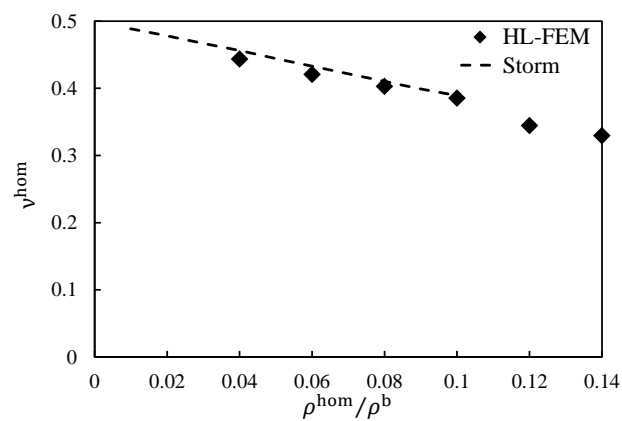
$$\left\{ \begin{array}{l} \phi_1 = -0.135q + 1.009 \\ \phi_2 = -0.0122q + 0.091 \\ \phi_3 = 0.0116q + 0.222 \\ \phi_4 = -0.179q + 1.045 \end{array} \right. \quad (2.30)$$



(a)



(b)



(c)

FIGURE 2.9: Evolution of (a) effective Young's modulus, (b) effective shear modulus and (c) effective Poisson's ratio with respect to the relative density.

The evolutions of the normalized effective elastic properties with the relative density

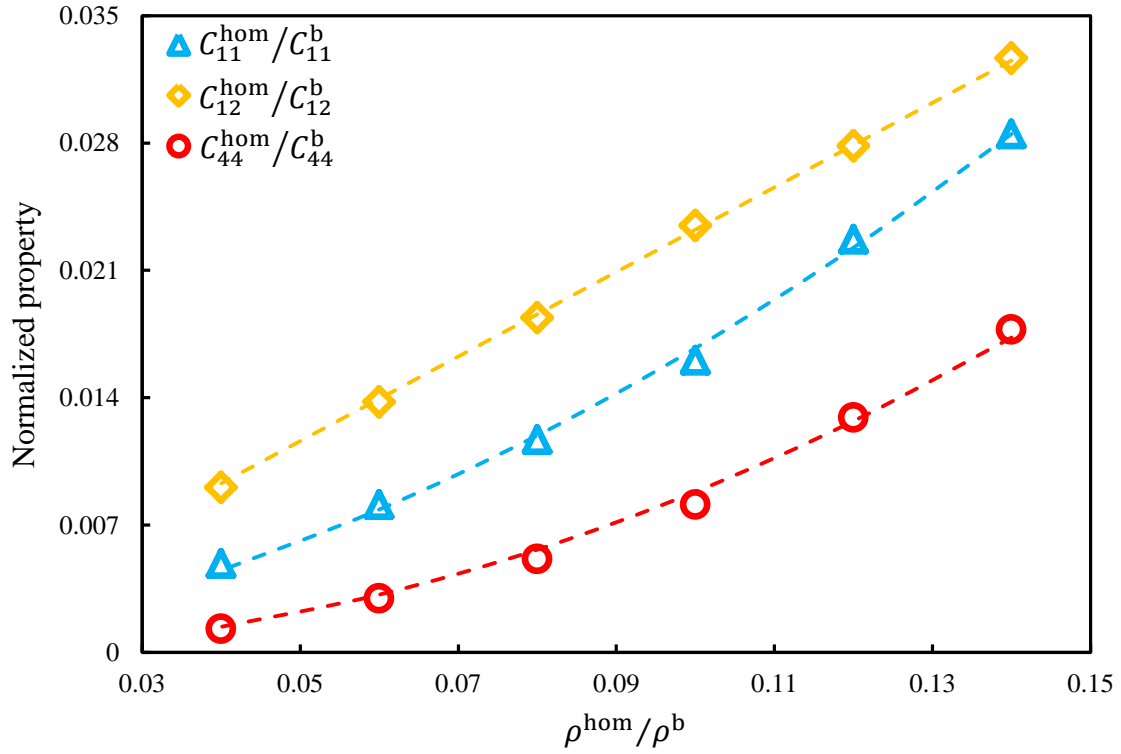


FIGURE 2.10: Effect of the relative density for the models ($q = 1, t = 1, Kelvin$) on the normalized properties.

of the analytical laws (al) (EQ. 2.27-EQ. 2.29 and EQ. 2.30) and the computational results (cr) are plotted in FIG. 2.12. Three sets of data with ($q = \{-0.3; 0.5; 1\}$) are given in the figures for clarity. The mean relative errors of $C_{11}^{\text{hom}} / C_{11}^{\text{b}}$, $C_{12}^{\text{hom}} / C_{12}^{\text{b}}$ and $C_{44}^{\text{hom}} / C_{44}^{\text{b}}$ are 2.06%, 1.95% and 6.08% respectively for all data.

Remark : Here, relative error means its absolute value.

5.4 Effect of diameter ratio

10 values in the range $[0.33, 1]$ are considered as the diameter ratios, which permit to cover the common ones. The study is carried out on the models ($\rho^{\text{hom}} / \rho^{\text{b}} = 6\%, q = 1, Kelvin$). The whole range of diameter ratio can be separated into two parts by dashed lines shown in FIG. 2.13. In part ①, the diameter ratio changes from 0.33 to 0.7, which stands for the struts with the large difference between the maximum and minimum diameter. The struts are flatter in part ② when the diameter ratio varies in the range ($t \in (0.7, 1]$). All three effective elastic properties have significant increase with the increase of diameter ratio in part ①, while the variations of them are much smaller in part ②.

Similarly, four functions $\phi_1(t)$, $\phi_2(t)$, $\phi_3(t)$ and $\phi_4(t)$ are obtained for Kelvin open-

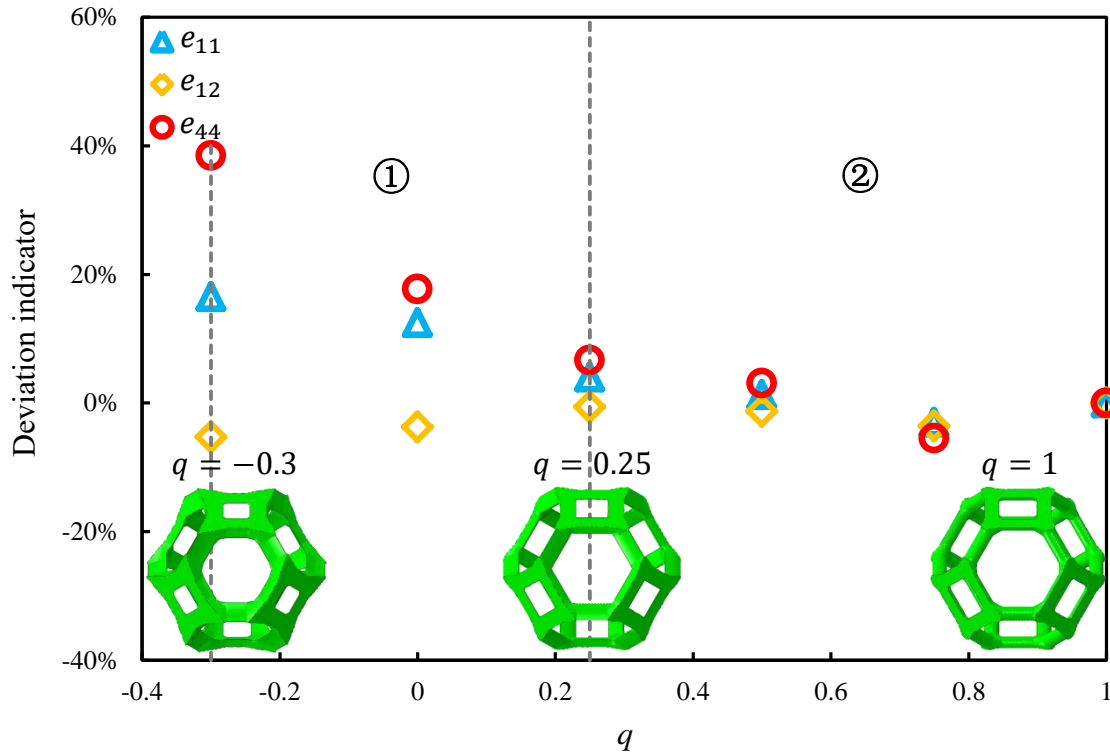


FIGURE 2.11: Effect of the normalized curvature for the models ($\rho^{\text{hom}}/\rho^{\text{b}} = 6\%$, $t = 1$, *Kelvin*) on the deviation indicators.

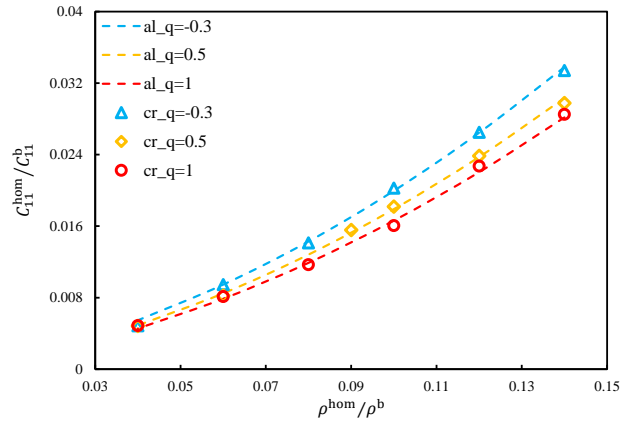
cell foams with circular cross section struts by fitting :

$$\begin{cases} \phi_1 = 7.147t^3 - 16.885t^2 + 12.895t - 2.334 \\ \phi_2 = 0.0114t + 0.0765 \\ \phi_3 = -0.291t^2 + 0.518t + 0.00234 \\ \phi_4 = 2.866t^3 - 7.496t^2 + 6.411t - 0.897 \end{cases} \quad (2.31)$$

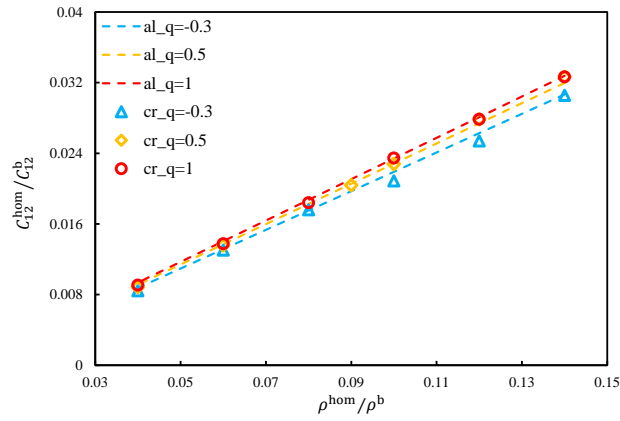
FIG. 2.14 compares the evolutions of the normalized properties with the relative density between the analytical laws (EQ. 2.27-EQ. 2.31) and the computational results. Four sets of data with ($t = \{0.33; 0.38; 0.43; 1\}$) are shown in the figures. The analytic laws show a satisfying agreement with the computational results. The mean relative errors of $C_{11}^{\text{hom}}/C_{11}^{\text{b}}$, $C_{12}^{\text{hom}}/C_{12}^{\text{b}}$ and $C_{44}^{\text{hom}}/C_{44}^{\text{b}}$ are 2.47%, 1.75% and 3.04% respectively for all data.

With the satisfactory agreement presented in FIG. 2.14 and FIG. 2.12, EQ. 2.27-EQ. 2.29 have been proven to be appropriate for Kelvin open-cell foams with t or q by taking into account the morphological functions ($\phi_1(t); \phi_2(t); \phi_3(t); \phi_4(t)$) or ($\phi_1(q); \phi_2(q); \phi_3(q); \phi_4(q)$).

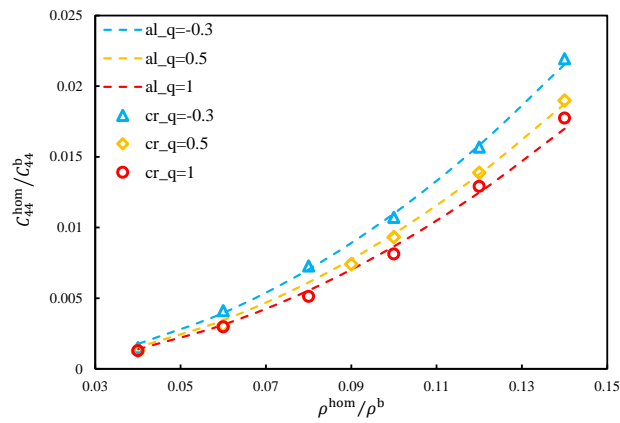
2. Effective elastic properties of regular Kelvin open-cell foams



(a)



(b)



(c)

FIGURE 2.12: Evolutions of (a) C_{11}^{hom}/C_{11}^b , (b) C_{12}^{hom}/C_{12}^b and (c) C_{44}^{hom}/C_{44}^b with respect to the relative density by the analytical laws (al) and the computational results (cr) with $(q = \{-0.3; 0.5; 1\})$.

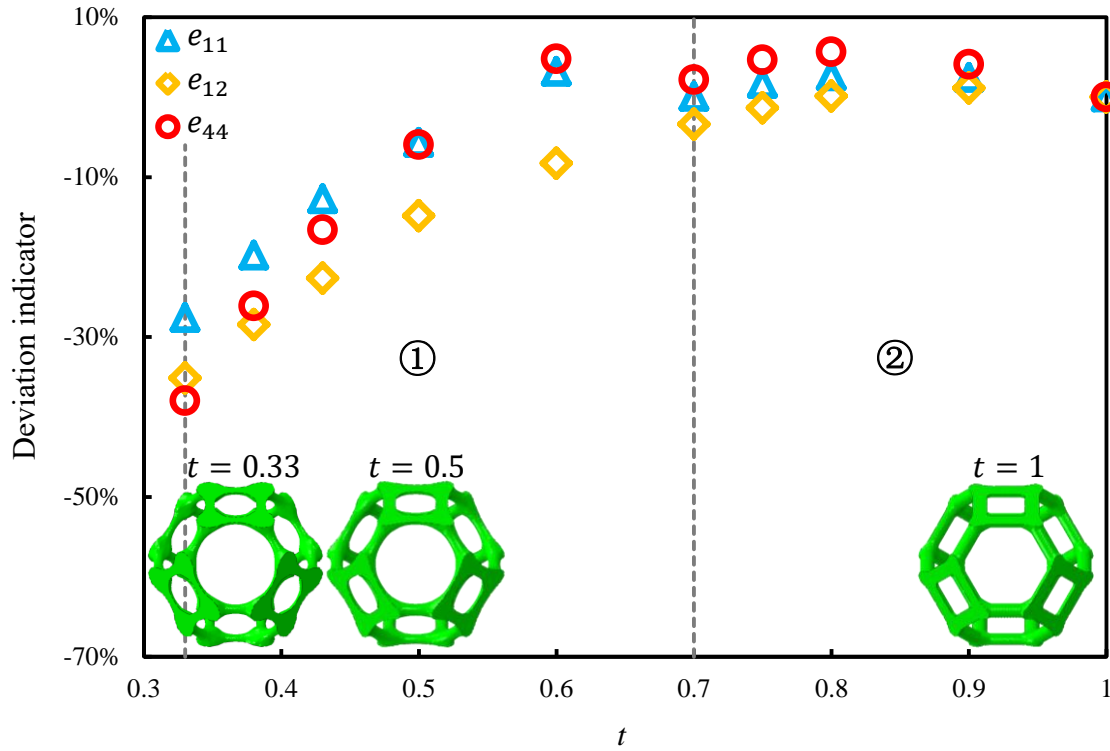


FIGURE 2.13: Effect of the diameter ratio for the models ($\rho^{\text{hom}}/\rho^{\text{b}} = 6\%$, $q = 1$, *Kelvin*) on the deviation indicators.

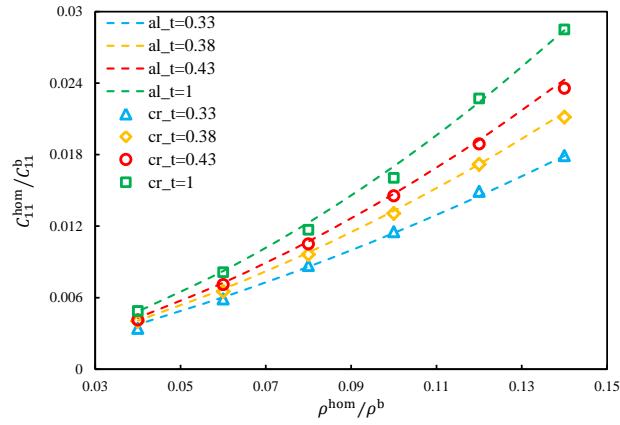
5.5 Effect of irregularity and dispersion of cell size distribution

The influences of the irregularity and the dispersion of cell size distribution are discussed simply in this section. The study of irregular open-cell foam will be expanded in detail in the next chapter.

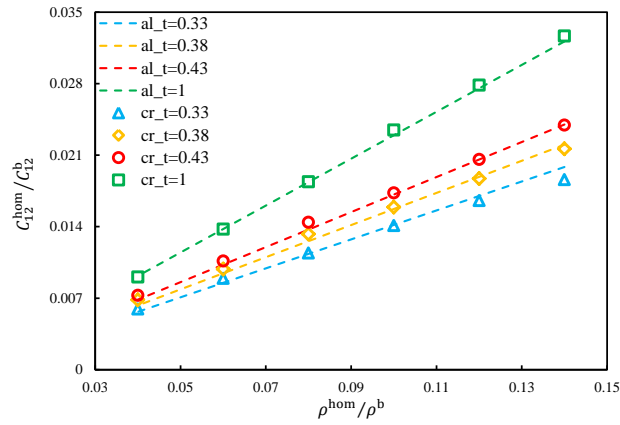
As [KAN 03, PEL 09] introduced, the behavior of a random small volume element of irregular foams will not be isotropic even if the microstructure is expected to be macroscopically isotropic. In order to obtain the isotropic behavior, one way is to use a large enough RVE and the other way is to take into account the statistical mean value with sufficient realizations for small RVE [KAN 03]. The number of realizations and the size of the RVE should be balanced. In order to show the effect of the irregularity and the dispersion of cell size distribution, Kelvin open-cell model and irregular open-cell models with different C_V s ($C_V = \{0; 0.05; 0.1\}$) are considered, which are illustrated in TAB. 2.3. Both regular Kelvin model and irregular models have same number of cells and same morphological parameters ($\rho^{\text{hom}}/\rho^{\text{b}} = 6\%$, $q = 1$, $t = 1$).

For RVEs with fixed volume and microstructures expected to be macroscopically isotropic, the overall isotropy would be achieved after a sufficient number of realizations.

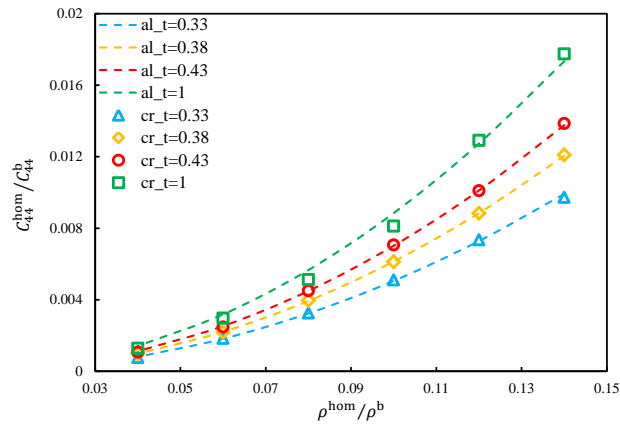
2. Effective elastic properties of regular Kelvin open-cell foams



(a)



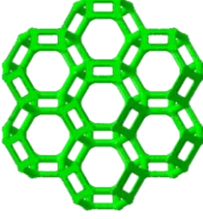
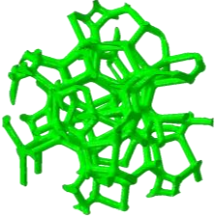
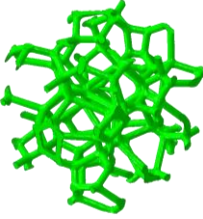
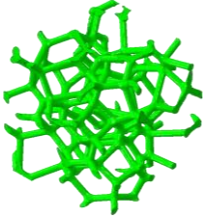
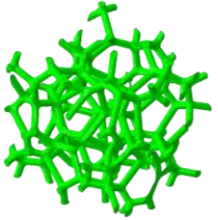
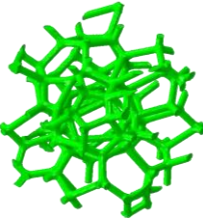
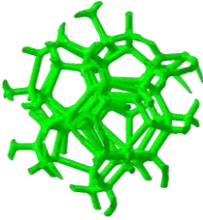
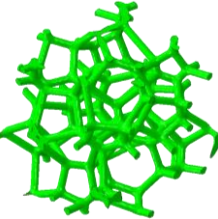
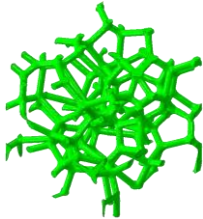
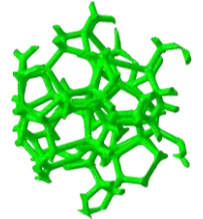
(b)



(c)

FIGURE 2.14: Evolutions of (a) C_{11}^{hom}/C_{11}^b , (b) C_{12}^{hom}/C_{12}^b and (c) C_{44}^{hom}/C_{44}^b with respect to the relative density by the analytical laws (al) and the computational results (cr) with ($t = \{0.33; 0.38; 0.43; 1\}$).

TABLE 2.3: Illustration of Kelvin structure and irregular structures with different C_V s.

Model	Structure		
Kelvin			
$C_V = 0$			
$C_V = 0.05$			
$C_V = 0.1$			

Hence the statistical mean of effective stiffness matrix is given by :

$$\overline{[\mathbb{C}^{\text{hom}}]} = \frac{1}{n_r} \sum_{m=1}^{n_r} [\mathbb{C}^{\text{hom}}]_m, \quad (2.32)$$

where n_r means the number of realizations and $[\mathbb{C}^{\text{hom}}]_m$ is the obtained effective stiffness matrix of the m th realization. In order to determine whether the number of realization is sufficient, the difference in the mean effective stiffness matrix between two consecutive realization step is computed [DÜS 12], such that :

$$\zeta_{conv} = \frac{\left\| \overline{[\mathbb{C}^{\text{hom}}]}_{n_r} - \overline{[\mathbb{C}^{\text{hom}}]}_{n_r-1} \right\|_{Frob}}{\left\| \overline{[\mathbb{C}^{\text{hom}}]}_{n_r-1} \right\|_{Frob}}, \quad (2.33)$$

2. Effective elastic properties of regular Kelvin open-cell foams

where $\|\bullet\|_{Frob}$ is the FROBENIUS norm. The number of realizations is considered to be sufficient if $\zeta_{conv} < 3 \times 10^{-3}$. For every C_V , the required number of realizations is around 25.

In order to quantify the overall isotropy of the effective behavior, the overall isotropy criterion is introduced [GAT 05] :

$$\zeta_{iso}(\overline{\mathbb{C}^{hom}}) = \frac{\|\overline{\mathbb{C}^{hom}} - \mathcal{P}_{iso}(\overline{\mathbb{C}^{hom}})\|}{\|\overline{\mathbb{C}^{hom}}\|}, \quad (2.34)$$

where $\|\mathbb{T}\| = \mathbb{T} :: \mathbb{T}$ is a norm of symmetric fourth order tensors and $\mathcal{P}_{iso}(\mathbb{T})$ is a projection over the isotropic frame of the symmetric fourth order tensors, i.e.

$$\mathcal{P}_{iso}(\mathbb{T}) = \frac{\mathbb{T} :: \mathbb{J}}{\mathbb{J} :: \mathbb{J}} \mathbb{J} + \frac{\mathbb{T} :: \mathbb{K}}{\mathbb{K} :: \mathbb{K}} \mathbb{K}. \quad (2.35)$$

Using the Voigt modified matrix notations, Eqs. 2.34 and 2.35 have the form that

$$\zeta_{iso}([\overline{\mathbb{C}^{hom}}]) = \frac{\|[\overline{\mathbb{C}^{hom}}] - \mathcal{P}_{iso}([\overline{\mathbb{C}^{hom}}])\|_{Frob}}{\|[\overline{\mathbb{C}^{hom}}]\|_{Frob}}, \quad (2.36)$$

and

$$\mathcal{P}_{iso}([\overline{\mathbb{C}^{hom}}]) = \frac{tr([\overline{\mathbb{C}^{hom}}][\mathbb{J}])}{tr([\mathbb{J}][\mathbb{J}])} [\mathbb{J}] + \frac{tr([\overline{\mathbb{C}^{hom}}][\mathbb{K}])}{tr([\mathbb{K}][\mathbb{K}])} [\mathbb{K}], \quad (2.37)$$

with tr the trace of the matrix. The mean effective stiffness matrix is considered isotropic when $\zeta_{iso}([\overline{\mathbb{C}^{hom}}]) < 2\%$. The obtained $\mathcal{P}_{iso}([\overline{\mathbb{C}^{hom}}])$ is regarded as the final isotropic matrix.

All models are meshed with almost 430,000 elements. The comparison of $\overline{C_{11}^{hom}}$, $\overline{C_{12}^{hom}}$ and $\overline{C_{44}^{hom}}$ of Kelvin model and irregular models is shown in TAB. 2.4. One can see that the difference of three mean effective properties is great between Kelvin model and irregular models, while the difference among irregular models with different C_V s is negligible. It can be concluded that in the range $[0,0.1]$, the effect of the dispersion of cell size distribution is not obvious on effective elastic properties.

TABLE 2.4: The comparison of mean effective properties among Kelvin model and irregular models ($C_V = \{0; 0.05; 0.1\}$).

	$\overline{C_{11}^{\text{hom}}}$ (MPa)	$\overline{C_{12}^{\text{hom}}}$ (MPa)	$\overline{C_{44}^{\text{hom}}}$ (MPa)
Kelvin	769.35	542.73	84.25
$C_V = 0$	710.37	504.30	103.04
$C_V = 0.05$	709.98	505.48	102.25
$C_V = 0.1$	709.27	502.99	103.14

6 Conclusion

In this chapter, a methodology is introduced to generate realistic open-cell foam structures. A micromechanical modeling based on Hill's lemma is developed to numerically compute the effective elastic properties of foam materials with no need to impose boundary loadings. In addition, the effects of morphological parameters on regular Kelvin open-cell foams are analysed. The main conclusions are listed here :

1. A Hill's lemma based computational homogenization approach is proposed to evaluate the effective elastic properties numerically. The approach is limited to linearized elasticity with small perturbations strictly so far. The HL-FEM has the same advantages as VAMUCH [YU 07a] comparing to usual FEM-based approaches : with only one calculation, the full effective elastic stiffness matrix can be obtained without elementary loadings. This approach has been validated by comparing with usual computational homogenization approach realized by Abaqus.
2. Four morphological parameters, i.e. the relative density, the cell size distribution and the way the solid distributed along cell struts (characterized by normalized curvature q and diameter ratio t) allow to stand for the microstructure of open-cell foams. The influences of these morphological parameters on effective elastic properties are investigated. For regular Kelvin open-cell foams, relative density is the most influential parameter. Strut minimum to maximum diameter and strut cross section are also proven to have significant effects in the certain range. For irregular open-cell foams, there is no obvious effect of the dispersion of cell size distribution in the current range. With the assessments, new generic laws for Kelvin open-cell foams are raised to describe the relations among the effective elastic properties, the relative density and the diameter ratio or the normalized curvature. The analytical laws have a good agreement with the numerical results.

Chapter 3

Effective elastic properties of periodic irregular open-cell foams

Following the investigation of regular Kelvin open-cell foams in the previous chapter, we concentrate on the irregular open-cell foams in this chapter. In order to generate realistic periodic irregular open-cell structures, the tomography slices of the real irregular open-cell sample are analyzed to obtain its morphological description. Hill's lemma computational homogenization approach is still used to estimate the effective elastic properties. In this chapter, due to the random distribution of cells, the determination of the RVE and the importance of choosing the RVE parameters, i.e. the number of realizations and the volume of RVE, on the accuracy of models are focused on. The efficiency of different approaches is discussed while some recommendations and improvements are raised. The main results are published in the paper : Zhu, W., Blal, N., Cunsolo, S., & Baillis, D. (2018). Effective elastic properties of periodic irregular open-cell foams. International Journal of Solids and Structures.

Contents

1	Introduction	57
2	Modeling of irregular open-cell structure from tomography slices	57
2.1	Morphological analysis of open-cell foam	57
2.2	Generations of numerical structures	61
3	RVE determination approach	62
3.1	Kanit's relation for linear properties [KAN 03]	62
3.2	Moussaddy's algorithm [MOU 13]	64
4	Numerical simulation	66
5	Results and discussion	67
5.1	Influence of RVE parameters	67
5.2	Results of Kanit's method	67
5.3	Results of Moussaddy's algorithm	72
5.4	New suggestions of the determination of the RVE	76
6	Conclusion	78

1 Introduction

X-ray tomography has been verified as a powerful non-destructive approach which can supply directly the images of the heterogeneous materials at the relevant scale [BAB 07]. With tomography slices, [MAI 03] described the microstructure of cellular materials. [BAD 00] created the realistic open-cell nickel foams by tomography technique and investigated the Young's modulus, the compression yield stress and the tensile fracture stress of this foam material. The results have also been compared to the model presented in [GIB 97]. The computed X-ray tomography can be used not only to characterize microstructures of foams, but also to observe the evolution of dynamic crushing in compression experiments [JAN 09]. Since the structures reconstructed by tomography are usually non-periodic and it is difficult to impose the periodic boundary condition on non-periodic structure (see Appendix B), Voronoi diagram is often performed to generate periodic foam structures [BAR 14a, YE 15, BAI 17] so that the periodic boundary condition could be imposed easily.

In this chapter, the structure of the real irregular open-cell foam is reconstructed by micro-computed tomography and its morphological characterizations are analyzed by iMorph [BRU 08]. Using the Voronoi diagram approach, the numerical periodic irregular open-cell structures with the same morphological features as the real foam are generated by considering the tomography data. Hill's lemma computational homogenization approach is still used to predict the effective elastic properties. Two RVE determination approaches [MOU 13, KAN 03] are carried out and their efficiency and accuracy are discussed. Specific methods are proposed for foam models based on these two approaches.

2 Modeling of irregular open-cell structure from tomography slices

2.1 Morphological analysis of open-cell foam

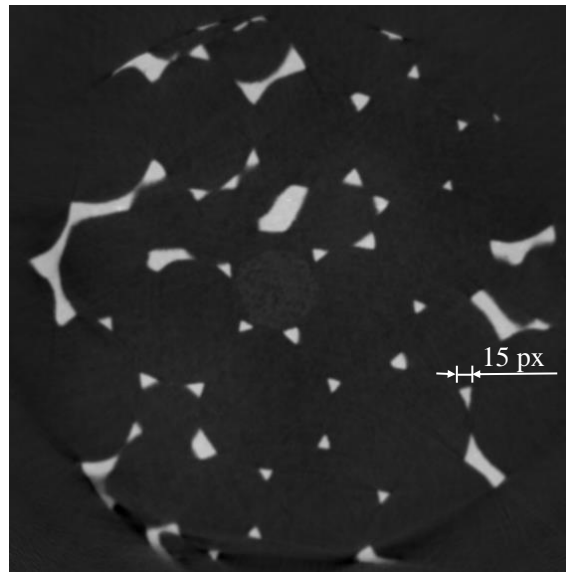
FIG. 3.1 presents a typical tomography slice of the aluminum foam and the reconstructed microstructure by micro-computed tomography. The resolution of the tomography slices and the nominal porosity are 22 μm per voxel and 94%, respectively.

2.1.1 Characterization of the geometry - covariance function

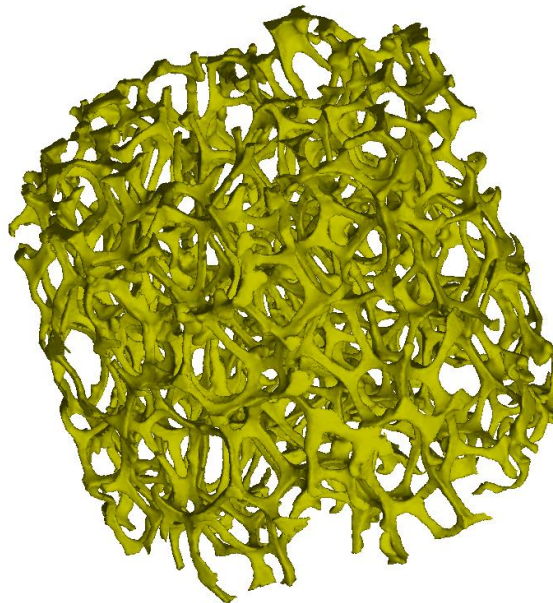
In order to characterize stationary and ergodic media, the covariance function and relevant integral range have been raised as the basic statistical descriptors [MAT 75]. Considering a set X , the covariance function $C(X, \mathbf{h})$ represents the probability of two points \mathbf{x} and $\mathbf{x} + \mathbf{h}$ belonging to set X , and it can be written as :

$$C(X, \mathbf{h}) = P\{\mathbf{x} \in X, \mathbf{x} + \mathbf{h} \in X\}, \quad (3.1)$$

where the vector \mathbf{h} means the space of these two points. Assuming $h = \|\mathbf{h}\|$, for $h = 0$, $C(X, 0)$ stands for the solid volume fraction of set X , while for $h \rightarrow +\infty$, the covariance



(a)



(b)

FIGURE 3.1: Tomographic data of the irregular open-cell structure : (a) slice of the sample ($571 \times 571 \text{ px}^2$); (b) 3D rendering after reconstruction ($571 \times 571 \times 484 \text{ px}^3$).

has an asymptotic value which is the square of the solid volume fraction. If the asymptotic value can be obtained before $h \rightarrow +\infty$, for example when $h = \mathcal{A}$, then the points are considered not correlated with the space larger than \mathcal{A} [MAT 71], and this space \mathcal{A} is the covariance range. The covariances of the microstructure of the irregular open-cell sample in three directions are illustrated in FIG. 3.2. From the figure, one can see the

covariance range, i.e. the intersection of the covariance functions and the asymptotic value, is about 55 px. Furthermore, the microstructure is considered geometrically isotropic because three covariance functions are similar in three directions.

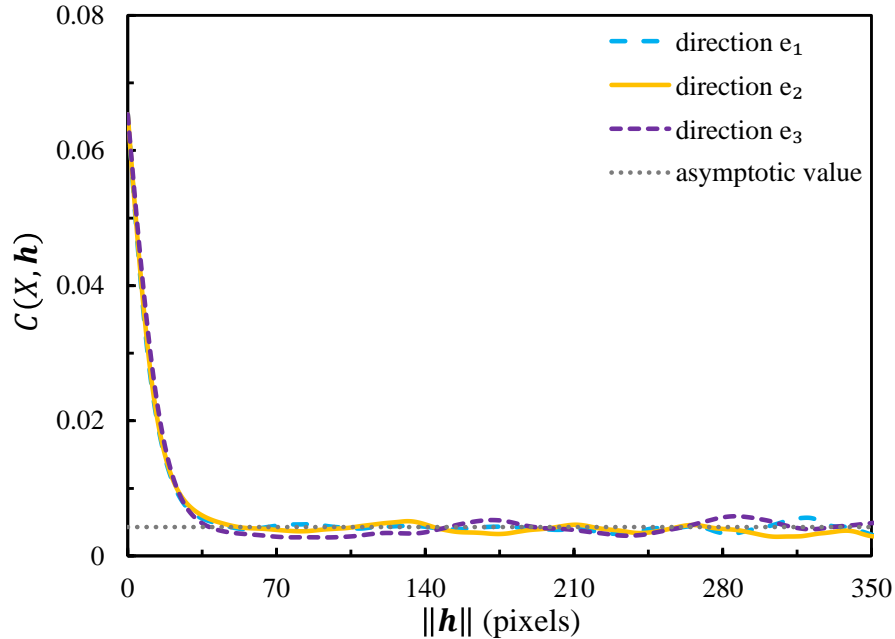


FIGURE 3.2: Covariance functions in three directions of solid phase of open-cell sample microstructure.

2.1.2 Morphological parameters

Recall four morphological parameters (introduced in previous chapter) which can represent the microstructure of open-cell foam models :

- Relative density, $\rho^{\text{hom}}/\rho^{\text{b}}$, is the solid volume fraction.
- Coefficient of variation, C_V , stands for the dispersion of cell size distribution of irregular structures. One has $C_V = \sigma_{d_c}/\bar{d}_c$, where σ_{d_c} is the standard deviation of equivalent cell diameters and \bar{d}_c denotes average cell diameter.
- Normalized curvature, q , shows the shape of cross section of strut. By controlling q , the shape of cross section can vary from circle ($q = 1$) to convex triangle ($1 > q > 0$) to flat triangle ($q = 0$) and to concave triangle ($0 > q \geq -0.5$).
- Diameter ratio, t , describes the variation of the cross section area of along the strut axis and $t = d_{\text{min}}/d_{\text{max}}$, where d_{min} and d_{max} are the minimum and maximum diameter of the strut.

3. Effective elastic properties of periodic irregular open-cell foams

In order to obtain the morphological parameters of the structure of the irregular open-cell sample, the tomographic slices are analyzed using the free software iMorph. The equivalent cell diameters show a Gaussian unimodal distribution with $\bar{d}_c = 2892 \mu\text{m}$ and $C_V = 3.39\%$. In the previous chapter, the normalized curvature q and the diameter ratio t demonstrate their significant influences on the effective elastic properties of open-cell foams. Hence these two parameters are necessary to be considered when generating structures. Two analytical relations among q , t and stereological parameters are proposed in [CUN 17] as :

$$4S_{sur}/d_o^2 = 1.11q + 1.52, \quad (3.2)$$

$$\frac{d_o + d_i}{2d_{j,max}} = t^{\frac{2}{3}}, \quad (3.3)$$

where S_{sur} denotes the strut cross section surface, d_o stands for the strut cross section circumcircle diameter, d_i represents the strut cross section incircle diameter and $d_{j,max}$ is the strut junction maximum diameter. FIG. 3.3 illustrates these stereological parameters. These parameters can be obtained directly by the cross section measurement function and the strut junctions measurement function of iMorph. Finally, the morphological parameters of the irregular open-cell sample are ($\rho^{\text{hom}}/\rho^{\text{b}} = 6.4\%$; $C_V = 3.4\%$; $q = 0.36$; $t = 0.34$).

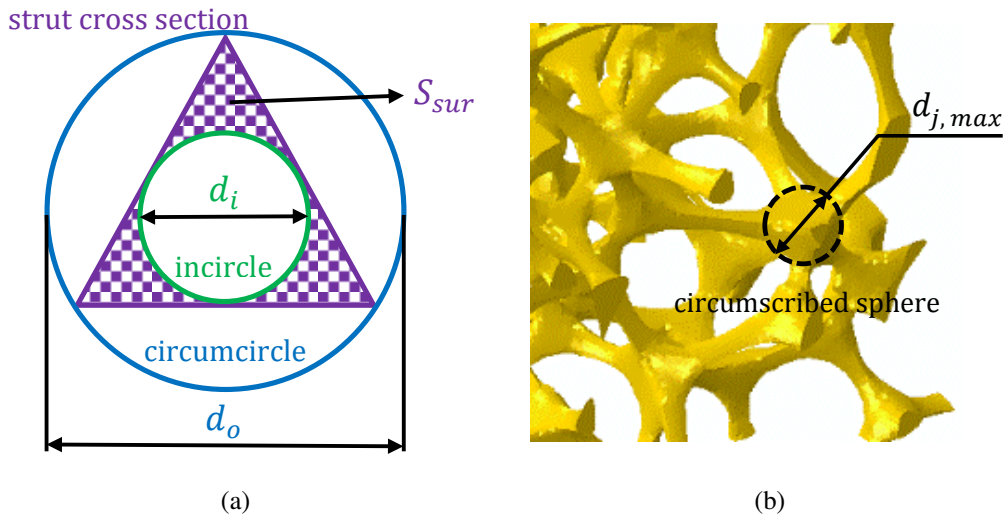


FIGURE 3.3: (a) Illustration of S_{sur} , d_o and d_i in the case $q = 0$ (flat triangle cross section); (b) Illustration of $d_{j,max}$.

2.2 Generations of numerical structures

With the obtained morphological parameters, five sets of numerical structures with different sizes are generated by Matlab [MAT 16]. FIG. 3.4 presents the illustration of structures for Set A*, Set B*, Set C*, Set D* and Set E*, respectively. Table 3.1 introduces the characterizations, i.e. the domain dimensions and the number of cells, of each set. The ratio of the number of cells to the volume of the structure keeps constant for each set, which is determined by morphological analysis.

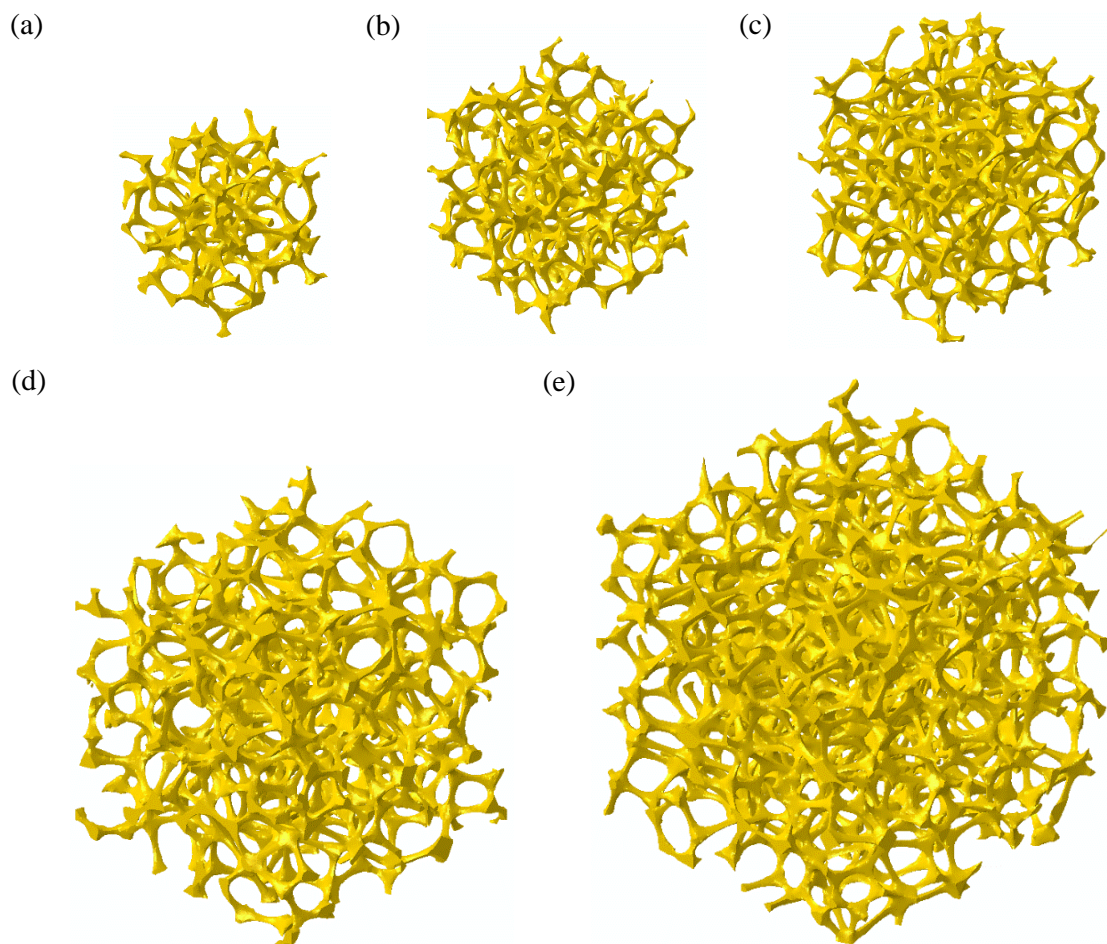


FIGURE 3.4: Illustration of numerical irregular open-cell structure ($\rho^{\text{hom}}/\rho^{\text{b}} = 6.4\%$) for (a) Set A* ; (b) Set B* ; (c) Set C* ; (d) Set D* and (e) Set E* .

TABLE 3.1: Characterizations of each set of open-cell structures ($\rho^{\text{hom}}/\rho^{\text{b}} = 6.4\%$).

	Domain dimensions (px ³)	Number of cells
Set A*	307 × 307 × 307	20
Set B*	400 × 400 × 400	44
Set C*	450 × 450 × 450	63
Set D*	500 × 500 × 500	86
Set E*	600 × 600 × 600	149

3 RVE determination approach

Two approaches proposed in literatures are introduced in this section and will be performed to determine two RVE parameters : the number of realizations n_r and the RVE volume V .

3.1 Kanit's relation for linear properties [KAN 03]

As presented in [MAT 71], the integral range for set X can be written as follows since covariance function (EQ. 3.1) is integrable :

$$\mathcal{A}^n = \frac{1}{C(X, \mathbf{0}) - C(X, \mathbf{0})^2} \int_{\mathbb{R}^n} (C(X, \mathbf{h}) - C(X, \mathbf{0})^2) d\mathbf{h}, \quad (3.4)$$

where n signifies the dimension of the space. The parameters estimated in \mathcal{A}^n have a good statistical representativeness. Moreover [KAN 03] put forward that \mathcal{A} can predict the fluctuation (or equivalently variance in statistics) of any arbitrary scalar variable.

Since the covariance functions shows a statistically morphological isotropy in FIG. 3.2 and the bulk property is isotropic as well, the overall effective property of irregular open-cell foams is expected to be isotropic. Hence according to EQ. 1.8, the effective stiffness matrix can be represented by the effective bulk modulus k^{hom} and the effective shear modulus μ^{hom} as :

$$\mathbb{C}^{\text{hom}} = 3k^{\text{hom}}\mathbb{J} + 2\mu^{\text{hom}}\mathbb{K}. \quad (3.5)$$

Recall that \mathbb{J} and \mathbb{K} stand for the classical isotropy basis components of isotropic fourth order symmetric tensors.

The statistical mean values of effective elastic moduli k^{hom} and μ^{hom} with n_r realizations are given by :

$$\overline{z^{\text{hom}}} = \frac{1}{n_r} \sum_{m=1}^{n_r} z_m^{\text{hom}}, \quad (3.6)$$

where z denotes k or μ , and m means the m th realization. The variance $D_z^2(V)$ of its mean value $\bar{z}(V)$ over the volume V is calculated as :

$$D_z^2(V) = \frac{1}{n_r - 1} \sum_{m=1}^{n_r} \left(z_m^{\text{hom}} - \bar{z}^{\text{hom}} \right)^2. \quad (3.7)$$

The total number of realizations of each set is required to make sure that the mean effective elastic moduli \bar{z}^{hom} and their variances $D_z^2(V)$ do not vary any longer up to given precisions (less than 0.2% for the mean moduli and 1% for the variances in our case), such that :

$$e_Z = \frac{|Z_{n_r} - Z_{n_r-1}|}{Z_{n_r-1}} \leq p, \quad (3.8)$$

where Z stands for \bar{z}^{hom} or $D_z^2(V)$, and p equals to 0.2% or 1%.

For a random function $z(x)$, a function is proposed in [KAN 03] as :

$$D_z^2(V) = D_z^2 \times \left(\frac{\mathcal{A}^3}{V} \right)^\alpha. \quad (3.9)$$

Here D_z^2 is the point variance of $z(x)$ and \mathcal{A}^3 is the integral range of $z(x)$. Considering the relative density $\rho^{\text{hom}}/\rho^{\text{b}}$ and the elastic modulus z^{b} of the bulk, for foam models, the point variance D_z^2 can be written as [CAI 94] :

$$D_z^2 = \frac{\rho^{\text{hom}}}{\rho^{\text{b}}} \left(1 - \frac{\rho^{\text{hom}}}{\rho^{\text{b}}} \right) \left(z^{\text{b}} \right)^2. \quad (3.10)$$

Substituting EQ. 3.10 into EQ. 3.9, the variance can be represented as a function of the relative density, the property of the bulk, the volume of RVE and the integral range :

$$D_z^2(V) = \frac{\rho^{\text{hom}}}{\rho^{\text{b}}} \left(1 - \frac{\rho^{\text{hom}}}{\rho^{\text{b}}} \right) \left(z^{\text{b}} \right)^2 \left(\frac{\mathcal{A}^3}{V} \right)^\alpha. \quad (3.11)$$

While in practice, a given error ε must be considered for the determination of the volume of the RVE. The absolute error of the mean value after n_r realizations of volume V is deduced with the interval of confidence, such that :

$$\varepsilon_{\text{abs}} = \frac{2D_z(V)}{\sqrt{n_r}}. \quad (3.12)$$

Then the relative error $\varepsilon_{\text{rela}}$ is :

$$\varepsilon_{\text{rela}} = \frac{\varepsilon_{\text{abs}}}{\bar{z}^{\text{hom}}} = \frac{2D_z(V)}{\bar{z}^{\text{hom}} \sqrt{n_r}}. \quad (3.13)$$

3. Effective elastic properties of periodic irregular open-cell foams

The relations between two RVE parameters, n_r and V , could be derived from the above equations. If one fix the RVE volume V , then the required number of realizations n_r is given by :

$$n_r(V) = \left(\frac{2z^b}{\varepsilon_{rel} z^{\text{hom}}} \right)^2 \frac{\rho^{\text{hom}}}{\rho^b} \left(1 - \frac{\rho^{\text{hom}}}{\rho^b} \right) \left(\frac{\mathcal{A}^3}{V} \right)^\alpha. \quad (3.14)$$

Similarly, if the required number of realizations n_r is fixed, the smallest corresponding RVE volume V can be evaluated as :

$$V(n_r) = \left[\left(\frac{2z^b}{\varepsilon_{rel} z^{\text{hom}}} \right)^2 \frac{\rho^{\text{hom}}}{n_r \rho^b} \left(1 - \frac{\rho^{\text{hom}}}{\rho^b} \right) \right]^{1/\alpha} \mathcal{A}^3. \quad (3.15)$$

In order to determine the RVE of a given microstructure (for fixed number of realizations) or the required number of realizations (for fixed RVE volume), the following steps should be performed [KAN 03] :

1. Generate numerous realizations of the given microstructure for different sets ;
2. Calculate the effective elastic stiffness matrix of each realization ;
3. For each set, estimate the mean values (EQ. 3.6) and the variances (EQ. 3.7) and evaluate if the number of realizations meets the stabilization criterion EQ. 3.8.
4. Calculate the integral range \mathcal{A}^3 and the power α (EQ. 3.11), and derive the relation between two RVE parameters according to EQ. 3.14 or EQ. 3.15. One can obtain either the number of realizations with the volume of RVE or the volume of RVE with the number of realizations.

3.2 Moussaddy's algorithm [MOU 13]

[MOU 13] proposed the algorithm based on the combination of criteria which belong to two groups of criteria to analyze fiber models. The first group contains the criteria of the number of realizations, and the second one contains the criteria of the RVE volume (number of fibers in their paper). The determination criteria are introduced first and the general algorithm is presented after as follows.

3.2.1 Criteria of number of realizations

A number of criteria are assessed to make sure the number of realizations is large enough to have confidence in the mean effective properties.

Isotropy criterion : If the microstructure is expected to be macroscopically isotropic, although the individual realization is not isotropic for small volume element, the overall isotropy would be obtained after a sufficient number of realizations. Since the isotropy criterion has already been introduced in Section 5.5 in Chapter 2, we do not repeat here.

It should be noticed that there are several isotropy indices in the previous literatures but there is no agreement on the value of the tolerance.

Confidence criterion : The criterion is studied to determine if the 95% confidence interval relative error with a certain number of realizations is under a pre-set tolerance, such that :

$$\zeta_{con} = \frac{I_{z^{\text{hom}}}^{95\%}/2}{z^{\text{hom}}} \leqslant tol. \quad (3.16)$$

In this chapter, tol is the pre-set fixed tolerance and set as 5% according to [MOU 13]. $I_{z^{\text{hom}}}^{95\%}$ represents the 95% confidence interval of the effective elastic modulus which is derived as :

$$I_{z^{\text{hom}}}^{95\%} = I_{TS} \frac{\sigma_{z^{\text{hom}}}}{\sqrt{n_r}}. \quad (3.17)$$

Here I_{TS} denotes the inverse of Student's T cumulative distribution function with $(n_r - 1)$ degrees of freedom. $\sigma_{z^{\text{hom}}}$ stands for the standard deviation of the effective elastic modulus.

3.2.2 Criteria of RVE volume

In order to investigate the accuracy of the RVE volume, different criteria are performed for each set.

Deviation criterion : By computing the standard deviation, the deviation criterion shows the degree of discretization of the effective elastic modulus :

$$\delta_{dev} = \frac{\sigma_{z^{\text{hom}}}}{z^{\text{hom}}} \leqslant tol. \quad (3.18)$$

Averaging variations criterion : The averaging variations criterion has been proposed [MOU 13] since it can reduce the cost of the RVE determination. In previous criteria, only the arithmetic mean value of the effective elastic modulus $\overline{z^{\text{hom}}}$ is taken into account. In the averaging variations criterion, both the arithmetic and harmonic means are considered. The arithmetic mean is introduced before (EQ. 2.32) and the harmonic mean effective elastic stiffness matrix can be written as :

$$[\underline{\mathbb{C}}^{\text{hom}}] = \left(\frac{1}{n_r} \sum_{m=1}^{n_r} [\mathbb{C}_m^{\text{hom}}]^{-1} \right)^{-1}. \quad (3.19)$$

The average of two means is considered as the average property after n_r realizations :

$$\widehat{z^{\text{hom}}} = \frac{\overline{z^{\text{hom}}} + z^{\text{hom}}}{2}. \quad (3.20)$$

This criterion presents the RVE is found only when the difference between the average property \widehat{z}^{hom} and $\overline{z}^{\text{hom}}$ or $\underline{z}^{\text{hom}}$ is under the tolerance 5% :

$$\delta_{ave} = \left| \frac{\widehat{z}^{\text{hom}} - \overline{z}^{\text{hom}}}{\widehat{z}^{\text{hom}}} \right| = \left| \frac{\widehat{z}^{\text{hom}} - \underline{z}^{\text{hom}}}{\widehat{z}^{\text{hom}}} \right| \leqslant tol. \quad (3.21)$$

Effective property error : The effective property error with respect to the properties of the largest volume has the form :

$$\delta_{err} = \frac{|\overline{z}^{\text{hom}}(V) - \overline{z}^{\text{hom}}(V_{max})|}{\overline{z}^{\text{hom}}(V_{max})} \leqslant tol, \quad (3.22)$$

where V_{max} indicates the largest volume.

3.2.3 Determination algorithm

For Moussaddy's algorithm, each RVE determination Method (M) contains a combination of both a criterion of number of realizations and a criterion of RVE volume. Hence a total of 6 methods can be estimated, and they are named as : $M_{\zeta_{iso}\delta_{dev}}$, $M_{\zeta_{iso}\delta_{ave}}$ and $M_{\zeta_{iso}\delta_{err}}$, $M_{\zeta_{con}\delta_{dev}}$, $M_{\zeta_{con}\delta_{ave}}$, $M_{\zeta_{con}\delta_{err}}$. Similarly, the following steps are necessary for each method :

1. From small volume, generate and solve realizations until a criterion in the first group (number of realizations) is satisfied;
2. If a criterion in the second group (volume of RVE) is satisfied, the RVE is found; Otherwise, increase the volume and repeat from step 1.

4 Numerical simulation

The bulk properties of aluminum are set as Young's modulus $E^b = 70$ GPa and Poisson's ratio $\nu^b = 0.3$. The generated geometries are meshed with linear tetrahedron solid elements in the commercial package ICM CFD 16.2 [ANS 13] and solved by Hill's lemma approach (realized by Matlab [MAT 16]). The convergence approach is still used to reduce the mesh discretization error.

For Set E^* , the obtained overall effective elastic stiffness matrix after 25 realizations in the frame (e_1, e_2, e_3) is :

$$[\overline{C}^{\text{hom}}] = \begin{bmatrix} 531.71 & 308.67 & 310.26 & \sim 0 & \sim 0 & \sim 0 \\ & 533.69 & 310.94 & \sim 0 & \sim 0 & \sim 0 \\ & & 532.93 & \sim 0 & \sim 0 & \sim 0 \\ & Sym & & 228.60 & \sim 0 & \sim 0 \\ & & & & 229.86 & \sim 0 \\ & & & & & 228.70 \end{bmatrix} \text{ (MPa)}.$$

Meanwhile the isotropy criterion ζ_{iso} equals to 0.46%, which means the effective stiffness matrix can be considered isotropic. Hence $[\overline{\mathbb{C}^{hom}}]$ can be rewritten equivalently as follows :

$$[\overline{\mathbb{C}^{hom}}] = 3\overline{k^{hom}}[\mathbb{J}] + 2\overline{\mu^{hom}}[\mathbb{K}], \quad (3.23)$$

with $\overline{k^{hom}} = 384.45$ MPa and $\overline{\mu^{hom}} = 113.41$ MPa.

5 Results and discussion

5.1 Influence of RVE parameters

The influence of the number of realizations is studied by evaluating the evolutions of the effective elastic moduli. The evolutions of $\overline{k^{hom}}$ and $\overline{\mu^{hom}}$ as a function of the number of realizations for Set D* is reported in FIG. 3.5(a). Both two mean effective elastic moduli have same tendency, i.e. gradually converging after small perturbations. Similar tendency can be observed on the other four sets. FIG. 3.5(b) plots the evolutions of $\overline{k^{hom}}$ for all five sets. It is obvious from the figure that in general the evolution trends to converge earlier with the increase of RVE volume. The convergence values of all sets are very close, except for Set A* (higher). As explained in [KAN 03] and [MOU 13], the bias is caused by the deterministic size effects (e.g., boundary effects).

The convergent $\overline{k^{hom}}/k^b$ and $\overline{\mu^{hom}}/\mu^b$ of each set with sufficient realizations estimated by EQ. 3.8 are shown in FIG. 3.6. From the figure, it is clear that both $\overline{k^{hom}}/k^b$ and $\overline{\mu^{hom}}/\mu^b$ of Set A* are higher than those of the other sets.

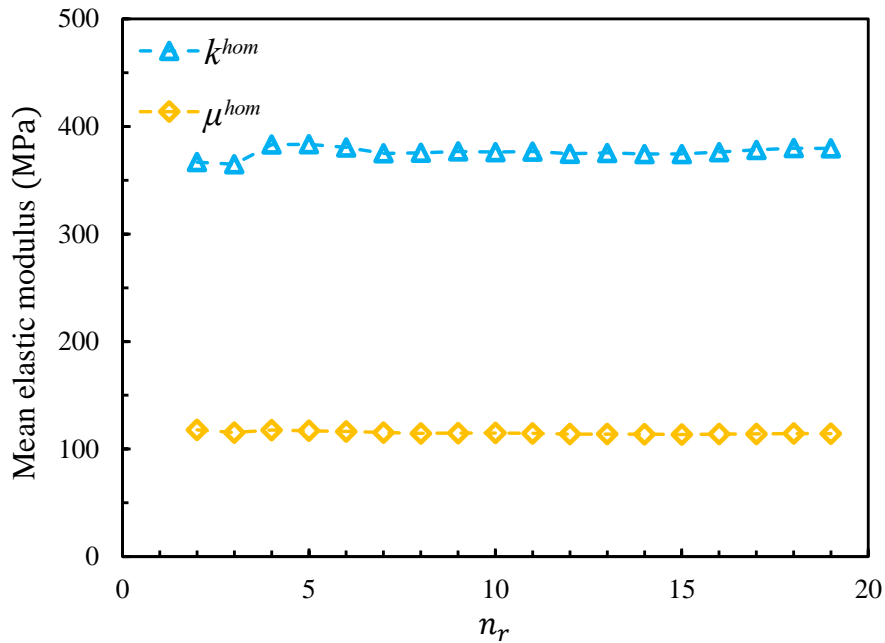
5.2 Results of Kanit's method

5.2.1 Estimation of the relation between the RVE parameters

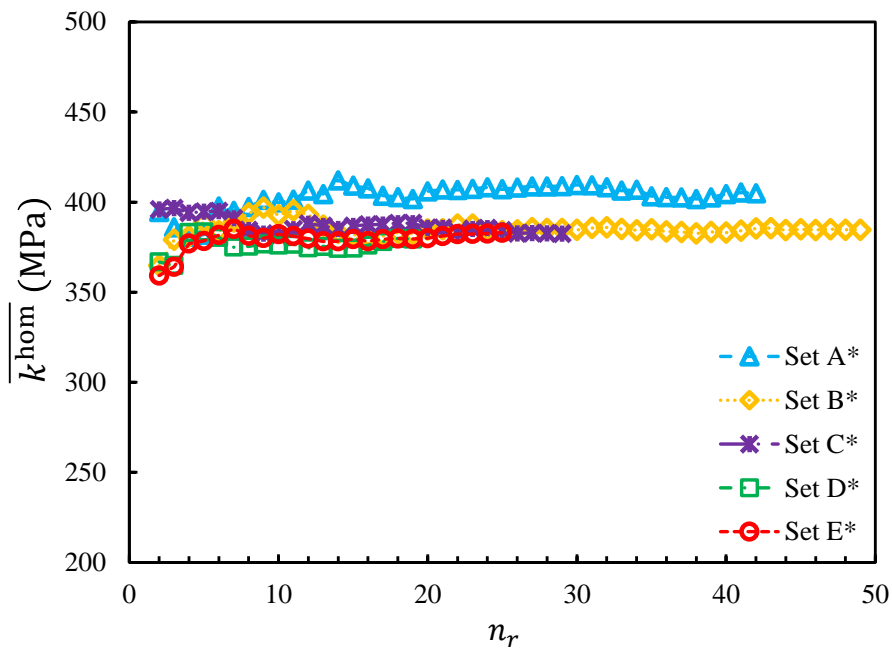
The point variances of the elastic moduli D_k^2 and D_μ^2 equals to 2.04×10^8 (MPa)² and 4.34×10^7 (MPa)² with the previous data. FIG. 3.7 plots the variance ratios $D_k^2(V)/D_k^2$ and $D_\mu^2(V)/D_\mu^2$ as a function of the volume respectively. In the figure, the simulation data are indicated as the points and the analytical law (EQ. 3.9) is named as "model". In [KAN 03], the differences between the simulation data and the fitting law are significant for the RVEs which are biased by boundary effect. Hence in our case, the fittings are carried out without the biased Set A*, while the simulation data of Set A* is still shown in the figure. One can see the analytic law fits well with the numerical results from the figure, which verifies the law is appropriate for the foam models. Table 3.2 gives the parameters \mathcal{A}^3 and α for two effective elastic moduli.

It should be noticed that in [KAN 03], the integral range has been used to investigate the RVE of Voronoi mosaic microstructures of inclusions-matrix materials. The integral range has been proven that can be considered as a morphological parameter and has the order of magnitude similar to the size of the heterogeneity in the RVE. In our case, one

3. Effective elastic properties of periodic irregular open-cell foams



(a)



(b)

FIGURE 3.5: Evolution of the mean elastic property as a function of the number of realizations : (a) $\overline{k^{hom}}$ and $\overline{\mu^{hom}}$ for Set D* ; (b) $\overline{k^{hom}}$ for each set.

can imagine FIG. 3.1(a) as a slice of the inclusion-matrix microstructure as well, where the cross-sections of the struts are equivalent to the “inclusions” (or heterogeneities) and

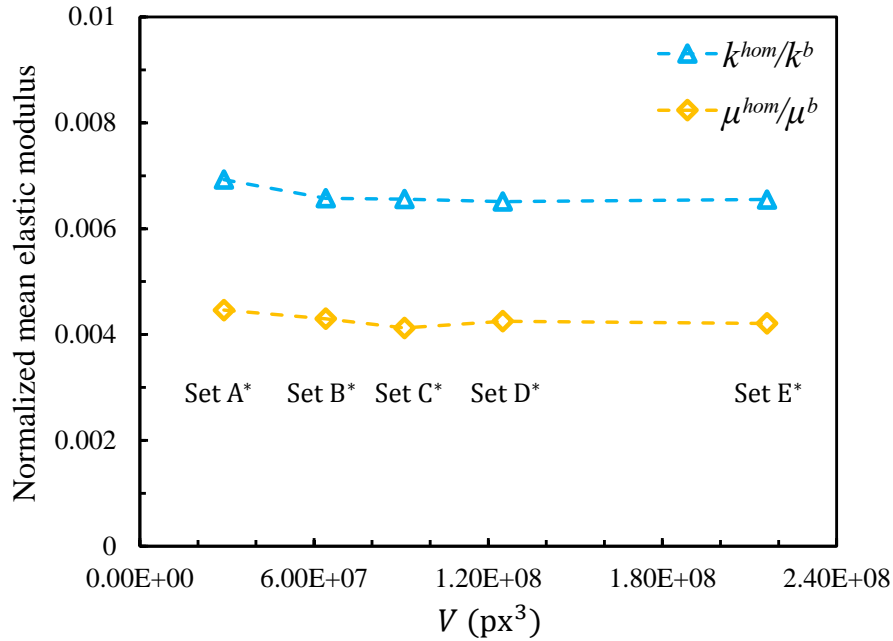


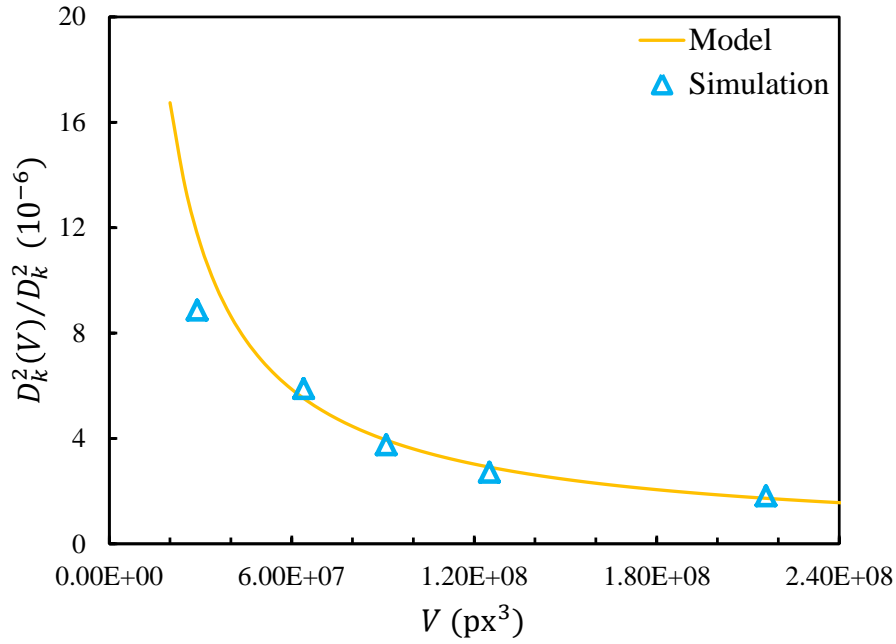
FIGURE 3.6: Evolution of the normalized mean property as a function of the RVE volume.

the porous is equivalent to the matrix. The similar orders of magnitude of the equivalent “inclusion” and the integral range are found, which makes sure that the integral range is a pure morphological parameter.

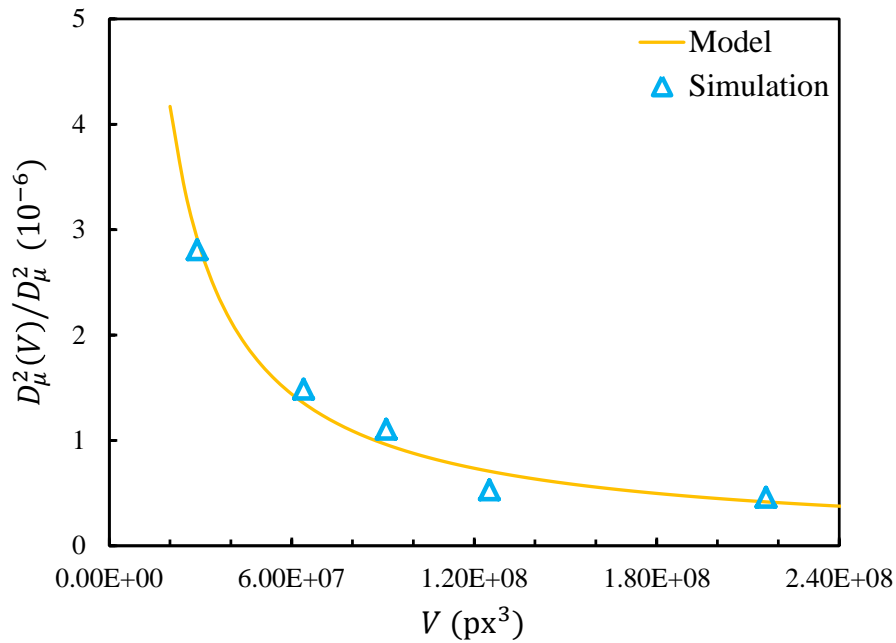
TABLE 3.2: The integral range \mathcal{A}^3 and the coefficient α for the effective elastic moduli k^{hom} and μ^{hom} , which are estimated by fitting with EQ. 3.9 ($\rho^{hom}/\rho^b = 6.4\%$).

Effective elastic modulus	Integral range \mathcal{A}^3 (px ³)	Coefficient α
k^{hom}	$10^{2.30}$	0.95
μ^{hom}	$10^{1.75}$	0.97

With the obtained parameters (\mathcal{A}^3 and α) and EQ. 3.14, Table 3.3 shows the required number of realizations to evaluate the overall effective elastic moduli k^{hom} and μ^{hom} for each set for a given ϵ_{rela} . From the table, one can see that for the foam models, the minimal number of realization of k^{hom} is always larger than that of μ^{hom} for each set. Hence the number of realizations of k^{hom} determines that of the set for the given ϵ_{rela} . Furthermore, it can be noticed that comparing with the minimal number of realizations showed in [KAN 03], only a small number of realizations are required to obtain the accurate overall effective elastic moduli for the foam models. In the same way, the smallest volume with n_r realizations for a given ϵ_{rela} can also be estimated. For example with $\epsilon_{rela} = 1\%$ and 1 realization, one should consider $V = 2.57 \times 10^{10}$ px³ for k^{hom} , and $V = 1.36 \times 10^{10}$



(a)



(b)

FIGURE 3.7: Evolution of the variance ratio $D_z^2(V)/D_z^2$ as a function of the RVE volume.

px^3 for μ^{hom} . Even if taking into account $\epsilon_{\text{rela}} = 5\%$, the needed volume is still over $5 \times 10^8 \text{px}^3$. Computing such a large model by FEM will be extremely expensive. Hence considering smaller models with a sufficient number of realizations is a better strategy.

Moreover, Kanit's relation can be regarded as the criterion to evaluate the number of realizations for each set or to evaluate the volume for a given number of realizations with ε_{rela} , which will be discussed in the following section.

TABLE 3.3: Minimal number of realizations estimated to obtain the effective elastic modulus for each set ($\rho^{hom}/\rho^b = 6.4\%$).

Relative error	$\varepsilon_{rela} = 1\%$	$\varepsilon_{rela} = 2\%$	$\varepsilon_{rela} = 5\%$
k^{hom} (Set A*)	655	164	27
μ^{hom} (Set A*)	388	97	16
k^{hom} (Set B*)	307	77	13
μ^{hom} (Set B*)	180	45	8
k^{hom} (Set C*)	219	55	9
μ^{hom} (Set C*)	128	32	6
k^{hom} (Set D*)	162	41	7
μ^{hom} (Set D*)	94	24	4
k^{hom} (Set E*)	96	24	4
μ^{hom} (Set E*)	56	14	3

5.2.2 Influence of relative density

The relative density has been proven as the most influential parameter on the effective elastic properties in the previous chapter. Hence it is interesting to study its influence on the analytic relation. The contrastive models are generated with the same parameters except $\rho^{hom}/\rho^b = 4\%$. In the same way, the overall effective elastic moduli of the contrastive models are estimated and the results are $\overline{k^{hom}} = 245.45$ MPa and $\overline{\mu^{hom}} = 45.36$ MPa. Table 3.4 and 3.5 report the parameters \mathcal{A}^3 and α , and the required number of realizations for each set for the contrastive models. Comparing with Table 3.2 and 3.3, it can be observed that the parameters \mathcal{A}^3 and α change with the variance of the relative density, and the minimal numbers of realizations are larger for the models with the smaller relative density.

TABLE 3.4: The integral range \mathcal{A}^3 and the coefficient α for the contrastive models ($\rho^{hom}/\rho^b = 4\%$).

Effective elastic modulus	Integral range \mathcal{A}^3 (px ³)	Coefficient α
k^{hom}	$10^{2.22}$	0.96
μ^{hom}	$10^{1.54}$	1.05

TABLE 3.5: Minimal number of realizations for the contrastive models ($\rho^{\text{hom}}/\rho^{\text{b}} = 4\%$).

Relative error	$\varepsilon_{\text{rela}} = 1\%$	$\varepsilon_{\text{rela}} = 2\%$	$\varepsilon_{\text{rela}} = 5\%$
k^{hom} (Set A*)	813	204	33
μ^{hom} (Set A*)	319	80	13
k^{hom} (Set B*)	380	95	16
μ^{hom} (Set B*)	139	35	6
k^{hom} (Set C*)	271	68	11
μ^{hom} (Set C*)	96	24	4
k^{hom} (Set D*)	200	50	8
μ^{hom} (Set D*)	39	18	3
k^{hom} (Set E*)	119	30	5
μ^{hom} (Set E*)	39	10	2

5.3 Results of Moussaddy's algorithm

5.3.1 Analysis of criteria of number of realizations

The variation of the isotropy criterion ζ_{iso} with the increase of the number of realizations for each set is shown in FIG. 3.8. As expected, the larger the RVE is, the more isotropic it shows. For Set A*, even with a great number of realizations, ζ_{iso} can just reach 2%, while for Set E*, only an individual model presents the better isotropy and ζ_{iso} is close to 1%. For different sets, the convergence values of the isotropy criterion are different with a sufficient number of realizations. As said before, the convergence value of Set A* just reaches 2% while for Set C*, Set D* and Set E*, the values are around 0.5%. Therefore it is difficult to define the tolerance of ζ_{iso} . In our case, the overall stiffness matrix is considered isotropic when $\zeta_{iso} \leq 1\%$. This tolerance is strict for Set A* and Set B*, while for Set C*, Set D* and Set E*, the required numbers of realizations are 5, 5 and 2, respectively.

The evolution of the confidence criterion error ζ_{con} as a function of the number of realizations for five sets is plotted in FIG. 3.9. The errors of k^{hom} and μ^{hom} are calculated for each set. It shows from the figure that in general, the confidence criterion error reduces with increasing the number of realization, no matter for different effective elastic moduli or for different sets. For models with smaller volume, more realizations are needed in general to make the error satisfy the tolerance. Assuming that for all criteria (except ζ_{iso}), the tolerance 5% should be satisfied for both elastic moduli. Hence the required numbers of realizations are 23, 16, 10, 11 and 10 for five sets, respectively.

5.3.2 Analysis of criteria of RVE volume

The influence of the RVE volume on the volume criteria δ_{dev} , δ_{ave} and δ_{err} is presented in FIG. 3.10. All errors are evaluated with the same number of realizations which satisfies

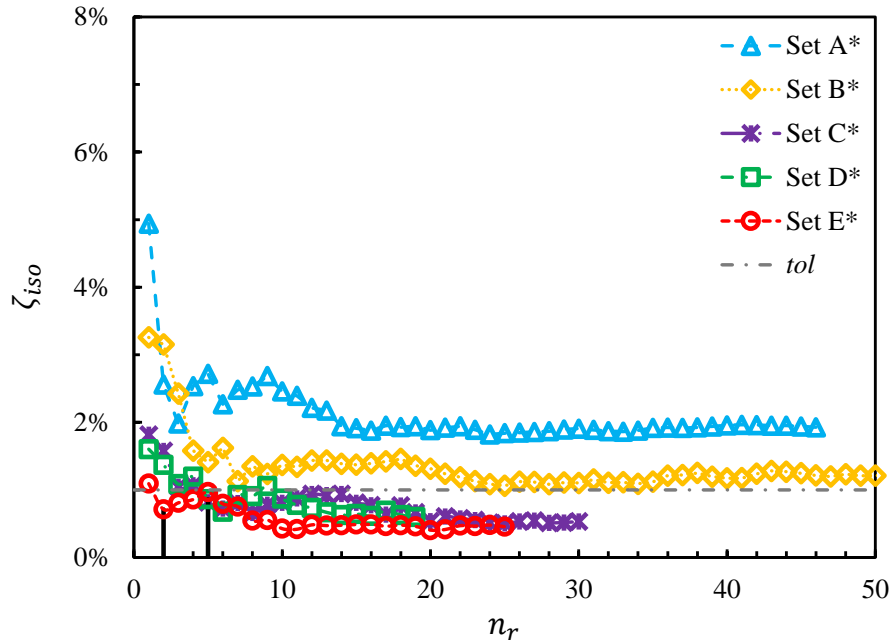


FIGURE 3.8: Evolution of ζ_{iso} as a function of the number of realizations for five sets.

the confidence criterion ζ_{con} for each set. The tolerance 5% is proposed for the fiber models, however this value is not appropriate for δ_{dev} and δ_{ave} for the foam models. The tolerance 5% is strict for δ_{dev} while too slack for δ_{ave} . From FIG. 3.10(a), the tendency of the curves shows δ_{dev} reduces with the increase of RVE volume in general. δ_{ave} has the similar tendency. On the other hand, $tol = 5\%$ is appropriate for δ_{err} . One can see clearly in FIG. 3.10(c) that δ_{err} of k^{hom} of Set A* is significant, and δ_{err} of μ^{hom} of Set A* is also close to 5%.

5.3.3 Determination of RVE parameters

Following the method introduced in Section 3.2.3, the RVE parameters are found by each method and listed in Table 3.6. As mentioned in Section 5.3.2, since $tol = 5\%$ is strict for δ_{dev} , no set satisfies $\delta_{dev} \leq 5\%$. Hence the methods which include δ_{dev} , i.e. $M_{\zeta_{con}\delta_{dev}}$ and $M_{\zeta_{iso}\delta_{dev}}$, can not determine the RVE. While $tol = 5\%$ is too slack for δ_{ave} , each set satisfies $\delta_{ave} \leq 5\%$. Therefore for the methods including δ_{dev} , only the criteria of the number of realizations works in determining the RVE, and these criteria can not avoid the bias occurring on the small models. Since $tol = 5\%$ is appropriate for δ_{err} , it can determine the volume of RVE well. While for $M_{\zeta_{iso}\delta_{err}}$, although it determines the RVE quickly, i.e. with only 2 realizations, the errors are large between the obtained effective elastic moduli ($\overline{k^{hom}} = 359.23$ MPa and $\overline{\mu^{hom}} = 111.23$ MPa) and the convergent results ($\overline{k^{hom}} = 384.45$ MPa and $\overline{\mu^{hom}} = 113.41$ MPa). Hence the combination method $M_{\zeta_{con}\delta_{err}}$ seems to be the most appropriate method for the foam models.

3. Effective elastic properties of periodic irregular open-cell foams

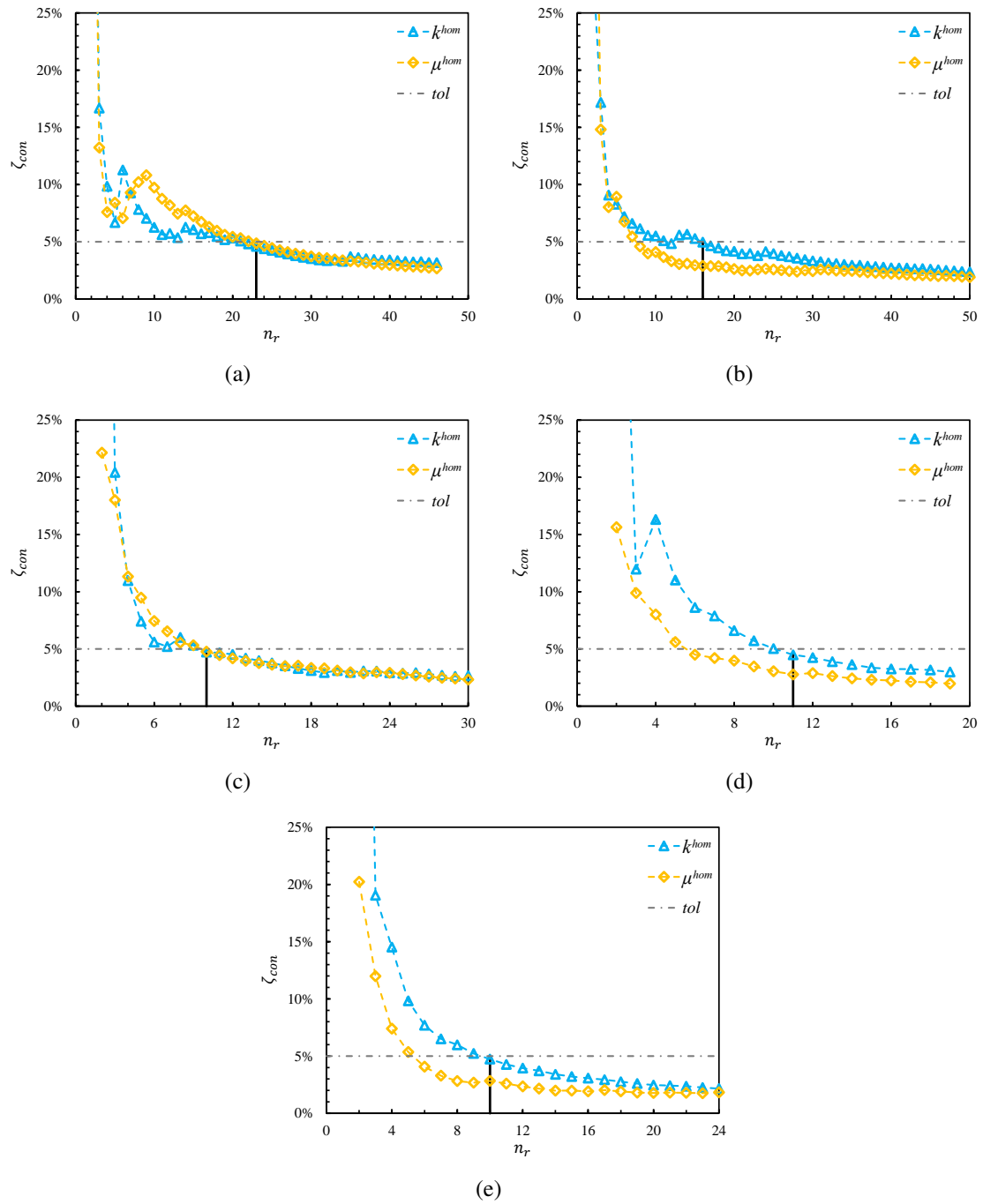
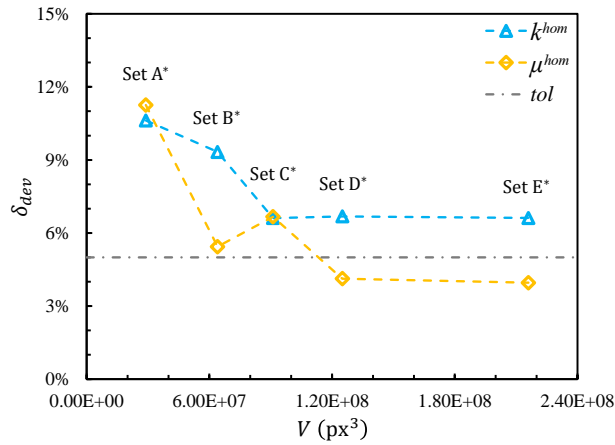
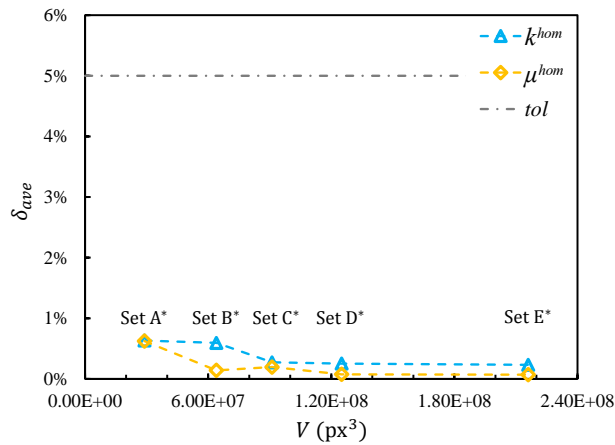


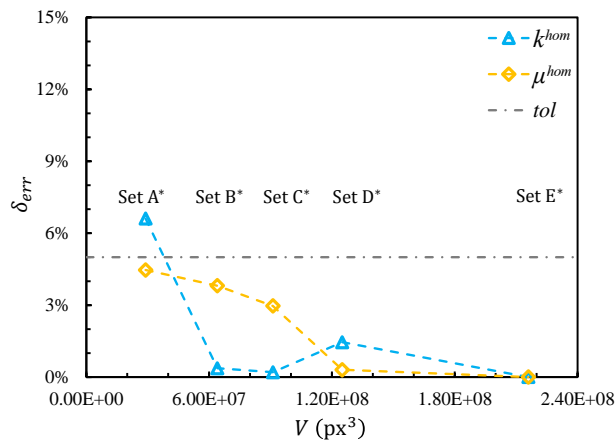
FIGURE 3.9: Evolution of ζ_{con} as a function of the number of realizations for (a) Set A* ; (b) Set B* ; (c) Set C* ; (d) Set D* and (e) Set E*.



(a)



(b)



(c)

FIGURE 3.10: Evolution of (a) δ_{dev} , (b) δ_{ave} and (c) δ_{err} as a function of the RVE volume.

TABLE 3.6: Number of realization n_r and RVE set determined by each method (M) with $tol = 5\%$ for all criteria except $\zeta_{iso} \leq 1\%$.

	$M_{\zeta_{con}\delta_{dev}}$	$M_{\zeta_{con}\delta_{ave}}$	$M_{\zeta_{con}\delta_{err}}$	$M_{\zeta_{iso}\delta_{dev}}$	$M_{\zeta_{iso}\delta_{ave}}$	$M_{\zeta_{iso}\delta_{err}}$
n_r	-	23	16	-	5	2
Set	-	Set A*	Set B*	-	Set C*	Set E*

5.4 New suggestions of the determination of the RVE

The evaluations of the RVE parameters, i.e. the number of realizations and the RVE volume are two essential steps in order to determine the RVE. Since $M_{\zeta_{con}\delta_{err}}$ is the most appropriate method for the foam models, several criteria are proposed to compare with the two criteria used in $M_{\zeta_{con}\delta_{err}}$, i.e. ζ_{con} and δ_{err} .

5.4.1 Determination of the number of realizations

The comparison is performed on Set B* (since determined by $M_{\zeta_{con}\delta_{err}}$) to show the accuracy and efficiency in determining the number of realizations among :

- *Confidence criterion* : The confidence criterion ζ_{con} is carried out with $tol = 5\%$.
- *Kanit's relation* : Assume that Kanit's relation (EQ. 3.14) is a criterion of number of realizations ζ_{Kanit} , and the relative error is also set as $\epsilon_{rela} = 5\%$. Following this criterion, the needed number of realizations is given by EQ. 3.14.
- *Convergence criterion [DÜS 12]* : As mentioned in Section 5.5 in Chapter 2, the convergence of the realizations is determined by computing the difference of the mean effective elastic stiffness matrix between two consecutive realizations :

$$\zeta_{conv} = \frac{\left\| [\overline{\mathbb{C}^{hom}}]_{n_r} - [\overline{\mathbb{C}^{hom}}]_{n_r-1} \right\|_{Frob}}{\left\| [\overline{\mathbb{C}^{hom}}]_{n_r-1} \right\|_{Frob}} \leq 3 \times 10^{-3}.$$

Table 3.7 shows the needed number of realizations and the mean effective elastic moduli evaluated by different criteria for Set B*. The numbers of realizations found by three criteria are close and all of them are small (less than 17). The obtained mean effective elastic moduli are similar as well. The same results can be found on the other four sets. Hence all three criteria are consider to evaluate the effective elastic properties of the foam models efficiently and accurately.

5.4.2 Determination of the volume of RVE

The comparison of the errors of k^{hom} is conducted with the RVE volume and the number of realizations determined by ζ_{con} (23, 16, 10, 11 and 10 for Set A*, Set B*, Set

TABLE 3.7: The comparison of the required numbers of realizations and the obtained properties for Set B*.

	n_r	$\overline{k^{\text{hom}}}$ (MPa)	$\overline{\mu^{\text{hom}}}$ (MPa)
ζ_{con}	16	380.73	118.65
ζ_{Kanit}	13	386.95	118.35
ζ_{conv}	15	381.94	118.10

C*, Set D* and Set E*, respectively). The errors are determined by the following criteria of RVE volume :

- *Effective property error* : As previously introduced, it corresponds to EQ. 3.22.
- *Kanit's relation* : Kanit's relation is always used to determine the number of realizations with a fixed volume or determine the volume with the fixed number of realizations for a given error. Since the volumes of the five sets are fixed and the numbers of realizations are determined as well, it can be used as a criterion to evaluate the relative error by considering :

$$\delta_{Kanit} = \frac{2k^b}{\overline{k^{\text{hom}}}} \sqrt{\frac{\rho^{\text{hom}}}{n_r \rho^b} \left(1 - \frac{\rho^{\text{hom}}}{\rho^b}\right) \left(\frac{\mathcal{A}^3}{V}\right)^\alpha} \leq 5\%. \quad (3.24)$$

- *Convergence criterion (new)* : The effective property error δ_{err} is proven to be a good criterion. However if the number of realizations is few, the results of the largest volume are not very credible. The convergence criterion δ_{conv} , which is similar as EQ. 3.8 and EQ. 2.33, is then proposed. The difference of $\overline{k^{\text{hom}}}$ between two consecutive volume sizes is calculated as :

$$\delta_{conv} = \frac{|\overline{k_{S_{i+1}}^{\text{hom}}} - \overline{k_{S_i}^{\text{hom}}}|}{\overline{k_{S_i}^{\text{hom}}}} \leq 5\%, \quad (3.25)$$

where S_{i+1} and S_i stand for the two consecutive sets.

Table 3.8 reports the comparison of the errors determined by different criteria for k^{hom} . For Set A*, all three errors are larger than 5%, which means all the criteria can avoid the very small RVE like Set A*.

5.4.3 Synthesis on the determination

After the above discussion, one can see that in our case, ζ_{con} , ζ_{Kanit} and ζ_{conv} are efficient and accurate criteria in determining the number of realizations, and δ_{err} , δ_{Kanit} and

TABLE 3.8: The comparison of the errors for k^{hom} combined with the set (volume) and the number of realizations determined by ζ_{con} (23, 16, 10, 11 and 10 for each set, respectively).

	Set A*	Set B*	Set C*	Set D*	Set E*
δ_{err}	6.61%	0.37%	0.20%	1.45%	-
δ_{Kanit}	5.33%	4.38%	4.68%	3.83%	3.10%
δ_{conv}	6.54%	0.17%	1.25%	1.47%	-

δ_{conv} can evaluate the volume of RVE well. Hence for the foam models, the RVE determination methods combined these criteria are proposed as : $M_{\zeta_{\text{con}}\delta_{\text{err}}}$, $M_{\zeta_{\text{con}}\delta_{\text{Kanit}}}$, $M_{\zeta_{\text{con}}\delta_{\text{conv}}}$, $M_{\zeta_{\text{Kanit}}\delta_{\text{err}}}$, $M_{\zeta_{\text{Kanit}}\delta_{\text{conv}}}$, $M_{\zeta_{\text{conv}}\delta_{\text{err}}}$, $M_{\zeta_{\text{conv}}\delta_{\text{Kanit}}}$ and $M_{\zeta_{\text{conv}}\delta_{\text{conv}}}$. The determination of RVE follows the algorithm in Section 3.2.3 and the obtained RVEs are listed in Table 3.9. The RVEs found by the proposed methods are similar and seem reasonable.

TABLE 3.9: The RVE parameters determined by the proposed methods for the foam models.

	n_r	Set
$M_{\zeta_{\text{con}}\delta_{\text{err}}}$	16	Set B*
$M_{\zeta_{\text{con}}\delta_{\text{Kanit}}}$	16	Set B*
$M_{\zeta_{\text{con}}\delta_{\text{conv}}}$	16	Set B*
$M_{\zeta_{\text{Kanit}}\delta_{\text{err}}}$	13	Set B*
$M_{\zeta_{\text{Kanit}}\delta_{\text{conv}}}$	13	Set B*
$M_{\zeta_{\text{conv}}\delta_{\text{err}}}$	15	Set B*
$M_{\zeta_{\text{conv}}\delta_{\text{Kanit}}}$	15	Set B*
$M_{\zeta_{\text{conv}}\delta_{\text{conv}}}$	15	Set B*

6 Conclusion

This chapter focuses on the study of effective elastic properties of irregular open-cell foams. The main conclusions are :

1. The morphological description of the real irregular open-cell sample are obtained by analyzing the reconstructed tomography structure. It allows to generated realistic periodic irregular open-cell structures which have the same morphological parameters as the real sample. Hill's lemma computational homogenization approach is still used to predict the effective elastic properties. The low computational cost is very useful for the study of irregular models which needs numerous realizations.

2. Two RVE determination approaches are performed to estimate the accurate effective elastic properties of irregular open-cell models. From the results, one can see that both RVE parameters, i.e. the number of realizations and the RVE volume, should be evaluated using the appropriate criteria for the determination of RVE. Kanit's analytic model could reflect the relation between the number of realizations and the RVE volume well. The obtained parameters \mathcal{A}^3 and α changes with the variance of the relative density. The required number of realizations increases when the relative density of foam models decrease. The results shows that the required number of realizations is not large even for the models with small volume. Hence choosing relatively smaller models with a sufficient number of realizations seems to be a better strategy. Moussaddy's algorithm helps to intuitively understand the variation tendency of each elastic modulus with both two RVE parameters. While not all criteria are appropriate for foam models. The effective elastic properties of the foam models can be evaluated accurately and efficiently by both approaches. Specific methods for foam models are proposed for the determination of the RVE.

Chapter 4

Effective elastic properties of periodic irregular closed-cell foams

After studying the open-cell foams, we will deal with the closed-cell foams in this chapter. The effective elastic properties of irregular closed-cell foams are still predicted with the Hill's lemma computational periodic homogenization approach. With the morphological parameters obtained by analysing the tomography images, the numerical structures are generated by the Voronoi-based approach. The influences of the kinematic modelings, the RVE parameters and the relative density on the effective elastic properties are studied. The comparison of the energy density is performed between the homogenized model and the tomography reconstruction model. The satisfying agreement between the homogenized results and the experimental results are observed.

Contents

1	Introduction	83
2	Modeling of irregular closed-cell structure	83
2.1	Material and its properties	83
2.2	Morphological description	85
2.3	Generations of numerical models	86
3	Results and discussion	90
3.1	Influence of kinematic modeling	90
3.2	Influence of RVE parameters	91
3.3	Influence of relative density	92
3.4	Comparison with tomography model	94
3.5	Comparison with experimental results	100
4	Conclusion	102

1 Introduction

The mechanical properties of closed-cell foams have been investigated widely recently. The tension-tension and compression-compression cyclic properties have been measured in [HAR 99] to show the fatigue failure mechanism of the closed-cell aluminium alloy foam. [SON 10, LI 14b] contribute to the understanding of the dynamic crushing responses of 3D closed-cell foams based on Voronoi random model. The influences of the cell shape irregularity, relative density, inertia of cell walls, strain hardening and impact loading on the plateau stress and the deformation model have been studied. The influence of the relative density and irregularity of Voronoi closed-cell foam models on the elastic and plastic properties are reported in [BAR 14a]. A multiaxial “plasticity” criterion of the simulation of the macroscopic behavior of light closed-cell foams is developed in [YE 15]. For us, we focus more on the elastic behavior of closed-cell foam. In [ROB 01], different isotropic random closed-cell foam models based on Voronoi tessellations and level-cut Gaussian random fields are generated and the density and microstructure dependence of the Young’s modulus and Poisson’s ratio have been computed. The results can be described by a power law $E \propto \rho^n (1 < n < 2)$ for the closed-cell cellular materials. [GRE 00] studies the influence of non-uniform cell wall thickness on elastic stiffness of Kelvin closed-cell structure. It shows that the stiffness of closed-cell cellular solids is not sensitive to the variations of the wall thickness. The similar investigation of cell wall thickness variation is reported by [CHE 15], and the effect of cell size variation on the stiffness of closed-cell structure foams using Laguerre tessellation models has also been studied. [MIR 16] focuses on the influence of internal pores distribution on the elastic properties of closed-cell aluminium foam by conducting monotonic compression test. [PAB 18] carried out numerical calculations of relative Young’s modulus on computer-generated Kelvin and random microstructures of closed-cell cellular materials and inverse foams. The numerical results are compared to several analytical models.

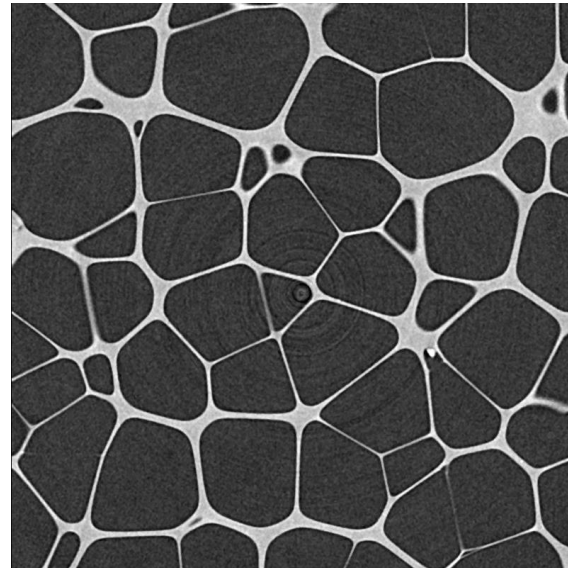
In this chapter, the tomography slices of the irregular closed-cell sample are analysed to obtain the dispersion of cell size distribution and the anisotropy. With the morphological description, numerical irregular closed-cell structures are generated by the recent approach based on Voronoi diagram. The Hill’s lemma computational homogenization approach is used to predict the effective elastic properties of irregular closed-cell foam models. The influence of the RVE parameters, the kinematic modelings and the relative density are analyzed. The homogenized results are compared with the results of the tomography reconstruction model and the experimental results.

2 Modeling of irregular closed-cell structure

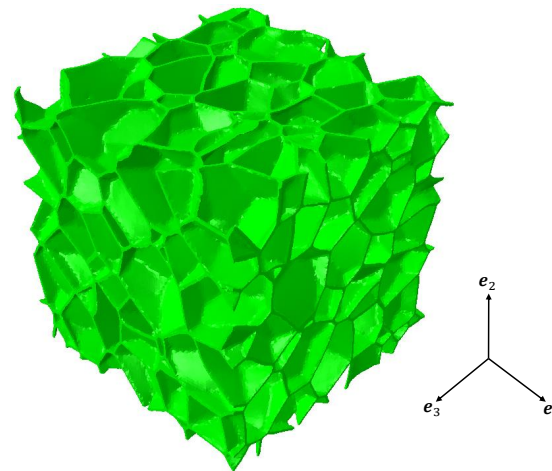
2.1 Material and its properties

The material used in this chapter is a modified Polyvinylchloride (PVC) cross-linked cellular foam made by AIREX[®]. The nominal density is 200 kg/m³, referred as C70.200. A typical tomography slice of the irregular closed-cell foam and the structure obtained by

micro-computed tomography are shown in FIG. 4.1. The resolution of the sample are 3 μm per voxel.



(a)



(b)

FIGURE 4.1: Tomographic data of the irregular closed-cell structure : (a) a tomography slice ($400 \times 400 \text{ px}^2$); (b) 3D rendering after reconstruction.

Due to different production processes, the properties of PVC could be very different. In [ASH 05], the Young's modulus of PVC is 2140-4140 MPa and the density is 1300-1580 kg/m^3 . In the following studies, the relative density of the foam is set as 15% first, and its influence on the effective elastic properties will be estimated in the certain range in Section 3.3. The Young's modulus and the Poisson's ratio of PVC are set as 4000 MPa and 0.33, respectively [ASH 05, YE 15].

2.2 Morphological description

Three morphological parameters will be considered when generating realistic numerical irregular closed-cell structures : 1. the relative density $\rho^{\text{hom}}/\rho^{\text{b}}$; 2. the coefficient of variation C_V , which represents the dispersion of cell size distribution ; 3. the anisotropy of the structure. The last two parameters are introduced in detail in the following sections.

2.2.1 Dispersion of cell size distribution

The volume of each cell can be measured directly by the software iMorph [BRU 08]. Considering the cells equivalent to the spheres, the distribution of the normalized cell diameters (by the average diameter) exhibits a Gaussian unimodal shape (shown in Section 2.3). By analysing σ_{d_c} and $\overline{d_c}$, the coefficient of variation C_V can be estimated as 0.136. It should be noticed that the analysis of the dispersion of cell size distribution is performed on fully contained cells.

2.2.2 Anisotropy

Due to performance needs or other reasons, sometimes foams can exhibit anisotropic behavior. Same investigation of covariance functions is performed on the tomography slices of the closed-cell sample to verify if the microstructure is isotropic or not. FIG. 4.2 shows the covariance of the microstructure of the irregular closed-cell foam in the orthogonal coordinate system (e_1, e_2, e_3) . From the figure, the microstructure seems to be isotropic since the covariance functions are similar along three directions. While numerous blurs are observed when analysing the tomography slices. FIG. 4.3 is a typical slice which have several blurs marked in red arrows or circle. These blurs may be caused by beam hardening in reconstruction and can lead to errors because they are also considered as solid parts when studying the covariance functions. This is also why the relative density obtained in FIG. 4.2, i.e. 21.44%, is much larger than that analyzed in Section 2.1.

Another method is used to verify the isotropy, i.e. analysing the matrix of inertia [DIL 05]. Cells of the tomography structure are considered equivalent to ellipsoids and the anisotropy of the whole structure is quantified directly by the commercial FE package Abaqus 6.11-2 [Aba 11]. For simplicity, the matrix of inertia is normalized by the first component of the main diagonal, i.e.

$$[I_C^*] = \begin{bmatrix} 1.00 & \sim 0 & \sim 0 \\ \sim 0 & 1.01 & \sim 0 \\ \sim 0 & \sim 0 & 1.00 \end{bmatrix}.$$

The eigenvalues of this matrix are approximately equal.

Hence, the tomography structure is considered to be geometrically isotropic by both methods.

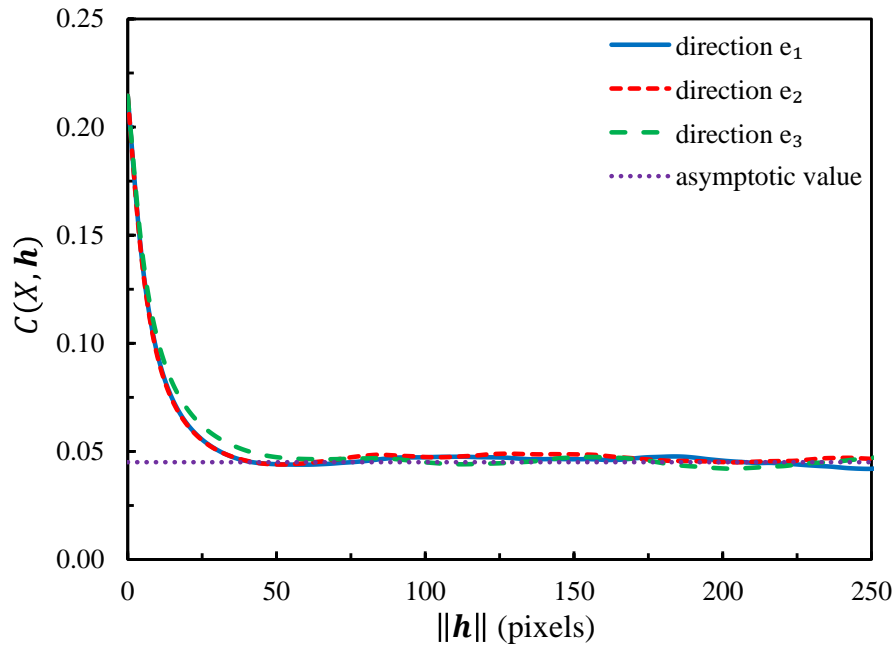


FIGURE 4.2: Covariance functions in three directions of solid phase of closed-cell sample microstructure.

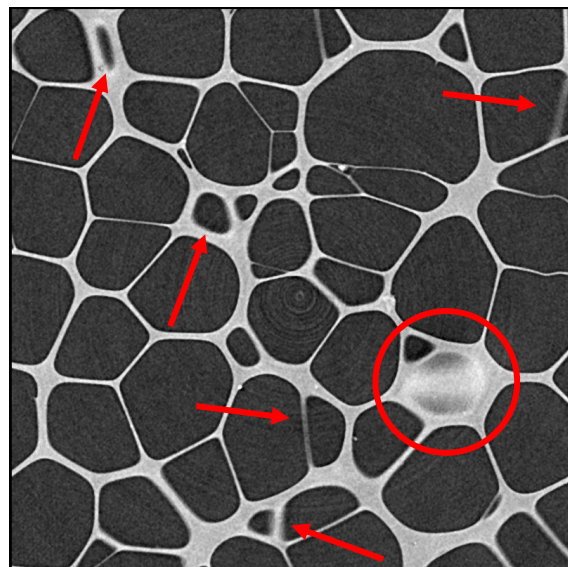


FIGURE 4.3: Illustration of the blurs in the tomography slice which leads to the error.

2.3 Generations of numerical models

The Voronoi-based approach, which has been used for open-cell structures before, is applied to numerically generate periodic irregular closed-cell structures. For closed-cell structures, the cells obtained by Surface Evolver will be “separated”, i.e. every face

is duplicated and each of the two copies is grouped with other connected faces, each group constituting the boundaries of one of the original cells. Each cell-group can then be assigned with a displacement vector. One can see in FIG. 4.4 that with an opportunely chosen set of displacement vectors, a wall with the chosen thickness between cells can be represented. For the full cell structure, the role of displacement vectors can be observed in FIG. 4.5. After that, the displaced cells are used to carve holes in a cubic bounding box thus resulting in the finalized constant thickness closed-cell structure.

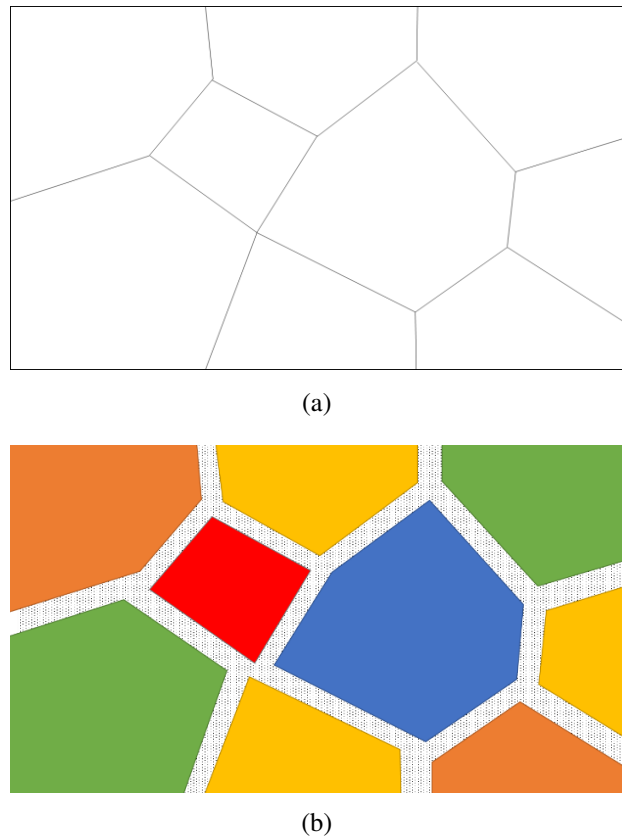


FIGURE 4.4: Original (a) and exploded (b) cell structure. Colors identify cells. Walls are pattern filled.

The cell size distribution of the tomography structure is plotted with the blue curve in FIG. 4.6. The numerical closed-cell structures are generated, trying to match coefficient of variation of the equivalent cell diameter distribution. The matching is realized by inputting the required quantity in the algorithm directly rather than by means of an iterative process. The distribution of the normalized cell diameters of the numerical structure, i.e. the red curve in the figure, makes a great consistency with the blue curve. Two curves have a shared area fraction of 93.47% quantitatively.

Like the previous chapter, in order to study the influence of the RVE parameters (the number of realizations and the RVE volume), five sets of numerical closed-cell structures with different volumes are generated. FIG. 4.7 and Table 4.1 show the illustration and the

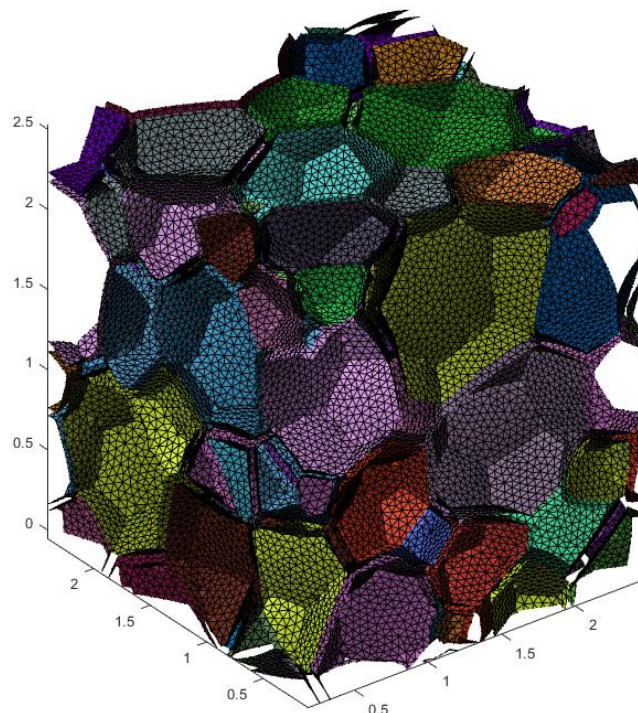


FIGURE 4.5: Full cell structure showing the space between cells (wall thickness) in 3D.

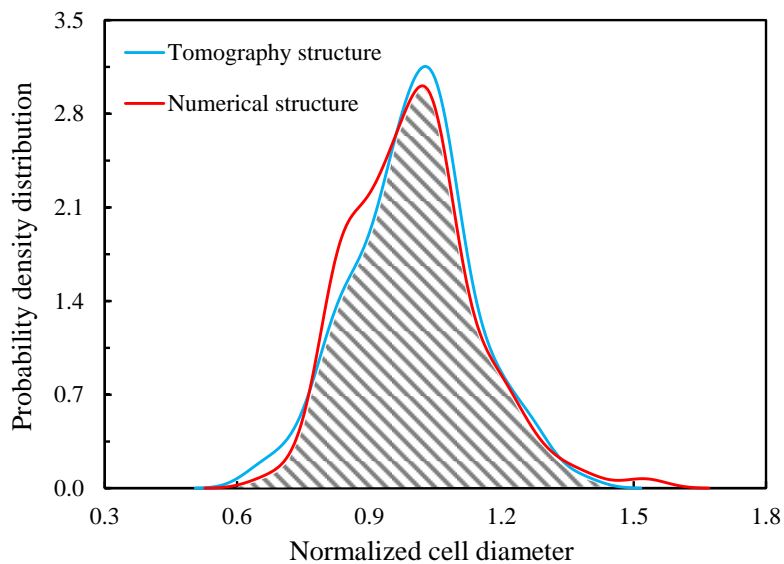


FIGURE 4.6: Normalized cell diameter distributions of the tomography structure and the numerical structure, as calculated by iMorph.

characterization of each set respectively. The ratio of the number of cells to the volume of models is kept constant, which is obtained by morphological analysis.

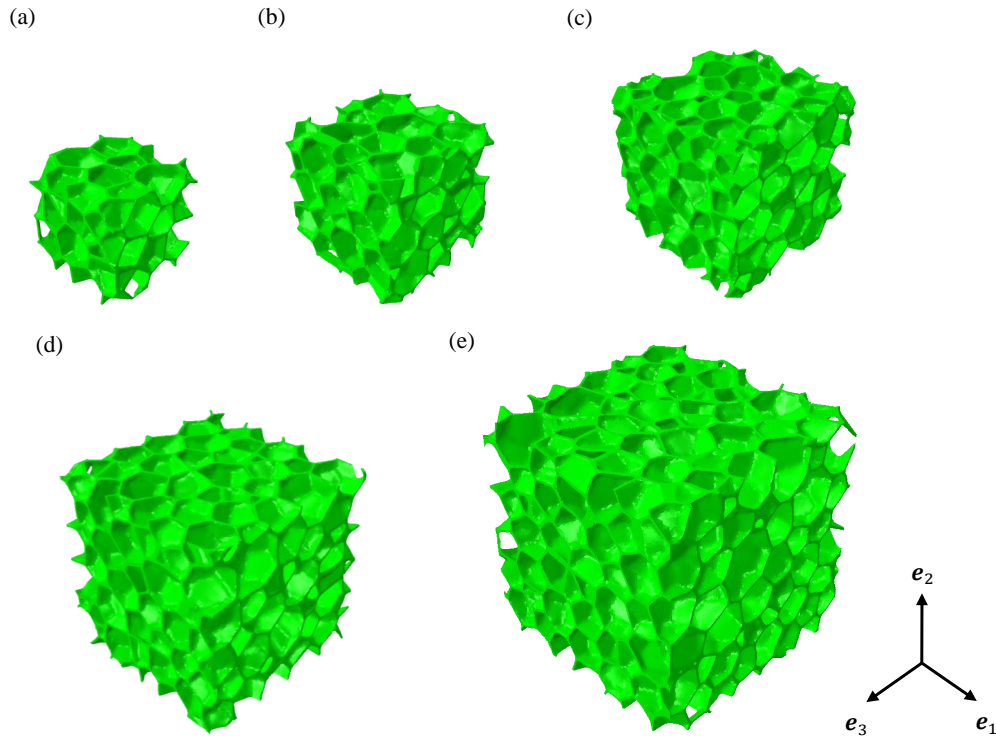


FIGURE 4.7: Illustration of numerical irregular closed-cell model for (a) Set A; (b) Set B; (c) Set C; (d) Set D and (e) Set E.

TABLE 4.1: Characterizations of each set of closed-cell structures.

	Domain dimensions (px^3)	Number of cells
Set A	$200 \times 200 \times 200$	30
Set B	$250 \times 250 \times 250$	58
Set C	$300 \times 300 \times 300$	100
Set D	$350 \times 350 \times 350$	159
Set E	$400 \times 400 \times 400$	238

3 Results and discussion

3.1 Influence of kinematic modeling

In addition to solid elements, shell elements are also used to mesh closed-cell foam models [CAT 08, BAR 14a, YE 15, CHE 15]. It is interesting to compare the elastic properties of solid model and shell model. In FIG. 4.8, the same models ($300 \times 300 \times 300 \text{ px}^3$ with 100 cells) are meshed with 304,341 3-node triangular general-purpose shell elements (FIG. 4.8(a)) and 891,823 linear tetrahedron solid elements (FIG. 4.8(b)). Unlike the model with solid elements, it is difficult to obtain the effective elastic stiffness matrix of the model with shell elements. Hence the tensile simulation and the shear simulation are carried out on both models by applying the displacements on one surface along different directions while “clamping” the opposite surface along the corresponding directions and testing the force (FIG. 4.9 shows 2D perspective for simplicity). The simulations are realized by the commercial FE package Abaqus 6.11-2 [Aba 11]. The periodic boundary condition is imposed on both models, and for the shell model, the periodicity of the rotation of the corresponding nodes is also considered. The thickness of the shell elements is uniform, and both models have the same relative density.

FIG. 4.10 and FIG. 4.11 show the deformations of both shell model (with 304,341 elements) and solid model (with 891,823 elements) after the certain displacement for the tensile test along direction 11 and the shear test along direction 12 respectively with *von Mises* equivalent stress map. From the figure, the deformations of two models are similar with similar *von Mises* equivalent stresses in general, whether for the tensile simulation or the shear simulation. The difference may be caused by the different kinematic models (will be analyzed in the following paragraphs), small structural differences and the different numbers of elements.

Tensile responses and shear responses along direction 11 and direction 12 respectively of two models are compared in FIG. 4.12. The simulation results are the convergent values of the data with different number of elements for both models. One can see from the figure that whether for the tension or the shear, the solid model is stiffer than shell model. The relative errors are 12.77% for the tension and 13.37% for the shear.

The similar results can be observed in [STO 13b] that the differences in the effective elastic properties are over 10% between solid open-cell foam models and beam open-cell foam models. The underestimation of the stiffness for the beam model has been considered and the reasons has been analyzed as [STO 13b] :

- the moment of inertia at the nodes is much larger for solid models than beam models;
- the free bending length of the struts decrease for solid models.

Shell model is the same as beam model that neglects the material concentration since the elements are connected at the middle of the elements and the bodies of the elements don not interact with each other.

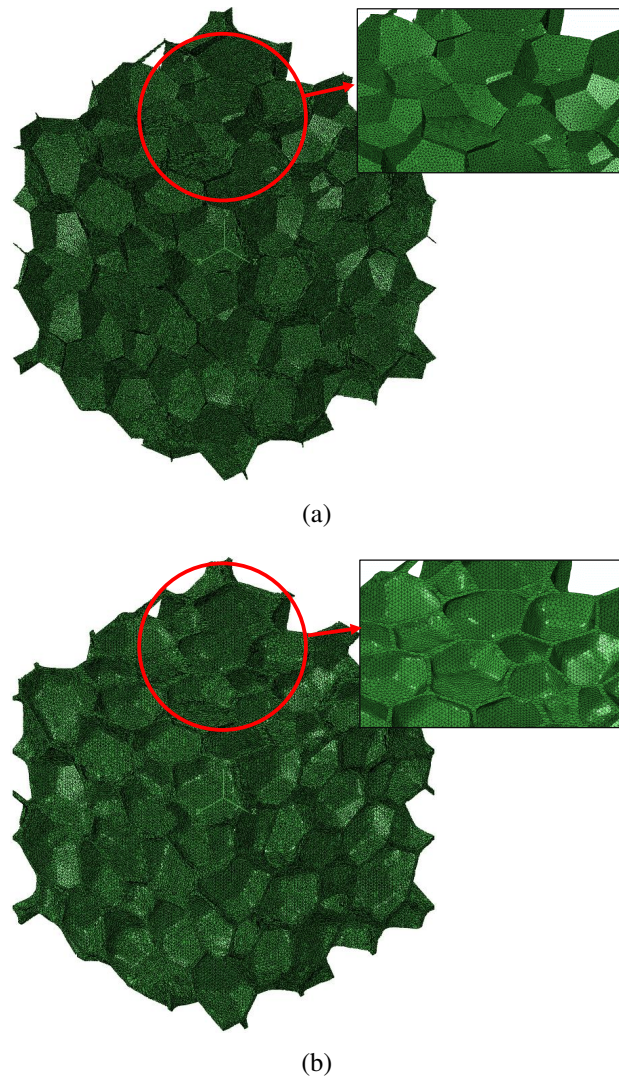


FIGURE 4.8: An original overall isotropic model is mesh with (a) 304,341 shell elements and (b) 891,823 solid elements, respectively.

3.2 Influence of RVE parameters

Stochastic realizations are performed as well to take into account the microstructure irregularities of the studied closed-cell foams. For Set D, the overall effective elastic stiffness matrix after 5 realizations in the frame (e_1, e_2, e_3) is :

$$\overline{[C]^{hom}} = \begin{bmatrix} 340.51 & 153.47 & 152.84 & \sim 0 & \sim 0 & \sim 0 \\ & 342.91 & 153.08 & \sim 0 & \sim 0 & \sim 0 \\ & & 341.62 & \sim 0 & \sim 0 & \sim 0 \\ & Sym & & 188.02 & \sim 0 & \sim 0 \\ & & & & 186.56 & \sim 0 \\ & & & & & 187.24 \end{bmatrix} \text{ (MPa)}.$$

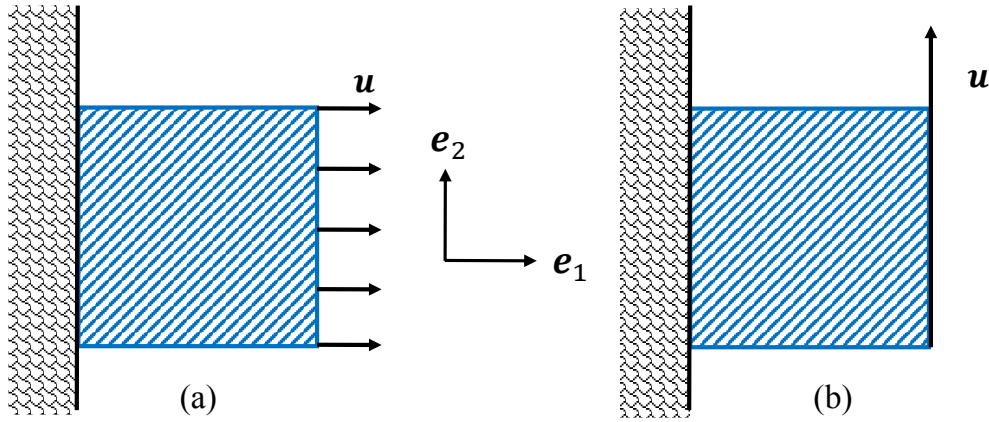


FIGURE 4.9: Illustration of (a) tensile simulation and (b) shear simulation in a 2D perspective.

The isotropy criterion ζ_{iso} of the overall effective matrix after 5 realizations is deduced as $\zeta_{iso} = 0.28\%$. It indicates that the homogenized behavior can be assumed isotropic. Hence the effective elastic stiffness tensor can be equivalently written as :

$$\overline{\mathbb{C}}^{\text{hom}} = 3\overline{k}^{\text{hom}}\mathbb{J} + 2\overline{\mu}^{\text{hom}}\mathbb{K},$$

with the overall effective bulk modulus $\overline{k}^{\text{hom}} = 215.98$ MPa and the overall effective shear modulus $\overline{\mu}^{\text{hom}} = 93.89$ MPa. Due to the isotropic property, one just needs to focus on k^{hom} and μ^{hom} in the following studies.

The influence of the number of realizations n_r on the effective elastic properties of the closed-cell foams is estimated first. FIG. 4.13 shows the evolutions of the mean effective elastic moduli with the increase of the number of realizations for Set A. One can see even for the smallest models, the variances of both moduli are negligible with a very few realizations. Same tendency can be observed on the other sets. Comparing to the open-cell foams studied in the previous chapter, the variance of the closed-cell foam studied in this chapter is much smaller, which makes the determination of RVE in the previous chapter meaningless for the closed-cell foams.

The evolutions of $\overline{k}^{\text{hom}}$ and $\overline{\mu}^{\text{hom}}$ with the increase of the volume of RVE is given in FIG. 4.14. All data are the convergence values. In the figure, one can see for each effective elastic modulus, the difference among all 5 sets are very small. No bias caused by boundary effects is observed on these models. Since any set can represent this series of numerical models, define that the results of Set B are used in the following studies.

3.3 Influence of relative density

The influences of the relative density is studied in this section. As said in Section 2.1, according to [ASH 05], the density of PVC bulk varies from 1300 kg/m^3 to 1580

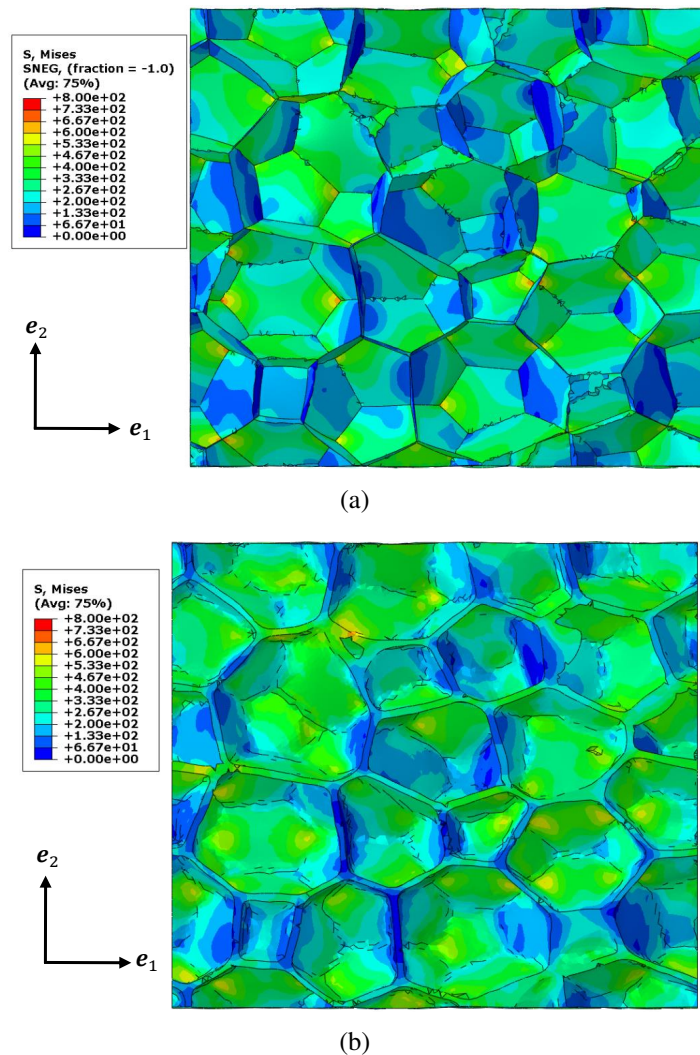


FIGURE 4.10: Deformations of (a) shell model and (b) solid model for the tensile test along direction 11 with *von Mises* equivalent stress map.

kg/m^3 , which makes the corresponding relative density vary from 12.66% to 15.38% given that the foam density equals to 200 kg/m^3 . Hence different models are generated as Set B except with different relative densities (12.7%, 13.7%, 14.6% and 15.3%). Since the numerical models have been proven to be very stable in Section 3.2, for each relative density, four realizations are estimated and the mean results are used to show the influence. The evolutions of the effective elastic moduli with the relative density are presented in FIG. 4.15. It may be a non-linear evolution for a large range of the relative density, however in this case, the evolution can be considered linear in the current small range .

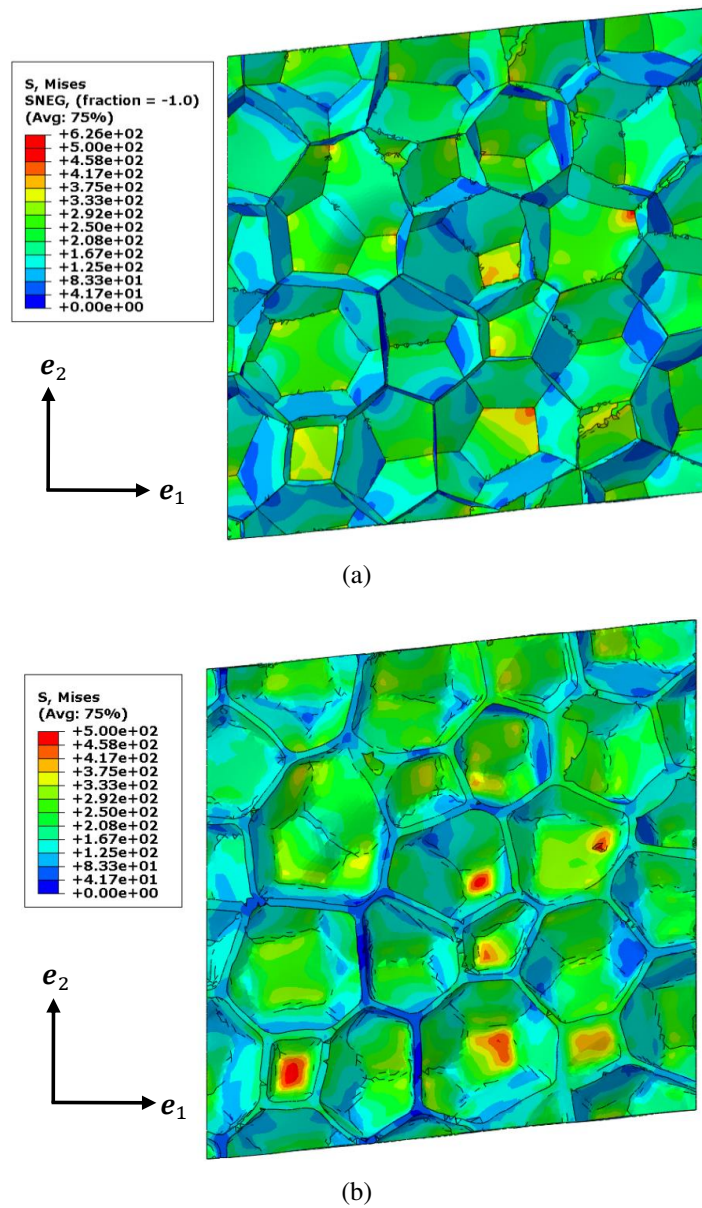


FIGURE 4.11: Deformations of (a) shell model and (b) solid model for the shear test along direction 12 with *von Mises* equivalent stress map.

3.4 Comparison with tomography model

The comparison of the effective elastic properties between the tomography model (FIG. 4.1(b)) and the homogenized model is performed in this section. The relative density of the tomography model is set as 15%. The kinematic boundary conditions are imposed on the tomography model instead of the periodic boundary condition, since the structure is non-periodic. As introduced before, the tensile simulation and the shear simulation are carried out on models by applying the displacements on one surface along different

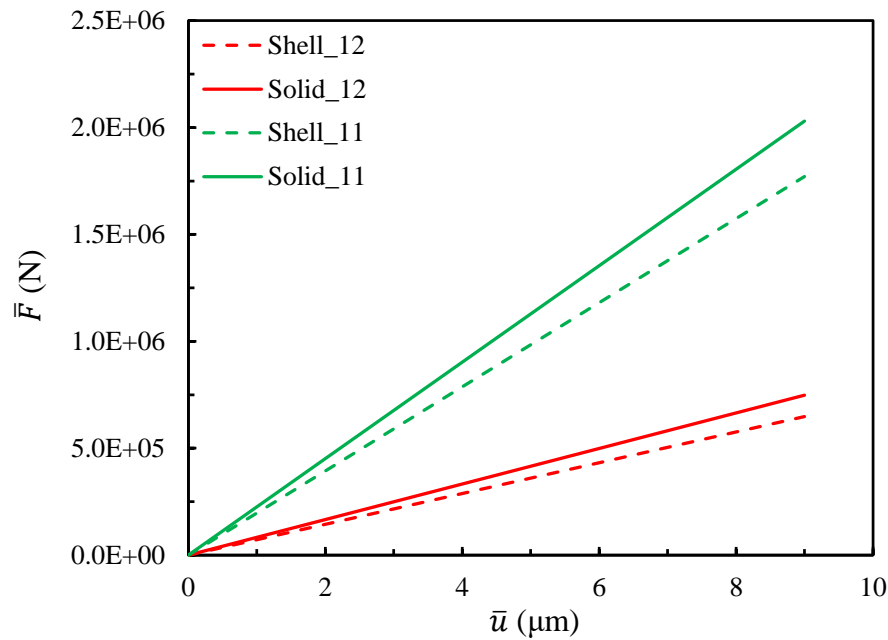


FIGURE 4.12: Comparison of the tensile response and the shear response between shell model and solid model.

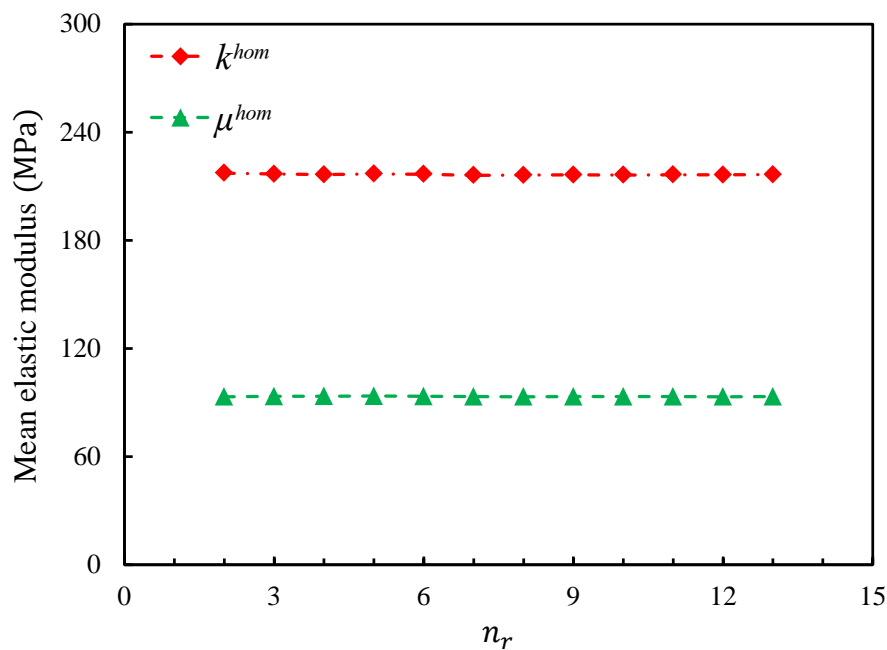


FIGURE 4.13: Evolutions of $\overline{k}^{\text{hom}}$ and $\overline{\mu}^{\text{hom}}$ as a function of the number of realizations for Set A.

directions while “clamping” the opposite surface along the corresponding directions. The tomography model is meshed with 654,303, 969,394 and 1,596,850 linear tetrahedron

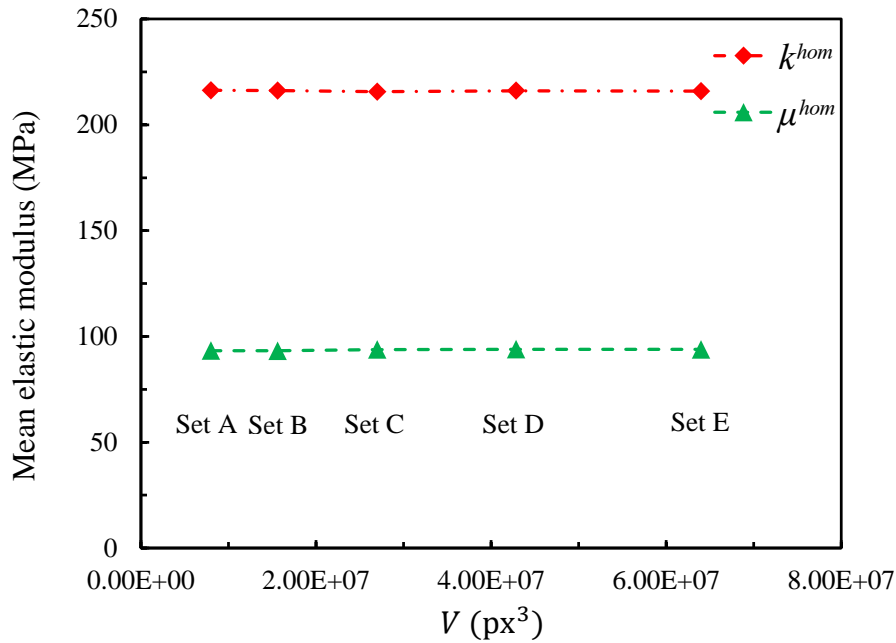


FIGURE 4.14: Evolution of $\overline{k^{hom}}$ and $\overline{\mu^{hom}}$ as a function of the RVE volume.

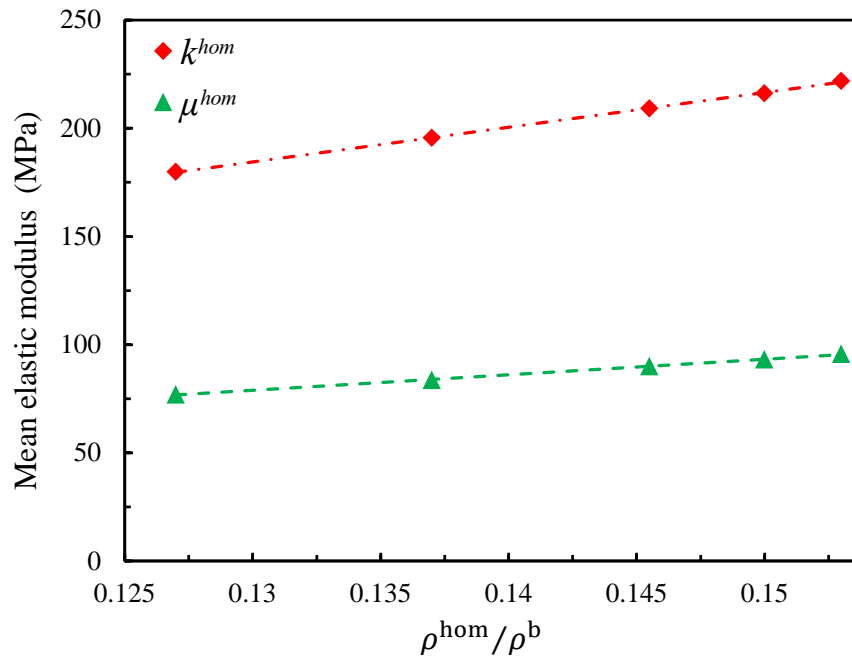


FIGURE 4.15: Effect of the relative density on the effective elastic moduli.

solid elements respectively and the convergence values are used to compare as well. The finite element simulations are realized by Abaqus. FIG. 4.16 shows the deformations of the tomography (with 1,596,850 elements) after the certain displacement for the tensile

test and the shear test respectively with *von Mises* equivalent stress map.

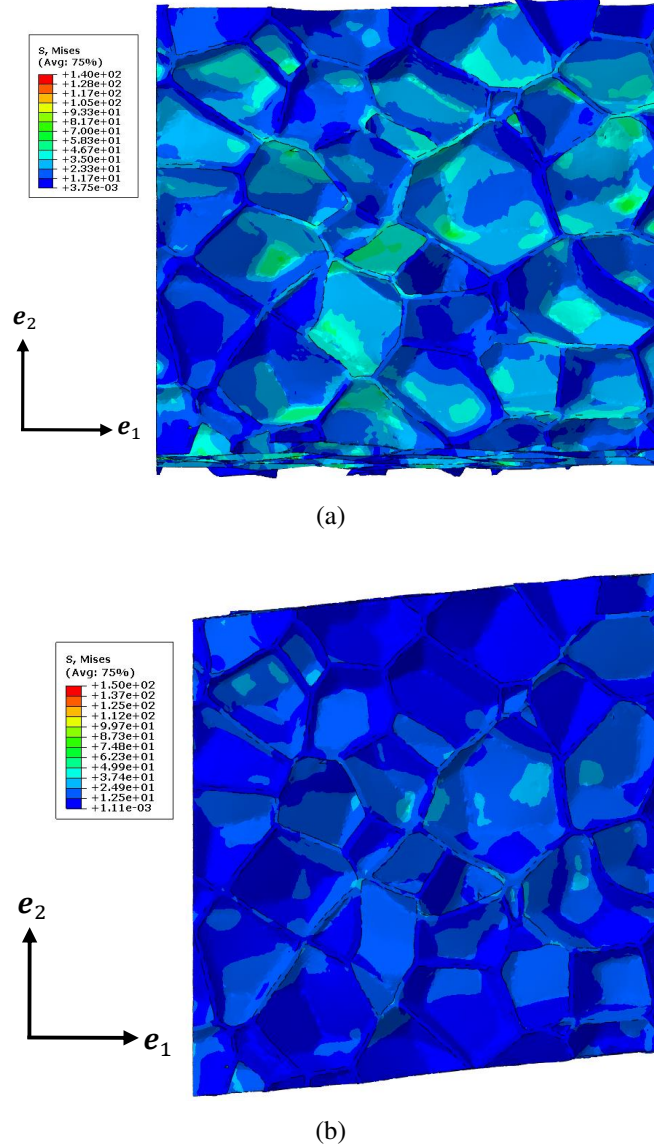


FIGURE 4.16: Deformations of the tomography model for (a) the tensile test and (a) the shear test with *von Mises* equivalent stress map.

The overall macroscopic energy $\langle \Psi \rangle = \left\langle \frac{1}{2} \boldsymbol{\sigma} : \boldsymbol{\epsilon} \right\rangle = \frac{1}{2} \bar{\boldsymbol{\sigma}} : \bar{\boldsymbol{\epsilon}}$ of the tomography model, which is obtained by Abaqus simulation, is compared to the homogenized derived behavior. Indeed, with Abaqus simulations, one can compute

$$\langle \Psi \rangle = \frac{1}{|\Omega|} \sum_{e=1}^{N_e} \Psi_e \quad (4.1)$$

and

$$\langle \boldsymbol{\sigma} \rangle = \frac{1}{|\Omega|} \sum_{e=1}^{N_e} \boldsymbol{\sigma}_e, \quad (4.2)$$

where e means the element index and ψ_e is the element strain energy. On the other hand, the overall energy within the elastic RVE can be written for macroscopically isotropic media as :

$$\psi^{\text{hom}} = \frac{\bar{\sigma}_m^2}{2k^{\text{hom}}} + \frac{\bar{\sigma}_{eq}^2}{6\mu^{\text{hom}}} \quad (4.3)$$

where $\bar{\sigma}_m$ (resp. $\bar{\sigma}_{eq}$) corresponds to the macroscopic hydrostatic (resp. equivalent) stress obtained with Abaqus. According to the previous computations, k^{hom} and μ^{hom} for the homogenized model are 216.14 MPa and 93.21 MPa, respectively.

For uniaxial tension or shear without the periodic boundary condition, all other components of the average stress $\{\bar{\boldsymbol{\sigma}}\}$ can be considered 0 compared to $\bar{\sigma}_{ij}$. For example, for the two cases in FIG. 4.9, the average stresses are $^T\{\bar{\sigma}_{11}, 0, 0, 0, 0, 0\}$ and $^T\{0, 0, 0, 0, 0, \sqrt{2}\bar{\sigma}_{12}\}$. Hence the evolutions of the energy density with the overall macroscopic stress component $\bar{\sigma}_{ij}$ are compared between the tomography model (a real non-periodic microstructure) and the homogenized model (derived with the periodicity boundary condition assumptions) in FIG. 4.17. Besides, two numerically generated models are also tested under the kinematic boundary conditions, similarly to the tomography model. Both of them have the same size and statistical morphology description as the tomography model. While one is generated with geometrically periodic boundaries, and the other is generated with non-periodic boundaries. FIG. 4.17(a) shows the evolutions of the energy density with $\bar{\sigma}_{11}$ and FIG. 4.17(b) presents those with $\bar{\sigma}_{12}$. In the figures, the points are the simulation results of the real tomography model, named ‘‘Tomo’’, and the results of the simulations with the numerical generated microstructures models, named ‘‘Num-P’’ and ‘‘Num-NP’’ respectively. The corresponding results of the homogenized model are drawn with the solid lines, named ‘‘Hom’’.

From the figures, one can see whether for the tensile test or for the shear test, the tomography model has the responses similar to the numerical models with periodic boundaries or non-periodic boundaries. It turns out that the numerically generated models do not bias the the real tomography model. Furthermore, for the tensile test, the difference between the homogenized model and the tomography model is negligible. While for the shear test, the difference in energy density is much more significant. It seems that shear is more sensitive to the periodic boundary condition than tensile for the RVE with $V = 400 \times 400 \times 400$ px³.

From the results, the tomography model is not large enough to have correct results without the periodic boundary condition.

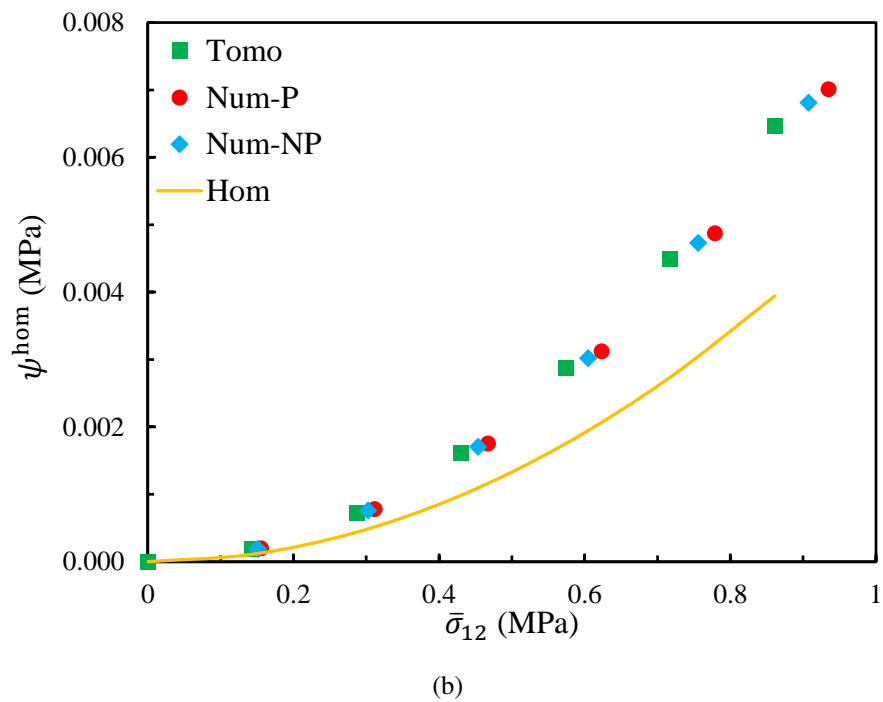
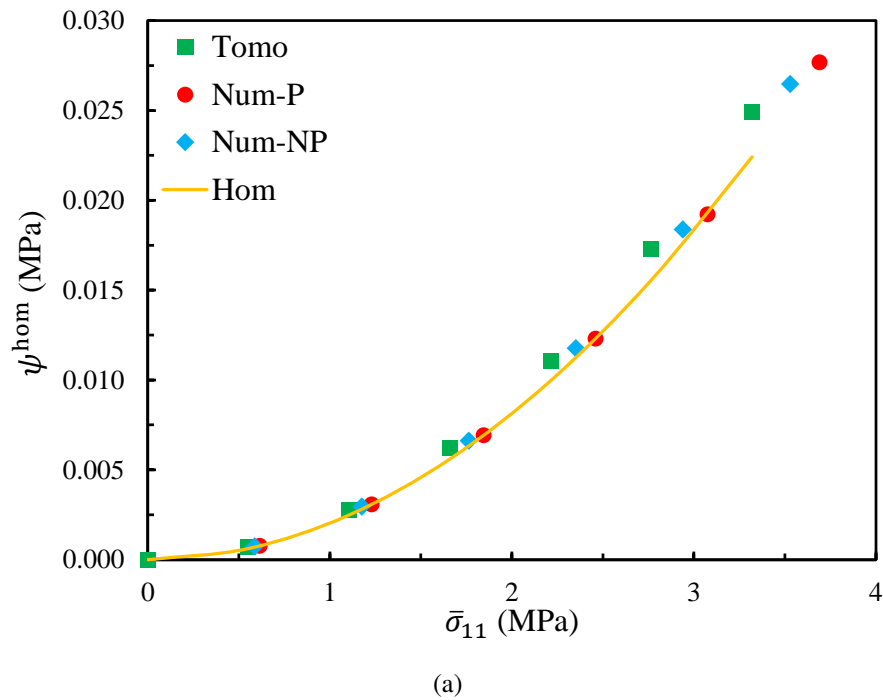


FIGURE 4.17: The evolution of the energy density as a function of (a) $\bar{\sigma}_{11}$ and (b) $\bar{\sigma}_{12}$ for each model.

3.5 Comparison with experimental results

Experiments are performed explicitly to obtain the macroscopic responses. The illustration of the specimens for different tests is shown in FIG. 4.18. The cubic specimen is prepared for the compression test, while the shear test is performed using the Arcan method [ARC 78, HUN 97, COG 11] with the “Batman” type specimen. It consists of two flanges in half-moon shape and is gripped in a loading frame with the load applied via the faces to avoid the potential problem of instability associated with edge loading and to obtain pure shear in the central part of the specimen. In the experiments, the local strain is measured by digital image correlation technique [CHU 85]. FIG. 4.19 is an example of the measurement of the strain field during the shear test using the software Icasoft [MGU 97].

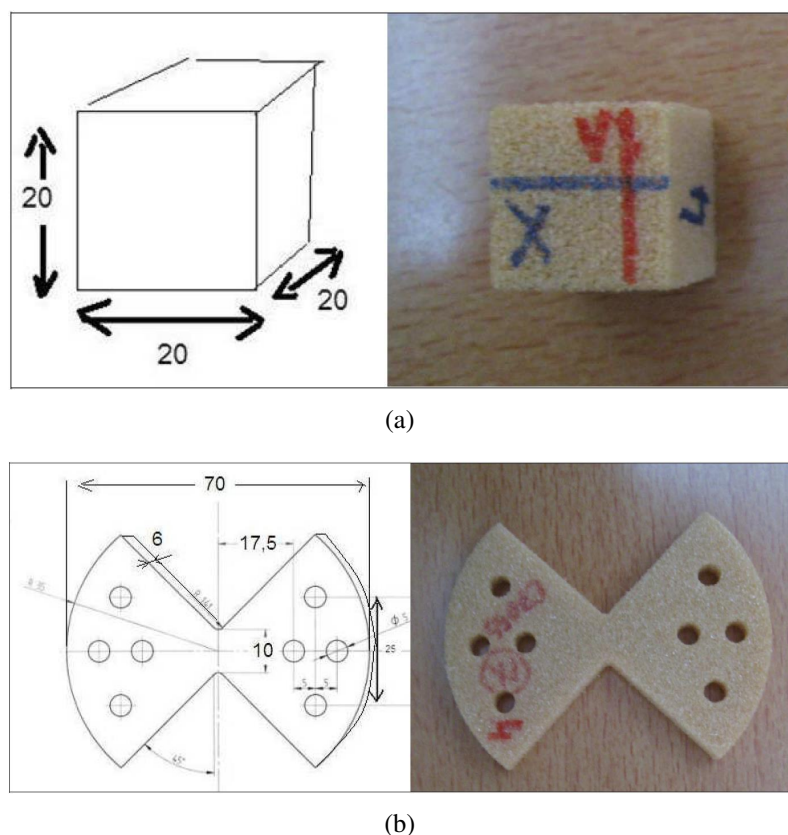


FIGURE 4.18: Illustration of (a) the cubic specimen for compression test and (b) the “Batman”-shaped specimen for shear test.

The macroscopic response curves are plotted in FIG. 4.20. Although these curves reflect the complete deformations, we focus on the elasticity in this study. Meanwhile, the corresponding effective elastic moduli of the homogenized model are drawn with the black lines in the figure. Since the density of the samples studied can not be obtained accurately, the bars here stand for the range of the effective elastic moduli caused by different relative densities in their certain range (12.66%-15.38%). Considering for the

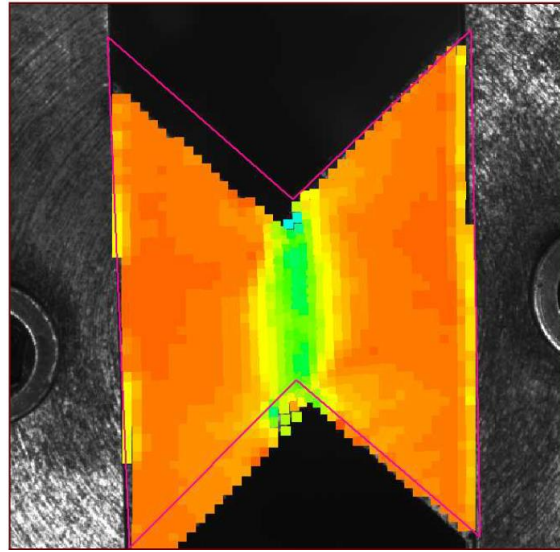


FIGURE 4.19: Illustration of the shear deformation of the ‘Batman’-shaped specimen.

experimental results, each elastic modulus is determined by measuring the slope of the beginning of the stress-strain curve, one can see the homogenized results have a good agreement with the experimental results.

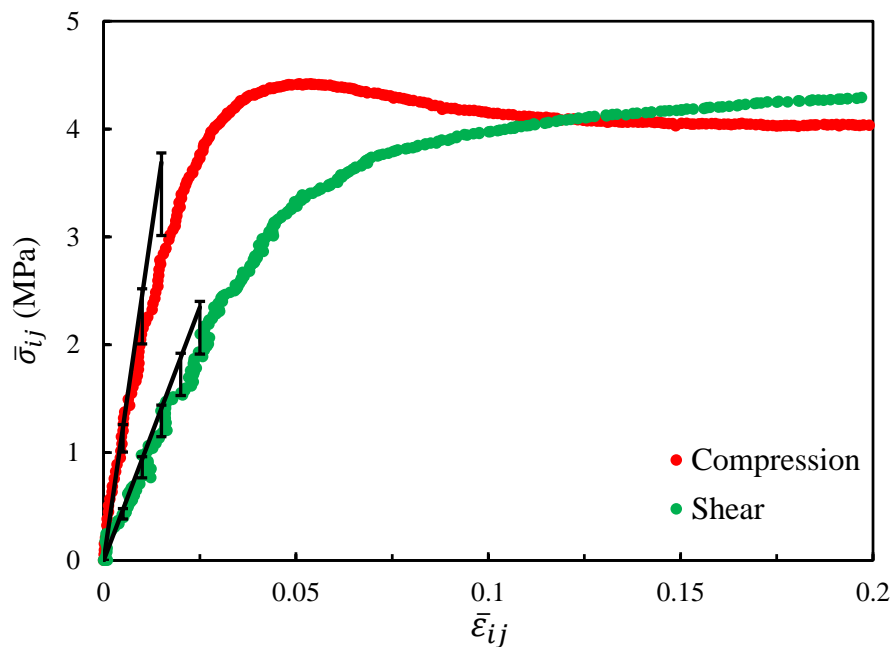


FIGURE 4.20: Stress-strain curves of the macroscopic compression and shear tests (the effective elastic moduli obtained by numerical simulations are drawn with the black lines).

4 Conclusion

In this chapter, the study of the effective elastic properties of the irregular closed-cell foams are performed. The main conclusions are following :

1. By analysing the tomography slices, the dispersion of cell size distribution and the anisotropy of the real irregular closed-cell foam are obtained. Using the approach based on Voronoi diagram, realistic periodic irregular closed-cell foam structures are numerically generated with the morphological parameters.
2. Hill's lemma computational homogenization approach is used to predict the effective elastic properties of the closed-cell foam models. The closed-cell foam models require only a small amount of realizations to reach convergence. The comparison between the same structure with different kinematic modelings is carried out. The model with solid elements is stiffer than that with shell elements. The influence of the relative density on the effective elastic moduli are studied. The approximately linear evolution is found in the small range. The energy density is investigated to compare the homogenized models with the tomography reconstruction model without the periodic boundary condition. It permits to point out that the tomography sample is not large enough to obtain the correct results. The homogenized results are compared with the experimental results, where a satisfying agreement is achieved.

General conclusions and prospects

Conclusions

In this thesis, the effective elastic properties of foams have been investigated. The main body of the work is based on numerical simulations, which are realized by the Hill's lemma periodic computational homogenization approach. In addition, the recent approach based on Voronoi diagram is used to generate a variety of foam structures, which are able to represent the details of the microstructure. The major achievements are highlighted below, followed with some prospects.

- I- A Hill's lemma based periodic computational homogenization approach (HL-FEM) is developed to predict the effective elastic properties numerically, which is strictly limited to linear elasticity with small perturbations at present. Comparing with usual approach, the current HL-FEM can obtain the complete effective elastic stiffness matrix with only one finite element calculation and without boundary loadings, such as macro-strains. The validation of HL-FEM is performed by usual method.
- II- The approach based on Voronoi diagram permits to generate numerical structures with a number of morphological parameters, i.e. the solid fraction, the cell size distribution and the anisotropy for both open-cell structures and closed-cell structures; the way the solid distributed in cell struts (characterized by the diameter ratio and the normalized curvature) for open-cell structures. It allows to study the influences of these morphological parameters and combine with the morphological analysis of the real foam samples.
- III- The effects of the morphological parameters on effective elastic properties of Kelvin open-cell foams are investigated. The relative density is proved to be the most influential parameter. The way the solid distributed in cell struts also has significant influence. There are obvious differences in the effective elastic properties between the regular Kelvin structures and irregular structures, while it seems that for irregular structures, changing the dispersion of cell size distribution in the certain range has no obvious influence.

- IV- RVE determination approaches are performed to obtain the accurate effective elastic properties of irregular open-cell models. Both RVE parameters (the number of realizations and the RVE volume) should be determined using appropriate criteria. With Kanit's analytic law, the relationship between the number of realizations and the RVE volume is estimated for irregular open-cell foams. The parameters of the law change with the variance of the relative density, and the required number of realization is larger for the models with smaller relative density. Moussaddy's algorithm reflects well the variation tendency of each elastic modulus with RVE parameters. Specific methods are proposed to determine the RVE for foam models.

- V- The investigated closed-cell foam models show stability. The comparison between the same structure with different kinematic modelings is carried out, which shows the model with solid elements is stiffer. By varying the relative density in the certain range, the approximate linear evolution of the effective elastic moduli is found. The comparison of the energy density is performed between our generated models and the tomography model without the periodic boundary condition. It shows in the elastic phase, the anisotropic model shows the different sensitivities to the periodic boundary condition along different directions. The numerical results have a satisfying agreement with the experimental results.

Prospects

- I- As an efficient approach, Hill's lemma periodic computational homogenization approach is proposed and implemented for predicting the effective linear elastic properties of foams in this thesis. It is possible and interesting to expand the field of its application. First, in addition to mechanical properties, this approach has the potential to estimate other properties, i.e. thermal properties, dielectric properties, magnetic properties, piezoelectric properties, etc. Second, besides linear properties, this approach has the potential to predict the non-linear properties. Third, the research object can also be extended to other composite materials.

- II- It is easy to impose the periodic boundary condition on the models with periodic structures. While the geometrical periodicity cannot always be satisfied for some structures, for example tomography reconstruction structures. We have verified that some existing methods of imposing the enforced periodic boundary condition are not appropriate for the high-porosity foam models (see Appendix B). It will be interesting to develop a method which can impose an enforced periodic boundary condition on the high-porosity model with non-periodic structure.

- III- The details of the morphology of foam models need to be studied further. Although a number of morphological parameters have already been considered, there are still some simplifications. For example, for open-cell foams, the average diameters of

the cross sections of strut are considered uniform. While for closed-cell foams, the thicknesses of the walls are uniform as well.

Appendix A

The variational asymptotic method for unit cell homogenization (VAMUCH)

The theoretical formulations, which are basis mathematical formulations of this work, have been presented in great detail on the work of [YU 07a]. Hence, the necessary equations will be presented. For elastic RVE, the strain energy density within the RVE [YU 07a] is :

$$\psi^{\text{hom}} = \left\langle \frac{1}{2} \boldsymbol{\epsilon} : \mathbb{C} : \boldsymbol{\epsilon} \right\rangle, \quad (\text{A.1})$$

The variational statement for RVE can be formulated as seeking the minimum value of the following functional based on finite element discretization :

$$\psi^{\text{hom}} = \frac{1}{2} \{\bar{\boldsymbol{\epsilon}}\}^T \langle \mathbb{C} \rangle \{\bar{\boldsymbol{\epsilon}}\} + \{\mathbf{u}'\}^T [\mathbf{F}] \{\bar{\boldsymbol{\epsilon}}\} + \frac{1}{2} \{\mathbf{u}'\}^T [\mathbf{K}] \{\mathbf{u}'\}. \quad (\text{A.2})$$

Therefore, one could obtain :

$$\frac{\partial \psi^{\text{hom}}}{\partial \{\mathbf{u}'\}} = 0, \quad (\text{A.3})$$

which leads to

$$[\mathbf{K}] \{\mathbf{u}'\} = -[\mathbf{F}] \{\bar{\boldsymbol{\epsilon}}\}, \text{ i.e. } \{\mathbf{u}'\} = [\mathbf{A}] \{\bar{\boldsymbol{\epsilon}}\} \quad (\text{A.4})$$

Finally, the macroscopic energy becomes

$$\psi^{\text{hom}} = \frac{1}{2} \{\bar{\boldsymbol{\epsilon}}\}^T (\langle \mathbb{C} \rangle + [\mathbf{A}] [\mathbf{F}]) \{\bar{\boldsymbol{\epsilon}}\} \equiv \frac{1}{2} \{\bar{\boldsymbol{\epsilon}}\}^T [\mathbb{C}^{\text{hom}}] \{\bar{\boldsymbol{\epsilon}}\}. \quad (\text{A.5})$$

Appendix B

Enforced periodic boundary condition

[YUA 08] presented a master/slave method for implementing the periodic boundary condition for non-periodic mesh. By enforcing the displacement field at intersections, [TYR 07] imposed the periodic boundary condition for a periodic 2D unit-cell with arbitrary non-periodic mesh. The Lagrange interpolation and the cubic spline interpolation were used by [NGU 12] to enforce strongly the periodic boundary condition on arbitrary finite element meshes of periodic and random materials in the 2-dimensional or 3-dimensional cases. By iteration, [WOJ 17] adopted a fixed point method to solve the problem that the geometries of the images of rocks or generated samples are non-periodic.

In this section, the polynomial interpolation and the fixed point method are attempted to enforce periodic boundary condition on non-periodic high porosity structure.

1 Polynomial interpolation

In [NGU 12], the method based on polynomial interpolation is implemented not only on the arbitrary meshes of periodic structures but also on the non-periodic structures. Since it is not difficult to realize the first case and we are more interesting in the second case, the non-periodic structure will be discussed next.

After meshing a non-periodic structure with linear tetrahedron solid elements, the nodes can be categorised into three sorts :

1. the nodes belong to the corners ;
2. the nodes belong to the edges without corners ;
3. the nodes belong to the surfaces without the edges or corners.

For the first sort : If there is a node on every corner, the periodic boundary condition is imposed as usual. If there is no node on one or more corners, the periodic boundary condition will not be considered because of the lack of periodicity.

For the second sort : The elements on the edges can be imagined as segments. Since the elements are linear and solid, the periodic displacement of a point inside an element can

be represented by those of two endpoints. Considering three real nodes and an imaginary node on edges (FIG. B.1), node $A^\#$ is on an edge while node $B^\#$ and node $C^\#$, which belong to same element, are on the opposite edge. The imaginary node A' which corresponds to node $A^\#$ is between node $B^\#$ and node $C^\#$. As said before, the periodic displacement of A' can be written as $\mathbf{u}'_{A'} = s_B \mathbf{u}'_{B^\#} + s_C \mathbf{u}'_{C^\#}$. The shape functions s_B and s_C are determined by the positions of the nodes. The correspondence between $A^\#$ and A' leads to $\mathbf{u}'_{A^\#} = s_B \mathbf{u}'_{B^\#} + s_C \mathbf{u}'_{C^\#}$.

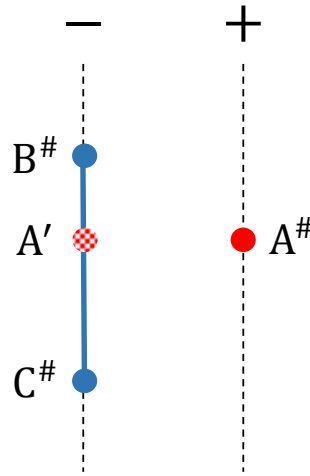


FIGURE B.1: Illustration of the positions and the relations of four nodes.

For the third sort : Comparing with the second one, the only difference is that the periodic displacement of the node $A^\#$ on a surface is represented by those of three nodes $B^\#$, $C^\#$ and $D^\#$ on the opposite surface, i.e. $\mathbf{u}'_{A^\#} = s_B \mathbf{u}'_{B^\#} + s_C \mathbf{u}'_{C^\#} + s_D \mathbf{u}'_{D^\#}$.

However taking into account the actual situation, i.e. the high porosity, only a few nodes have their corresponding nodes inside the elements on the opposite boundaries, while most of the corresponding nodes are outside. FIG. B.2 shows the the elements on two opposite surfaces of a non-periodic structure, which are marked in red and blue respectively. From the figure, one can see the overlapping areas account for only a small part. If only consider the nodes which have the corresponding nodes inside the elements, the periodic boundary condition will be imposed on a very small number of nodes. If consider all nodes, the above method will be based on interpolation and extrapolation as well. And the periodic displacement of a node, for example node $A^\#$, will be determined by those of the nodes closest to the corresponding node A' . Because of the high porosity, sometimes the distances among the nodes are very large, which will cause errors.

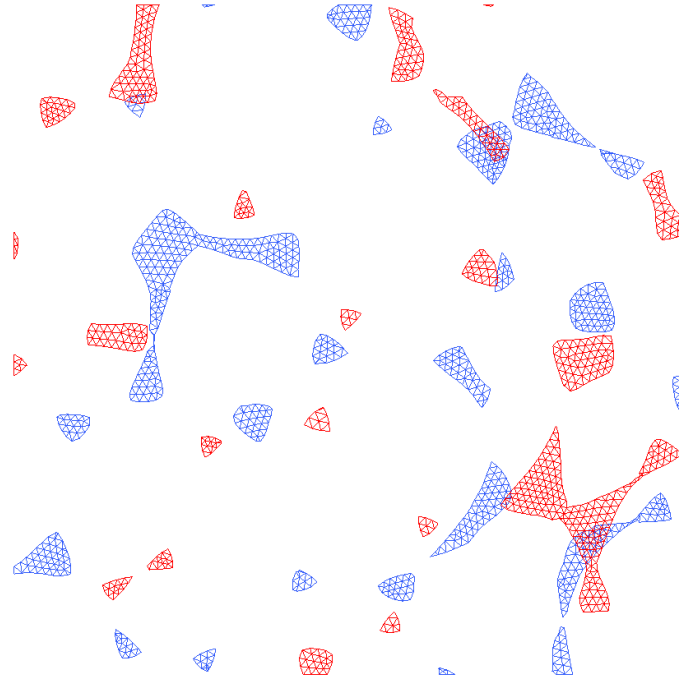


FIGURE B.2: The elements on two opposite surfaces.

2 Fixed point method

[WOJ 17] adopted the fixed point method to deal with non-periodic models. A layer is added around the cubic sample (FIG. B.3), so the periodic boundary condition is easy to be imposed. The stiffness matrix of the layer is defined as same as the stiffness matrix of the bulk initially. For every iteration, the stiffness matrix of the layer $[\mathbb{C}^{\text{layer}}]$ is updated as :

$$[\mathbb{C}^{\text{layer}}]_{[ii]} = [\mathbb{C}^{\text{hom}}]_{[ii-1]} \quad (\text{B.1})$$

where ii is the iteration number and $[\mathbb{C}^{\text{hom}}]$ is the overall stiffness matrix of the RVE (sample+layer). The stop criterion γ^{stop} is :

$$\gamma^{\text{stop}} = \frac{\|[\mathbb{C}^{\text{layer}}]_{[ii]} - [\mathbb{C}^{\text{hom}}]_{[ii]}\|_{\text{Frob}}}{\|[\mathbb{C}^{\text{hom}}]_{[ii]}\|_{\text{Frob}}} < 10^{-4}. \quad (\text{B.2})$$

In [WOJ 17], this method is efficient for sandstone microstructures with low porosity (4.6%). Kelvin open-cell structures ($q = 1, t = 1$) with domain dimension $2 \times 2 \times 2$ are chosen to study since they are periodic and the verifications are easy to be performed. The influences of several parameters are investigated in the following sections. The bulk properties are set as the Young's modulus $E^{\text{b}} = 70$ GPa and the Poisson's ratio $\nu^{\text{b}} = 0.3$. FIG. B.4 presents the section view of the combination of the Kelvin open-cell structure ($q = 1, t = 1, \rho^{\text{hom}}/\rho^{\text{b}} = 6\%$) and A layer.

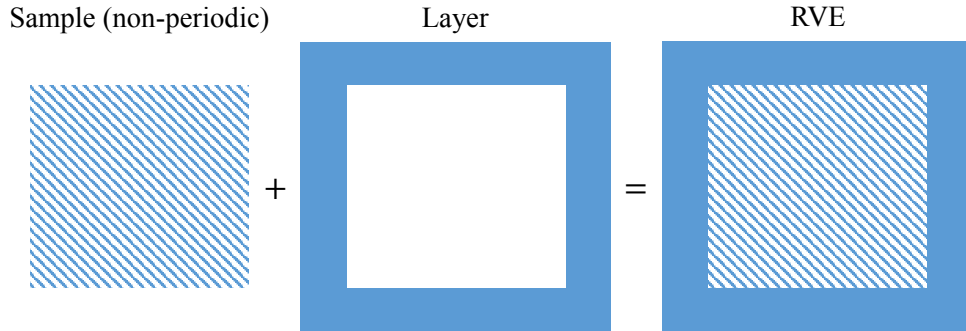


FIGURE B.3: Illustration of the fixed point method.

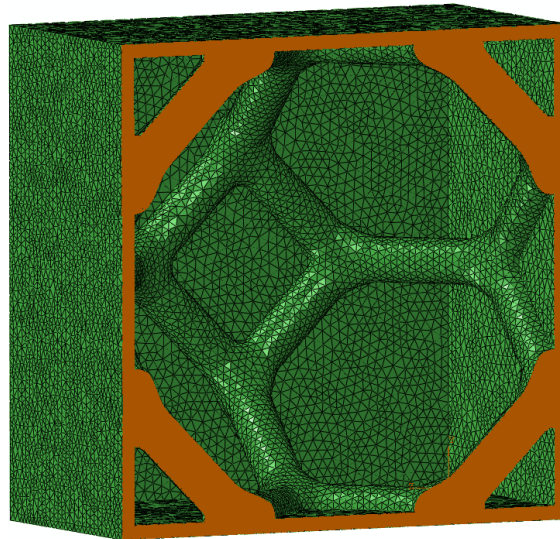


FIGURE B.4: Illustration of the Kelvin open-cell structure surrounded by a layer.

2.1 Influence of relative density

Kelvin open-cell structures ($q = 1, t = 1$) are defined with 6 different relative densities ($\rho^{\text{hom}}/\rho^{\text{b}} = \{4\%; 6\%; 8\%; 10\%; 12\%; 14\%\}$). For each model, the fixed point method is carried out and verified by imposing the periodic boundary condition directly on the model. The layer thickness of each model is 0.06 and the global mesh size of each RVE is 0.06.

For the model with $\rho^{\text{hom}}/\rho^{\text{b}} = 6\%$, the stiffness matrix obtained by imposing the

periodic boundary condition directly in the cubic frame (e_1, e_2, e_3) is :

$$[\mathbb{C}_{direct}^{hom}] = \begin{bmatrix} 783.94 & 538.81 & 538.90 & \sim 0 & \sim 0 & \sim 0 \\ & 783.33 & 538.71 & \sim 0 & \sim 0 & \sim 0 \\ & & 782.86 & \sim 0 & \sim 0 & \sim 0 \\ & Sym & & 88.56 & \sim 0 & \sim 0 \\ & & & & 88.65 & \sim 0 \\ & & & & & 88.59 \end{bmatrix} \text{ (MPa)}.$$

While by the fixed point method, the stiffness matrix is :

$$[\mathbb{C}_{FPM}^{hom}] = \begin{bmatrix} 150.79 & 77.67 & 77.48 & \sim 0 & \sim 0 & \sim 0 \\ & 151.39 & 77.67 & \sim 0 & \sim 0 & \sim 0 \\ & & 151.20 & \sim 0 & \sim 0 & \sim 0 \\ & Sym & & 27.95 & \sim 0 & \sim 0 \\ & & & & 27.97 & \sim 0 \\ & & & & & 28.01 \end{bmatrix} \text{ (MPa)}.$$

The difference between two stiffness matrix can be evaluated by :

$$\delta = \frac{\|[\mathbb{C}_{direct}^{hom}] - [\mathbb{C}_{FPM}^{hom}]\|_{Frob}}{\|[\mathbb{C}_{direct}^{hom}]\|_{Frob}}. \quad (\text{B.3})$$

FIG. B.5 shows the evolution of δ with the relative density. From the figure, one can see the foam model is affected by the layer significant because of the low relative density (or high porosity). δ is close to 1 when the relative density is very small. With the increase of the relative density, δ decreases rapidly, which means the effect of the layer weakens since the foam model becomes “strong”. According to the tendency, when the relative density reaches about 24%-30%, the error between the results is close to 0, while the relative density (95.4%) in [WOJ 17] is far more than the range.

2.2 Influence of layer thickness

Layers with different thicknesses ($l_{layer} = \{0.06; 0.09; 0.12\}$) are added respectively around the Kelvin open-cell structure ($q = 1, t = 1, \rho^{hom}/\rho^b = 6\%$) and the global mesh size of RVE is 0.06. FIG. B.6 shows the evolution of δ with the normalized layer thickness by the side length of the structure. From the above discussion, it is known that the layer has a great influence on the high porosity model. Increasing the thickness of the layer is equivalent to weakening the foam model. There is no doubt that δ will increase as the increase of the layer thickness.

2.3 Influence of number of elements

The layer is added around the Kelvin open-cell structure ($q = 1, t = 1, \rho^{hom}/\rho^b = 6\%$) and the thickness is fixed at 0.06. The global mesh sizes are 0.06, 0.05, 0.045 and 0.04,

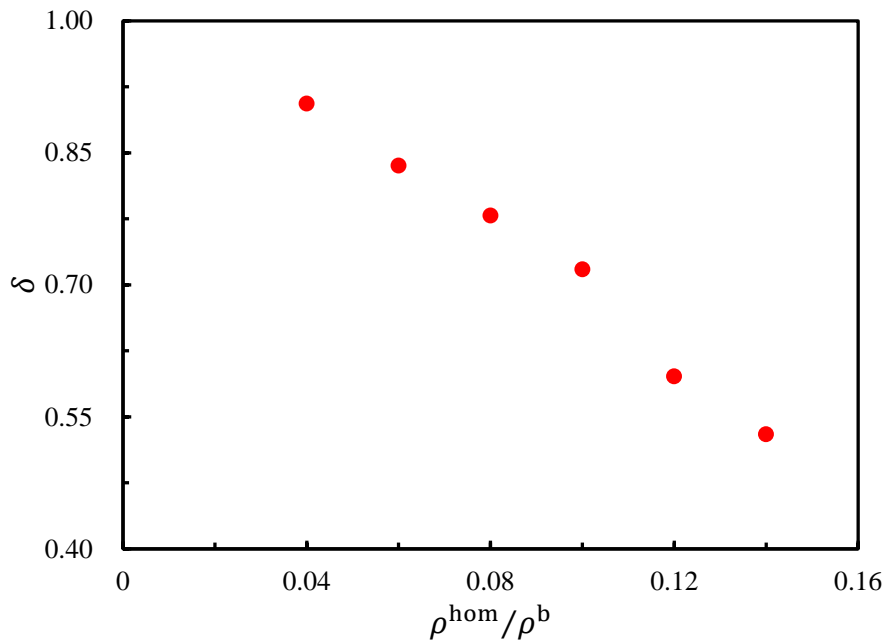


FIGURE B.5: Effect of the relative density on δ .

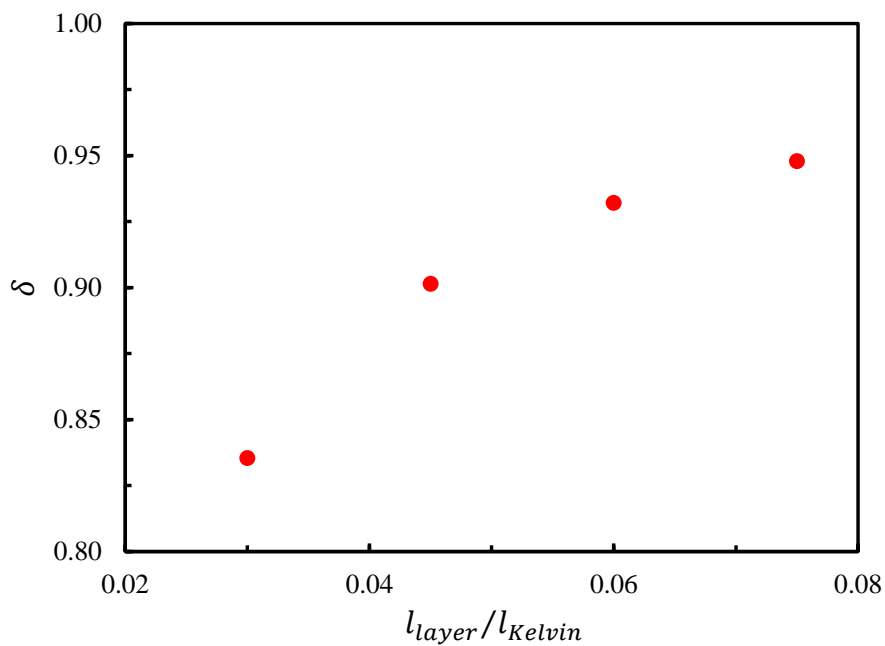


FIGURE B.6: Effect of the normalized layer thickness on δ .

corresponding to 29,452, 49,657, 76,369 and 110,494 elements for the foam model respectively. FIG. B.7 shows the evolution of δ with the number of elements of foam model. From the figure, one can see with the increase of number of elements, the difference bet-

ween the results obtained by two methods is more obvious and the convergent value of δ is about 0.866.

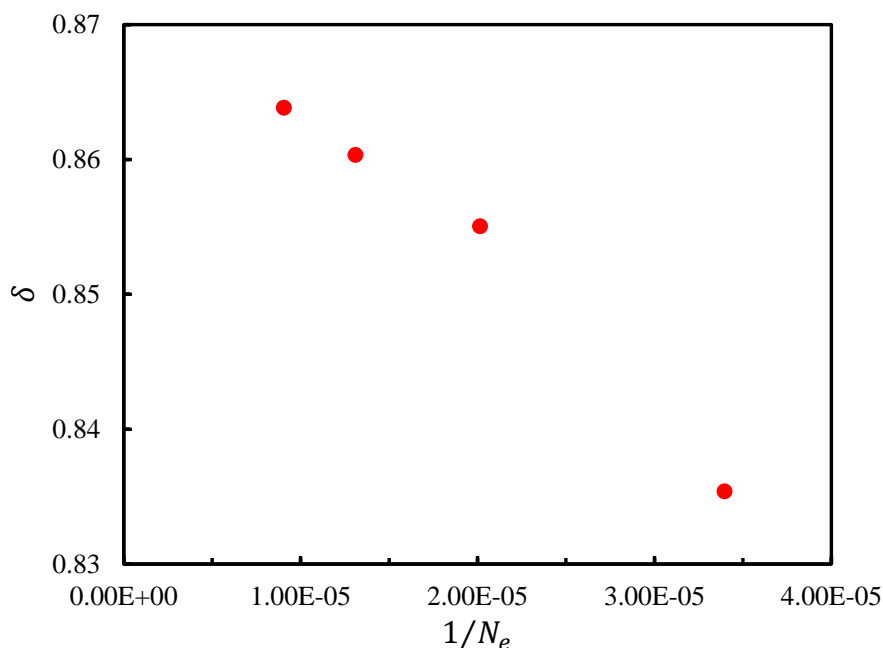


FIGURE B.7: Effect of the number of elements of foam model on δ .

3 Conclusion

For the high porosity foam models, the existing methods of imposing the enforced periodic boundary condition are not appropriate since the high porosity. There is only a small amount of bulk phase on the boundaries and its distribution is scattered, which will cause errors with the polynomial interpolation. Furthermore, the high porosity makes foam models too “weak” to be affected by layers significantly when using the fixed point method.

Bibliography

- [Aba 11] ABAQUS 6.11
Abaqus Analysis User's Manual. , 2011.
- [ANS 13] ANSYS I.
CFD User's Manual. *Ansys Inc.*, , 2013.
- [ARC 78] ARCAN M., HASHIN Z., VOLOSHIN A.
A method to produce uniform plane-stress states with applications to fiber-reinforced materials. *Experimental Mechanics*, vol. 18, n° 4, 1978, p. 141–146.
- [ASH 00] ASHBY M. F., EVANS T., FLECK N. A., HUTCHINSON J., WADLEY H., GIBSON L.
Metal foams : a design guide. Elsevier, 2000.
- [ASH 05] ASHBY M. F.
Materials Selection in Mechanical Design. Elsevier, Oxford, third édition, 2005.
- [ASH 13] ASHBY M.
Designing architected materials. *Scripta Materialia*, vol. 68, n° 1, 2013, p. 4 - 7.
- [BAB 07] BABIN P., VALLE G. D., DENDIEVEL R., LOURDIN D., SALVO L.
X-ray tomography study of the cellular structure of extruded starches and its relations with expansion phenomenon and foam mechanical properties. *Carbohydrate Polymers*, vol. 68, n° 2, 2007, p. 329 - 340.
- [BAD 00] BADICHE X., FOREST S., GUIBERT T., BIENVENU Y., BARTOUT J.-D., IENNY P., CROSET M., BERNET H.
Mechanical properties and non-homogeneous deformation of open-cell nickel foams : application of the mechanics of cellular solids and of porous materials. *Materials Science and Engineering : A*, vol. 289, n° 1, 2000, p. 276 - 288.
- [BAI 08] BAILLIS D., COQUARD R.
Radiative and Conductive Thermal Properties of Foams, p. 343–384. Wiley-VCH Verlag GmbH & Co. KGaA, 2008.
- [BAI 17] BAILLIS D., COQUARD R., CUNSOLO S.
Effective conductivity of Voronoi's closed- and open-cell foams : analytical laws and

- numerical results. *Journal of Materials Science*, vol. 52, n° 19, 2017, p. 11146–11167.
- [BAN 03] BANHART J.
Aluminum foams : On the road to real applications. *Mrs Bulletin*, vol. 28, n° 4, 2003, p. 290–295, Cambridge University Press.
- [BAR 14a] BARBIER C., MICHAUD P., BAILLIS D., RANDRIANALISOA J., COMBES-CURE A.
New laws for the tension/compression properties of Voronoi closed-cell polymer foams in relation to their microstructure. *European Journal of Mechanics - A/Solids*, vol. 45, 2014, p. 110 - 122.
- [BAR 14b] BARNES A., RAVI-CHANDAR K., KYRIAKIDES S., GAITANAROS S.
Dynamic crushing of aluminum foams : Part I - Experiments. *International Journal of Solids and Structures*, vol. 51, n° 9, 2014, p. 1631 - 1645.
- [BEN 87] BENVENISTE Y.
A new approach to the application of Mori-Tanaka's theory in composite materials. *Mechanics of Materials*, vol. 6, n° 2, 1987, p. 147 - 157.
- [BER 68] BERAN M. J.
Statistical Continuum Theories. *American Journal of Physics*, vol. 36, n° 10, 1968, p. 923-923.
- [BER 93] BERRYMAN J. G., BERGE P. A.
Rock elastic properties : dependence on microstructure. *ASME APPLIED MECHANICS DIVISION-PUBLICATIONS-AMD*, vol. 166, 1993, p. 1–13, ASME.
- [BRA 92] BRAKKE K. A.
The Surface Evolver. *Experimental Mathematics*, vol. 1, n° 2, 1992, p. 141-165.
- [BRU 08] BRUN E., VICENTE J., TOPIN F., OCCELLI R.
IMorph : A 3D morphological tool to fully analyse all kind of cellular materials. Dresden, Germany, 2008 CELLMET2008.
- [BUD 65] BUDIANSKY B.
On the elastic moduli of some heterogeneous materials. *Journal of the Mechanics and Physics of Solids*, vol. 13, n° 4, 1965, p. 223 - 227.
- [CAI 94] CAILLETAUD G., JEULIN D., ROLLAND P.
Size effect on elastic properties of random composites. *Engineering computations*, vol. 11, n° 2, 1994, p. 99–110.
- [CAI 03] CAILLETAUD G., FOREST S., JEULIN D., FEYEL F., GALLIET I., MOUNOURY V., QUILICI S.

- Some elements of microstructural mechanics. *Computational Materials Science*, vol. 27, n° 3, 2003, p. 351 - 374.
- [CAO 06] QING CAO X., HUA WANG Z., WEI MA H., MAO ZHAO L., TONG YANG G.
Effects of cell size on compressive properties of aluminum foam. *Transactions of Nonferrous Metals Society of China*, vol. 16, n° 2, 2006, p. 351 - 356.
- [CAT 08] CATY O., MAIRE E., YOUSSEF S., BOUCHET R.
Modeling the properties of closed-cell cellular materials from tomography images using finite shell elements. *Acta Materialia*, vol. 56, n° 19, 2008, p. 5524 - 5534.
- [CHE 15] CHEN Y., DAS R., BATTLE M.
Effects of cell size and cell wall thickness variations on the stiffness of closed-cell foams. *International Journal of Solids and Structures*, vol. 52, 2015, p. 150 - 164.
- [CHU 85] CHU T. C., RANSON W. F., SUTTON M. A.
Applications of digital-image-correlation techniques to experimental mechanics. *Experimental Mechanics*, vol. 25, n° 3, 1985, p. 232-244.
- [CIA 10] CIAMBELLI P., PALMA V., PALO E.
Comparison of ceramic honeycomb monolith and foam as Ni catalyst carrier for methane autothermal reforming. *Catalysis Today*, vol. 155, n° 1, 2010, p. 92 - 100.
- [COG 11] COGNARD J., SOHIER L., DAVIES P.
A modified Arcan test to analyze the behavior of composites and their assemblies under out-of-plane loadings. *Composites Part A : Applied Science and Manufacturing*, vol. 42, n° 1, 2011, p. 111 - 121.
- [COQ 06] COQUARD R., BAILLIS D.
Modeling of heat transfer in low-density EPS foams. *J. Heat Trans*, vol. 128, 2006, p. 538-549.
- [CUN 17] CUNSOLO S., COQUARD R., BAILLIS D., CHIU W. K., BIANCO N.
Radiative properties of irregular open cell solid foams. *International Journal of Thermal Sciences*, vol. 117, 2017, p. 77 - 89.
- [DAN 00] DANNEMANN K. A., LANKFORD J.
High strain rate compression of closed-cell aluminium foams. *Materials Science and Engineering : A*, vol. 293, n° 1, 2000, p. 157 - 164.
- [DAV 83] DAVIES G. J., ZHEN S.
Metallic foams : their production, properties and applications. *Journal of Materials Science*, vol. 18, n° 7, 1983, p. 1899-1911.

- [DIL 05] DILLARD T., N'GUYEN F., MAIRE E., SALVO L., FOREST* S., BIENVENU Y., BARTOUT J.-D., CROSET M., DENDIEVEL R., CLOETENS P.
3D quantitative image analysis of open-cell nickel foams under tension and compression loading using X-ray microtomography. *Philosophical Magazine*, vol. 85, n° 19, 2005, p. 2147–2175, Taylor & Francis.
- [DIR 12] DIRRENBERGER J.
Effective properties of architected materials. Thèse de doctorat, MINES-ParisTech, 2012.
- [DRU 96] DRUGAN W., WILLIS J.
A micromechanics-based nonlocal constitutive equation and estimates of representative volume element size for elastic composites. *Journal of the Mechanics and Physics of Solids*, vol. 44, n° 4, 1996, p. 497 - 524.
- [DÜS 12] DÜSTER A., SEHLHORST H.-G., RANK E.
Numerical homogenization of heterogeneous and cellular materials utilizing the finite cell method. *Computational Mechanics*, vol. 50, n° 4, 2012, p. 413–431.
- [FAN 17] FENG FAN S., ZHANG T., YU K., JIE FANG H., QING XIONG H., LONG DAI Y., JI MA J., YUE JIANG D., LONG ZHU H.
Compressive properties and energy absorption characteristics of open-cell nickel foams. *Transactions of Nonferrous Metals Society of China*, vol. 27, n° 1, 2017, p. 117 - 124.
- [FEN 04] FEND T., ROBERT-PITZ-PAAL, REUTTER O., BAUER J., HOFFSCHMIDT B.
Two novel high-porosity materials as volumetric receivers for concentrated solar radiation. vol. 84, 2004, p. 291 - 304.
- [FEY 00] FEYEL F., CHABOCHE J.-L.
FE2 multiscale approach for modelling the elastoviscoplastic behaviour of long fibre SiC/Ti composite materials. *Computer Methods in Applied Mechanics and Engineering*, vol. 183, n° 3, 2000, p. 309 - 330.
- [FIS 16] FISCHER S. F.
Energy absorption efficiency of open-cell pure aluminum foams. *Materials Letters*, vol. 184, n° Supplement C, 2016, p. 208 - 210.
- [FRI 12] FRITZEN F., FOREST S., BÖHLKE T., KONDO D., KANIT T.
Computational homogenization of elasto-plastic porous metals. *International Journal of Plasticity*, vol. 29, 2012, p. 102 - 119.
- [GAI 12] GAITANAROS S., KYRIAKIDES S., KRAYNIK A. M.
On the crushing response of random open-cell foams. *International Journal of Solids and Structures*, vol. 49, n° 19, 2012, p. 2733 - 2743.

- [GAI 14] GAITANAROS S., KYRIAKIDES S.
Dynamic crushing of aluminum foams : Part II–Analysis. *International Journal of Solids and Structures*, vol. 51, n° 9, 2014, p. 1646 - 1661.
- [GAI 15] GAITANAROS S., KYRIAKIDES S.
On the effect of relative density on the crushing and energy absorption of open-cell foams under impact. *International Journal of Impact Engineering*, vol. 82, 2015, p. 3 - 13.
- [GAN 05] GAN Y., CHEN C., SHEN Y.
Three-dimensional modeling of the mechanical property of linearly elastic open cell foams. *International Journal of Solids and Structures*, vol. 42, n° 26, 2005, p. 6628 - 6642.
- [GAT 05] GATT J.-M., MONERIE Y., LAUX D., BARON D.
Elastic behavior of porous ceramics : application to nuclear fuel materials. *Journal of Nuclear Materials*, vol. 336, n° 2-3, 2005, p. 145 - 155.
- [GAU 07] GAUTHIER S., LEBAS E., BAILLIS D.
SFGP 2007-natural gas/hydrogen mixture combustion in a porous radiant burner. *International Journal of Chemical Reactor Engineering*, vol. 5, n° 1, 2007, page A114.
- [GEE 16] GEERS M., YVONNET J.
Multiscale Modeling of Microstructure-Property Relations. *MRS Bulletin*, vol. 41, n° 08, 2016, p. 610-616, Cambridge University Press (CUP).
- [GHO 12] GHOSSEIN E., LÉVESQUE M.
A fully automated numerical tool for a comprehensive validation of homogenization models and its application to spherical particles reinforced composites. *International Journal of Solids and Structures*, vol. 49, n° 11, 2012, p. 1387 - 1398.
- [GIB 82a] GIBSON L., ASHBY M.
The mechanics of three-dimensional cellular materials. *Proc. R. Soc. Lond. A*, vol. 382, n° 1782, 1982, p. 43–59, The Royal Society.
- [GIB 82b] GIBSON L. J., SCHAJER G., ROBERTSON C.
The mechanics of two-dimensional cellular materials. *Proc. R. Soc. Lond. A*, vol. 382, n° 1782, 1982, p. 25–42, The Royal Society.
- [GIB 97] GIBSON L., ASHBY M.
Cellular Solids : Structure and properties. Cambridge University Press, Cambridge., 1997.
- [GIB 00] GIBSON L.
Mechanical behavior of metallic foams. *Annual review of materials science*, vol. 30, n° 1, 2000, p. 191–227.

- [GIT 07] GITMAN I., ASKES H., SLUYS L.
Representative volume : Existence and size determination. *Engineering Fracture Mechanics*, vol. 74, n° 16, 2007, p. 2518 - 2534.
- [GON 05] GONG L., KYRIAKIDES S., JANG W.-Y.
Compressive response of open-cell foams. Part I : Morphology and elastic properties. *International Journal of Solids and Structures*, vol. 42, n° 5, 2005, p. 1355 - 1379.
- [GRE 98] GRENESTEDT J. L.
Influence of wavy imperfections in cell walls on elastic stiffness of cellular solids. *Journal of the Mechanics and Physics of Solids*, vol. 46, n° 1, 1998, p. 29 - 50.
- [GRE 00] GRENESTEDT J. L., BASSINET F.
Influence of cell wall thickness variations on elastic stiffness of closed-cell cellular solids. *International Journal of Mechanical Sciences*, vol. 42, n° 7, 2000, p. 1327 - 1338.
- [GUS 97] GUSEV A. A.
Representative volume element size for elastic composites : A numerical study. *Journal of the Mechanics and Physics of Solids*, vol. 45, n° 9, 1997, p. 1449 - 1459.
- [HAI 08] HAIN M., WRIGGERS P.
Numerical homogenization of hardened cement paste. *Computational Mechanics*, vol. 42, n° 2, 2008, p. 197-212.
- [HAN 98] HAN F., ZHU Z., GAO J.
Compressive deformation and energy absorbing characteristic of foamed aluminum. *Metallurgical and Materials Transactions A*, vol. 29, n° 10, 1998, p. 2497-2502.
- [HAR 99] HARTE A.-M., FLECK N., ASHBY M.
Fatigue failure of an open cell and a closed cell aluminium alloy foam. *Acta Materialia*, vol. 47, n° 8, 1999, p. 2511 - 2524.
- [HAS 62] HASHIN Z., SHTRIKMAN S.
On some variational principles in anisotropic and nonhomogeneous elasticity. *Journal of the Mechanics and Physics of Solids*, vol. 10, n° 4, 1962, p. 335 - 342.
- [HAS 63] HASHIN Z., SHTRIKMAN S.
A variational approach to the theory of the elastic behaviour of multiphase materials. *Journal of the Mechanics and Physics of Solids*, vol. 11, n° 2, 1963, p. 127 - 140.
- [HAS 83] HASHIN Z.
Analysis of Composite Materials - A Survey. *Journal of Applied Mechanics*, vol. 50, n° 2, 1983, p. 481-505.

- [HER 54] HERSHEY A.
The elasticity of an isotropic aggregate of anisotropic cubic crystals. *Journal of Applied mechanics-transactions of the ASME*, vol. 21, n° 3, 1954, p. 236–240.
- [HIL 63] HILL R.
Elastic properties of reinforced solids : Some theoretical principles. *Journal of the Mechanics and Physics of Solids*, vol. 11, n° 5, 1963, p. 357 - 372.
- [HIL 65] HILL R.
A self-consistent mechanics of composite materials. *Journal of the Mechanics and Physics of Solids*, vol. 13, n° 4, 1965, p. 213 - 222.
- [HUN 97] HUNG S. C., LIECHTI K. M.
An evaluation of the arcan specimen for determining the shear moduli of fiber-reinforced composites. *Experimental Mechanics*, vol. 37, n° 4, 1997, p. 460–468.
- [ILU 13] ILUK A.
Global stability of an aluminum foam stand-alone energy absorber. *Archives of Civil and Mechanical Engineering*, vol. 13, n° 2, 2013, p. 137 - 143.
- [JAN 08] JANG W.-Y., KRAYNIK A. M., KYRIAKIDES S.
On the microstructure of open-cell foams and its effect on elastic properties. *International Journal of Solids and Structures*, vol. 45, n° 7, 2008, p. 1845 - 1875.
- [JAN 09] JANG W.-Y., KYRIAKIDES S.
On the crushing of aluminum open-cell foams : Part I. Experiments. *International Journal of Solids and Structures*, vol. 46, n° 3, 2009, p. 617 - 634.
- [JIN 16] JING L., WANG Z., ZHAO L.
The dynamic response of sandwich panels with cellular metal cores to localized impulsive loading. *Composites Part B : Engineering*, vol. 94, n° Supplement C, 2016, p. 52 - 63.
- [JUN 15] JUNG A., BEECH L., DIEBELS S., BORDAS S.
Open-cell aluminium foams with graded coatings as passively controllable energy absorbers. *Materials & Design*, vol. 87, n° Supplement C, 2015, p. 36 - 41.
- [KAE 10] KAEMMERLEN A., VO C., ASLLANAJ F., JEANDEL G., BAILLIS D.
Radiative properties of extruded polystyrene foams : Predictive model and experimental results. *Journal of Quantitative Spectroscopy and Radiative Transfer*, vol. 111, n° 6, 2010, p. 865 - 877.
- [KAN 03] KANIT T., FOREST S., GALLIET I., MOUNOURY V., JEULIN D.
Determination of the size of the representative volume element for random composites : statistical and numerical approach. *International Journal of Solids and Structures*, vol. 40, n° 13-14, 2003, p. 3647 - 3679.

- [KAN 06] KANIT T., N'GUYEN F., FOREST S., JEULIN D., REED M., SINGLETON S.
Apparent and effective physical properties of heterogeneous materials : Representativity of samples of two materials from food industry. *Computer Methods in Applied Mechanics and Engineering*, vol. 195, n° 33, 2006, p. 3960 - 3982.
- [KAR 07] KARI S., BERGER H., GABBERT U.
Numerical evaluation of effective material properties of randomly distributed short cylindrical fibre composites. *Computational Materials Science*, vol. 39, n° 1, 2007, p. 198 - 204.
- [KÖL 16] KÖLL J., HALLSTRÖM S.
Elastic properties of equilibrium foams. *Acta Materialia*, vol. 113, 2016, p. 11 - 18.
- [KRA 94] KRAYNIK A. M., WARREN W. E.
The elastic behavior of low-density cellular plastics, p. 187–225. Springer Netherlands, Dordrecht, 1994.
- [KRA 03] KRAYNIK A. M., REINELT D. A., VAN SWOL F.
Structure of random monodisperse foam. *Phys. Rev. E*, vol. 67, 2003, page 031403, American Physical Society.
- [KRA 04] KRAYNIK A. M., REINELT D. A., VAN SWOL F.
Structure of Random Foam. *Phys. Rev. Lett.*, vol. 93, 2004, page 208301, American Physical Society.
- [KRÖ 58] KRÖNER E.
Berechnung der elastischen Konstanten des Vielkristalls aus den Konstanten des Einkristalls. *Zeitschrift für Physik*, vol. 151, n° 4, 1958, p. 504–518.
- [KUR 04] KURUKURI S.
A review of homogenization techniques for heterogeneous materials. *Term paper: Advanced Mechanics of Materials and Structures, Graduate School in Structural Engineering, Germany*, , 2004.
- [LAR 11] LARSSON F., RUNESSON K., SAROUKHANI S., VAFADARI R.
Computational homogenization based on a weak format of micro-periodicity for RVE-problems. *Computer Methods in Applied Mechanics and Engineering*, vol. 200, n° 1, 2011, p. 11 - 26.
- [LI 06] LI K., GAO X.-L., SUBHASH G.
Effects of cell shape and strut cross-sectional area variations on the elastic properties of three-dimensional open-cell foams. *Journal of the Mechanics and Physics of Solids*, vol. 54, n° 4, 2006, p. 783 - 806.
- [LI 14a] LI Z., XI C., JING L., WANG Z., ZHAO L.
Effect of loading rate on the compressive properties of open-cell metal foams. *Materials Science and Engineering : A*, vol. 592, 2014, p. 221–229, Elsevier.

- [LI 14b] LI Z., ZHANG J., FAN J., WANG Z., ZHAO L.
On crushing response of the three-dimensional closed-cell foam based on Voronoi model. *Mechanics of Materials*, vol. 68, 2014, p. 85 - 94.
- [LIU 14] LIU Y., GONG W., ZHANG X.
Numerical investigation of influences of porous density and strain-rate effect on dynamical responses of aluminum foam. *Computational Materials Science*, vol. 91, 2014, p. 223–230, Elsevier.
- [LU 99] LU T., CHEN C.
Thermal transport and fire retardance properties of cellular aluminium alloys. *Acta Materialia*, vol. 47, n° 5, 1999, p. 1469 - 1485.
- [MAI 03] MAIRE E., FAZEKAS A., SALVO L., DENDIEVEL R., YOUSSEF S., CLOETENS P., LETANG J. M.
X-ray tomography applied to the characterization of cellular materials. Related finite element modeling problems. *Composites Science and Technology*, vol. 63, n° 16, 2003, p. 2431 - 2443.
- [MAT 71] MATHERON G.
The Theory of Regionalized Variables and Its Applications. Ecole Nationale Supérieure des Mines de Paris - Les Cahiers du Centre de Morphologie Mathématique de Fontainebleau, Paris, France, 1971.
- [MAT 75] MATHERON G.
Random sets and integral geometry. John Wiley & Sons, New York, 1975.
- [MAT 16] MATLAB
MATLAB Primer. The MathWorks Inc., 2016.
- [MEN 75] MENGES G., KNIPSCHILD F.
Estimation of mechanical properties for rigid polyurethane foams. *Polymer Engineering & Science*, vol. 15, n° 8, 1975, p. 623–627, Wiley Online Library.
- [MEY 16] MEY-CLOUTIER S., CALIOT C., KRIBUS A., GRAY Y., FLAMANT G.
Experimental study of ceramic foams used as high temperature volumetric solar absorber. *Solar Energy*, vol. 136, 2016, p. 226 - 235.
- [MGU 97] MGUIL-TOUCHAL S., MORESTIN F., BRUNEI M.
Various experimental applications of digital image correlation method. *International conference on computational methods and experimental measurements*, Rhodes, 1997 p. 45-58.
- [MIC 99] MICHEL J., MOULINEC H., SUQUET P.
Effective properties of composite materials with periodic microstructure : a computational approach. *Computer Methods in Applied Mechanics and Engineering*, vol. 172, n° 1, 1999, p. 109 - 143.

- [MIL 99] MILLS N., ZHU H.
The high strain compression of closed-cell polymer foams. *Journal of the Mechanics and Physics of Solids*, vol. 47, n° 3, 1999, p. 669 - 695.
- [MIL 00] MILLS N.
Micromechanics of polymeric foams. *Proceedings of the 3rd Nordic Meeting on Materials and Mechanics*, 2000, p. 45–76.
- [MIR 16] MIRZAALI M., LIBONATI F., VENA P., MUSSI V., VERGANI L., STRANO M.
Investigation of the Effect of Internal Pores Distribution on the Elastic Properties of Closed-Cell Aluminum Foam : A Comparison with Cancellous Bone. *Procedia Structural Integrity*, vol. 2, 2016, p. 1285 - 1294.
- [MIY 02] MIYOSHI T., MUKAI T., HIGASHI K.
Energy Absorption in Closed-Cell Al-Zn-Mg-Ca-Ti Foam. *MATERIALS TRANSACTIONS*, vol. 43, n° 7, 2002, p. 1778-1781.
- [MOR 73] MORI T., TANAKA K.
Average stress in matrix and average elastic energy of materials with misfitting inclusions. *Acta Metallurgica*, vol. 21, n° 5, 1973, p. 571 - 574.
- [MOU 98] MOULINEC H., SUQUET P.
A numerical method for computing the overall response of nonlinear composites with complex microstructure. *Computer Methods in Applied Mechanics and Engineering*, vol. 157, n° 1, 1998, p. 69 - 94.
- [MOU 13] MOUSSADDY H., THERRIault D., LÉVESQUE M.
Assessment of existing and introduction of a new and robust efficient definition of the representative volume element. *International Journal of Solids and Structures*, vol. 50, n° 24, 2013, p. 3817 - 3828.
- [MOU 14] MOUSANEZHAD D., GHOSH R., AJDARI A., HAMOUDA A., NAYEB-HASHEMI H., VAZIRI A.
Impact resistance and energy absorption of regular and functionally graded hexagonal honeycombs with cell wall material strain hardening. *International Journal of Mechanical Sciences*, vol. 89, 2014, p. 413 - 422.
- [MUK 99a] MUKAI T., KANAHASHI H., YAMADA Y., SHIMOJIMA K., MABUCHI M., NIEH T., HIGASHI K.
Dynamic compressive behavior of an ultra-lightweight magnesium foam. *Scripta Materialia*, vol. 41, n° 4, 1999, p. 365 - 371.
- [MUK 99b] MUKAI T., KANAHASHI H., YAMADA Y., SHIMOJIMA K., MABUCHI M., NIEH T., HIGASHI K.
Dynamic compressive behavior of an ultra-lightweight magnesium foam. *Scripta Materialia*, vol. 41, n° 4, 1999, p. 365–371, Pergamon.

- [NAM 10] NAMMI S., MYLER P., EDWARDS G.
Finite element analysis of closed-cell aluminium foam under quasi-static loading. *Materials & Design*, vol. 31, n° 2, 2010, p. 712–722, Elsevier.
- [NGU 12] NGUYEN V.-D., BÉCHET E., GEUZAIN C., NOELS L.
Imposing periodic boundary condition on arbitrary meshes by polynomial interpolation. *Computational Materials Science*, vol. 55, 2012, p. 390 - 406.
- [NIE 00] NIEH T., HIGASHI K., WADSWORTH J.
Effect of cell morphology on the compressive properties of open-cell aluminum foams. *Materials Science and Engineering : A*, vol. 283, n° 1, 2000, p. 105 - 110.
- [ODE 97] ODEN J., ZOHDI T. I.
Analysis and adaptive modeling of highly heterogeneous elastic structures. *Computer Methods in Applied Mechanics and Engineering*, vol. 148, n° 3, 1997, p. 367 - 391.
- [OST 98] OSTOJA-STARZEWSKI M.
Random field models of heterogeneous materials. *International Journal of Solids and Structures*, vol. 35, n° 19, 1998, p. 2429 - 2455.
- [OST 02] OSTOJA-STARZEWSKI M.
Microstructural randomness versus representative volume element in thermomechanics. *Journal of Applied Mechanics*, vol. 69, n° 1, 2002, p. 25–35.
- [OVE 98] OVERAKER D. W., CUITIÑO A. M., LANGRANA N. A.
Effects of morphology and orientation on the behavior of two-dimensional hexagonal foams and application in a re-entrant foam anchor model. *Mechanics of Materials*, vol. 29, n° 1, 1998, p. 43 - 52.
- [PAB 18] PABST W., UHLÍŘOVÁ T., GREGOROVÁ E., WIEGMANN A.
Young’s modulus and thermal conductivity of closed-cell, open-cell and inverse ceramic foams—model-based predictions, cross-property predictions and numerical calculations. *Journal of the European Ceramic Society*, vol. 38, n° 6, 2018, p. 2570–2578, Elsevier.
- [PEL 09] PELISSOU C., BACCOU J., MONERIE Y., PERALES F.
Determination of the size of the representative volume element for random quasi-brittle composites. *International Journal of Solids and Structures*, vol. 46, n° 14, 2009, p. 2842 - 2855.
- [PLA 73] PLATEAU J. A. F.
Statique expérimentale et théorique des liquides soumis aux seules forces moléculaires, vol. 2. Gauthier-Villars, 1873.
- [PLA 05] PLACIDO E., ARDUINI-SCHUSTER M., KUHN J.
Thermal properties predictive model for insulating foams. *Infrared Physics & Technology*, vol. 46, n° 3, 2005, p. 219 - 231.

- [RAJ 08] RAJENDRAN R., SAI K. P., CHANDRASEKAR B., GOKHALE A., BASU S.
Preliminary investigation of aluminium foam as an energy absorber for nuclear transportation cask. *Materials & Design*, vol. 29, n° 9, 2008, p. 1732 - 1739.
- [REU 29] REUSS A.
Berechnung der Fließgrenze von Mischkristallen auf Grund der Plastizitätsbedingung für Einkristalle. *ZAMM - Journal of Applied Mathematics and Mechanics / Zeitschrift für Angewandte Mathematik und Mechanik*, vol. 9, n° 1, 1929, p. 49–58.
- [ROB 00] ROBERTS A. P., GARBOCZI E. J.
Elastic Properties of Model Porous Ceramics. *Journal of the American Ceramic Society*, vol. 83, n° 12, 2000, p. 3041–3048, American Ceramics Society.
- [ROB 01] ROBERTS A., GARBOCZI E.
Elastic moduli of model random three-dimensional closed-cell cellular solids. *Acta Materialia*, vol. 49, n° 2, 2001, p. 189 - 197.
- [ROM 08] ROMERO P. A.
Three-dimensional finite-deformation multiscale modeling of elasto-viscoplastic open-cell foams in the dynamic regime. Thèse de doctorat, Rutgers, The State University of New Jersey-New Brunswick, 2008.
- [RUI 15] RUIZ C. J. Z., SZCZUREK A., DE YUSO ARISA A. M., RONDA J. C., CÁDIZ V., FIERRO V., CELZARD A.
Closed-cell carbon foams from diphenolic acid-based polybenzoxazine. *Carbon*, vol. 95, 2015, p. 919 - 929.
- [RYC 09] RYCROFT C. H.
VORO++ : A three-dimensional Voronoi cell library in C++. *Chaos*, vol. 19, n° 4, 2009.
- [SAB 92] SAB K.
On the homogenization and the simulation of random materials. *European journal of mechanics. A. Solids*, vol. 11, n° 5, 1992, p. 585–607.
- [SAL 12] SALMI M., AUSLENDER F., BORNERT M., FOGLI M.
Various estimates of Representative Volume Element sizes based on a statistical analysis of the apparent behavior of random linear composites. *Comptes Rendus Mécanique*, vol. 340, n° 4, 2012, p. 230 - 246.
- [SHA 94] SHAPOVALOV V.
Porous Metals. *MRS Bulletin*, vol. 19, n° 4, 1994, p. 24–28.
- [SHU 98] SHULMEISTER V.
Modelling of the Mechanical Properties of Low-Density Foams. Thèse de doctorat, Delft University of Technology, 1998.

- [SIN 00] SINGHAL S.
Advances in solid oxide fuel cell technology. *Solid State Ionics*, vol. 135, n° 1, 2000, p. 305 - 313.
- [SON 10] SONG Y., WANG Z., ZHAO L., LUO J.
Dynamic crushing behavior of 3D closed-cell foams based on Voronoi random model. *Materials & Design*, vol. 31, n° 9, 2010, p. 4281 - 4289.
- [STO 13a] STORM J., ABENDROTH M., EMMEL M., LIEDKE T., BALLASCHK U., VOIGT C., SIEBER T., KUNA M.
Geometrical modelling of foam structures using implicit functions. *International Journal of Solids and Structures*, vol. 50, n° 3, 2013, p. 548 - 555.
- [STO 13b] STORM J., ABENDROTH M., ZHANG D., KUNA M.
Geometry Dependent Effective Elastic Properties of Open-Cell Foams Based on Kelvin Cell Models. *Advanced Engineering Materials*, vol. 15, n° 12, 2013, p. 1292–1298, Wiley Online Library.
- [STO 15] STORM J., ABENDROTH M., KUNA M.
Influence of curved struts, anisotropic pores and strut cavities on the effective elastic properties of open-cell foams. *Mechanics of Materials*, vol. 86, 2015, p. 1 - 10.
- [STO 16] STORM J., ABENDROTH M., KUNA M.
Numerical and analytical solutions for anisotropic yield surfaces of the open-cell Kelvin foam. *International Journal of Mechanical Sciences*, vol. 105, 2016, p. 70 - 82.
- [SUQ 87] SUQUET P. M.
Elements of Homogenization for Inelastic Solid Mechanics, p. 193–278. Springer Berlin Heidelberg, Berlin, Heidelberg, 1987.
- [TAN 08a] TANG T., YU W.
Variational asymptotic homogenization of heterogeneous electromagnetoelastic materials. *International Journal of Engineering Science*, vol. 46, n° 8, 2008, p. 741 - 757.
- [TAN 08b] TANG T., YU W.
Variational asymptotic micromechanics modeling of heterogeneous piezoelectric materials. *Mechanics of Materials*, vol. 40, n° 10, 2008, p. 812 - 824.
- [TER 00] TERADA K., HORI M., KYOYA T., KIKUCHI N.
Simulation of the multi-scale convergence in computational homogenization approaches. *International Journal of Solids and Structures*, vol. 37, n° 16, 2000, p. 2285 - 2311.
- [THO 42] THOMPSON D. W.
On growth and form. Cambridge Univ. Press, 1942.

- [TRI 06] TRIAS D., COSTA J., TURON A., HURTADO J.
Determination of the critical size of a statistical representative volume element (SRVE) for carbon reinforced polymers. *Acta Materialia*, vol. 54, n° 13, 2006, p. 3471 - 3484.
- [TYR 07] TYRUS J., GOSZ M., DESANTIAGO E.
A local finite element implementation for imposing periodic boundary conditions on composite micromechanical models. *International Journal of Solids and Structures*, vol. 44, n° 9, 2007, p. 2972 - 2989.
- [VOI 89] VOIGT W.
Ueber die Beziehung zwischen den beiden Elasticitätsconstanten isotroper Körper. *Annalen der Physik*, vol. 274, n° 12, 1889, p. 573–587, WILEY-VCH Verlag.
- [WAN 06] WANG Z., MA H., ZHAO L., YANG G.
Studies on the dynamic compressive properties of open-cell aluminum alloy foams. *Scripta Materialia*, vol. 54, n° 1, 2006, p. 83 - 87.
- [WAN 10] WANG J., WANG H., CHEN X., YU Y.
Experimental and numerical study of the elastic properties of PMI foams. *Journal of Materials Science*, vol. 45, n° 10, 2010, p. 2688–2695.
- [WAR 87] WARREN W., KRAYNIK A.
Foam mechanics : the linear elastic response of two-dimensional spatially periodic cellular materials. *Mechanics of Materials*, vol. 6, n° 1, 1987, p. 27 - 37.
- [WAR 88] WARREN W., KRAYNIK A.
The linear elastic properties of open-cell foams. *Journal of Applied Mechanics*, vol. 55, n° 2, 1988, p. 341–346, American Society of Mechanical Engineers.
- [WAR 97] WARREN W., KRAYNIK A.
Linear elastic behavior of a low-density Kelvin foam with open cells. *Journal of Applied Mechanics*, vol. 64, n° 4, 1997, p. 787–794, American Society of Mechanical Engineers.
- [WOJ 17] WOJTACKI K., DARIDON L., MONERIE Y.
Computing the elastic properties of sandstone submitted to progressive dissolution. *International Journal of Rock Mechanics and Mining Sciences*, vol. 95, n° Supplement C, 2017, p. 16 - 25.
- [YAN 99] YANG J.
Development about composite homogenization in static and in dynamic-application to UD composite materials. Thèse de doctorat, l'Institut de Recherche en Génie Civil et Mécanique-Ecole Centrale de Nantes, 1999.
- [YE 15] YE W., BARBIER C., ZHU W., COMBESURE A., BAILLIS D.
Macroscopic multiaxial yield and failure surfaces for light closed-cell foams. *International Journal of Solids and Structures*, vol. 69-70, 2015, p. 60 - 70.

- [YI 01] YI F., ZHU Z., ZU F., HU S., YI P.
Strain rate effects on the compressive property and the energy-absorbing capacity of aluminum alloy foams. *Materials Characterization*, vol. 47, n° 5, 2001, p. 417 - 422.
- [YIN 14] YIN S., RAYESS N.
Characterization of Polymer-metal Foam Hybrids for Use in Vibration Dampening and Isolation. *Procedia Materials Science*, vol. 4, n° Supplement C, 2014, p. 311 - 316.
- [YU 07a] YU W., TANG T.
Variational asymptotic method for unit cell homogenization of periodically heterogeneous materials. *International Journal of Solids and Structures*, vol. 44, n° 11, 2007, p. 3738 - 3755.
- [YU 07b] YU W., TANG T.
A variational asymptotic micromechanics model for predicting thermoelastic properties of heterogeneous materials. *International Journal of Solids and Structures*, vol. 44, n° 22, 2007, p. 7510 - 7525.
- [YUA 08] YUAN Z., FISH J.
Toward realization of computational homogenization in practice. *International Journal for Numerical Methods in Engineering*, vol. 73, 2008, p. 361-380.
- [ZHA 14] ZHANG L., YU W.
A micromechanics approach to homogenizing elasto-viscoplastic heterogeneous materials. *International Journal of Solids and Structures*, vol. 51, n° 23, 2014, p. 3878 - 3888.
- [ZHU 97a] ZHU H., KNOTT J., MILLS N.
Analysis of the elastic properties of open-cell foams with tetrakaidecahedral cells. *Journal of the Mechanics and Physics of Solids*, vol. 45, n° 3, 1997, p. 319 - 343.
- [ZHU 97b] ZHU H., MILLS N., KNOTT J.
Analysis of the high strain compression of open-cell foams. *Journal of the Mechanics and Physics of Solids*, vol. 45, n° 11, 1997, p. 1875 - 1904.
- [ZHU 00] ZHU H., HOBDELL J., WINDLE A.
Effects of cell irregularity on the elastic properties of open-cell foams. *Acta Materialia*, vol. 48, n° 20, 2000, p. 4893 - 4900.
- [ZOH 04] ZOHDI T., WRIGGERS P.
Introduction to Computational Micromechanics (Lecture Notes in Applied and Computational Mechanics). Springer-Verlag New York, Inc., Secaucus, NJ, USA, 2004.

Scientific communications

- Articles
- W. Zhu, N. Blal, S. Cunsolo, D. Baillis. *Effective elastic properties of periodic irregular open-cell foams*. **Accept by International Journal of Solids and Structures**.
 - W. Zhu, N. Blal, S. Cunsolo, D. Baillis. *Micromechanical modeling of effective elastic properties of open-cell foam*. **International Journal of Solids and Structures**, 115, 61-72, 2017.
 - W. Zhu, N. Blal, S. Cunsolo, D. Baillis, P.M. Michaud. *Evaluation of effective elastic properties of irregular closed-cell foams*. **Article prepared for submission in Materials & Design**.
- Conference and seminars
- W. Zhu, N. Blal, D. Baillis. *A computational homogenization approach for effective elastic properties of open-cell foams*. **Société Française de Métallurgie et de Matériaux**. 23-25 octobre 2017, Lyon (France).
 - W. Zhu, N. Blal, D. Baillis. *A Hill's lemma computational homogenization approach for effective elastic properties of open-cell foams*. **13th National Conference on Computational Structural Mechanics**. 15-19 mai 2017, Giens (France).
 - W. Zhu, N. Blal, S. Cunsolo, D. Baillis, P.M. Michaud. *New laws for the elastic effective properties of Voronoi Kelvin open-cell foams in relation to their microstructure*. **Journée thématique: Les mousses solides à cellules ouvertes**. 20 octobre 2016, Lyon (France).



FOLIO ADMINISTRATIF

THESE DE L'UNIVERSITE DE LYON OPEREE AU SEIN DE L'INSA LYON

NOM : ZHU

DATE de SOUTENANCE : 16/05/2018

Prénoms : Wenqi

TITRE : Effective elastic properties of foams: morphological study and micromechanical modeling

NATURE : Doctorat

Numéro d'ordre : 2018LYSEI043

Ecole doctorale : MECANIQUE, ENERGETIQUE, GENIE CIVIL, ACOUSTIQUE

Spécialité : Mécanique – Génie Mécanique – Génie Civil

RESUME: Thanks to the excellent combination of physical, mechanical and thermal properties, foam materials bring new possibilities to extend the range of the properties for engineering, which is limited by fully dense solids. In this study, a micromechanical modeling based on Hill's lemma (Hill's lemma periodic computational homogenization approach) is proposed for predicting the effective elastic properties of foam materials. An approach based on Voronoi diagram is used to generate realistic periodic foam structures, including regular and irregular open-cell structures, and irregular closed-cell structures. First, the influences of morphological parameters of open-cell foams on the effective elastic properties are studied. The generated structures allow representing the details of the microstructure and cover a large range of foam materials for engineering purposes. With the assessments, new generic analytical laws are proposed for Kelvin open-cell foams by considering their morphological parameters. Second, the tomography images are analysed to obtain the morphological description of the real irregular open-cell structure. With these morphological parameters, numerous numerical realistic structures are generated. Specific statistic methods are proposed to determine the Representative Volume Element (RVE) for foam models. Third, the anisotropic irregular closed-cell foam is studied. The numerical structures are generated with the morphological description of the reconstructed tomography structure and the effective elastic properties of the closed-cell foam models are estimated. The numerical results show the satisfying agreement with the experimental results.

MOTS-CLÉS: Foam, Morphology, Tomography, Periodic computational homogenization, Effective elastic properties, Representative volume element

Laboratoire (s) de recherche : Laboratoire de Mécanique des Contacts et des Structures
UMR CNRS 5259 - INSA de Lyon
20, avenue Albert Einstein
69621 Villeurbanne Cedex FRANCE

Directeur de thèse: Professeur Dominique BAILLIS

Président de jury :

Composition du jury : Yann MONERIE; Hélène DUMONTET; Thouraya BARANGER; Guilherme MACHADO;
Dominique BAILLIS; Nawfal BLAL